Elastic Transmission of Identical Particles Through a Strongly Correlated Bose-Einstein Condensate

A Dissertation

submitted to the Faculty of the Graduate School

of the University of Minnesota

by

Yaroslav Lutsyshyn

in partial fulfillment of the requirements

for the degree of

Doctor of Philosophy

J. Woods Halley, adviser

December 2008

Acknowledgments

This work, along with a number of other projects, was done under the supervision of my thesis adviser J. Woods Halley. His projects were always interesting and challenging, making the whole experience so much better. I am grateful to him for his help and advice during all these years.

A number of faculty in Minnesota turned out not only to teach me things but also to offer guidance and encouragement. I would like to extend my gratitude to professors Charles Campbell, Paul Crowell and Keith Ruddick.

I acknowledge the financial support from the Physics department and professor Yuichi Kubota in his role as DGS for making it possible.

Graduate school turned out to be not just professional but also a personal experience. People that I met during this time have helped and influenced me. For this I owe thanks to many. Unfortunately I cannot mention all but a few.

Kindness and support of my girlfriend Mariya made finishing this work possible and even turned it into somewhat of a pleasant experience. It is hard to express how much this meant to me and how grateful I am to her.

I would like to thank my friends and colleagues. Some showed me the

way through the grad school, some offered help and tips, and yet others made it possible to have a good time in Minnesota. I would like to say thanks here to Jooho Park, Shramik Sengupta, Jorge Estevez, Lyuba Megits and Joseph Sabir, Erkan Tuzel, Roman Lutchyn, Alexander Chernatinsky and Jun Kyung Chung. Kudos to Alexei Kobrinskii for his LaTex tips.

I was introduced to math by my grandfather and I am lucky to have his unfaltering support and encouragement in my pursuits. I dedicate this work to him.

Abstract

Atomic transmission experiments on superfluid helium-four may provide information about its structure. It was proposed in the past that a transmission channel is possible in which the impinging atoms couple directly to the condensate fraction in helium-II. Such a mechanism would provide an important direct probe of the off-diagonal long-range order in helium-II.

We have successfully developed a method based on the diffusion Monte Carlo technique to simulate elastic transmission of atoms through a slab of helium-four at zero temperature. The scattering process is presented as a sum of appropriate standing wave scattering states. The phase factors for each scattering state are determined by matching the diffusion Monte Carlo results with correct energy of the scattering state. The scattering states effectively set the boundary conditions for the problem and in this way determine a phase factor and momentum of the incoming particle. Diffusion Monte Carlo is then performed in its fixed-node flavor.

Our results suggest a possibility of complete transparency of small unbound helium films for a broad range of incoming particle's energy. Wavepacket analysis of the computed transmission coefficient's phase dependence on

the incoming particle's wavevector was used to obtain times of the transmission process. Time delay analysis suggests the presence of anomalously fast transmission. Such results are strongly supportive of the original condensate mediated transmission hypothesis.

Contents

List of Tables

List of Figures

List of Abbreviations

$\boldsymbol{X}$	$\{\boldsymbol{r}_1 \cdots \boldsymbol{r}_N\}$, coordinate in the configuration space
ϕ_0	Ground state wave function of the considered system
ϕ_i	Hamiltonian eigenfunctions of the considered system
Ψ_{T}	Trial function
τ	Imaginary time in DMC evolution
K_0	$\frac{\hbar^2}{2m}$
BEC	Bose-Einstein Condensate / Condensation
DMC	Diffusion Monte Carlo
DMC 2a	Second order DMC algorithm from Ref. [86]
FN DMC	Fixed Node DMC
GFMC	Green's function Monte Carlo
RN DMC	Released Node DMC

s.p.	System point
VMC	Variational Monte Carlo

Chapter 1

Introduction

When cooled to low temperatures, helium-four liquefies at about 4.2 K but never freezes unless pressurized above 26 atm. This is due to a combination of low mass of helium atom with the resulting large zero-point confinement energy on one hand, and low attraction between helium atoms due to their closed electronic shell on the other. At about 2.17 K and saturated vapor pressure, liquid ^{4}He undergoes a phase transition with characteristic λ-peak in heat capacity. Below this temperature it experiences a number of peculiar properties [1], including ability to flow without resistance. This property being so remarkable, helium at this phase is referred to as superfluid.

Soon after its discovery in 1938, the lambda transition in helium was explained by London [2, 3] as occurring due to an onset of Bose-Einstein condensation (BEC) of helium atoms. Unambiguous evidence of the condensation as a presence of macroscopic number of atoms occupying the same

single-particle state turned out to be a challenging task. The condensation effect is significantly complicated by the interactions between atoms in the liquid, making superfluid ^{4}He (helium-II) a system with properties far from those of an ideal gas of bosons.

In an ideal gas of bosons, all particles will occupy the lowest single-particle state as temperature decreases to absolute zero. One measure of the presence of BEC in helium-II is the *condensate fraction*, a fraction of atoms in the lowest single-particle state at an instance. This measure is equivalent to the presence of the off-diagonal long-range order (ODLRO) in superfluid [4, 5]. Consider many-body wavefunction Φ describing the superfluid. The one-body density is given by the matrix element correspond to removing a particle from the system and then reintroducing it at a different location:

$$\rho_1(\boldsymbol{r}'', \boldsymbol{r}') = \left\langle \Phi \left| \psi^\dagger_{\boldsymbol{r}''} \psi_{\boldsymbol{r}'} \right| \Phi \right\rangle$$

where ψ and $\psi^\dagger$ are position representations of the annihilation and creation operators of one of the atoms. Because the bosonic wavefunction has to be symmetric over particle exchange, it does not matter which atoms we choose for this procedure. Lets introduce a summation over a complete set

in momentum representation:

$$\begin{aligned}
\rho_1(\boldsymbol{r}'', \boldsymbol{r}') &= \sum_{\boldsymbol{k}} \left\langle \Phi \left| \psi^\dagger_{\boldsymbol{r}''} \right| \boldsymbol{k} \right\rangle \left\langle \boldsymbol{k} \left| \psi_{\boldsymbol{r}'} \right| \Phi \right\rangle \\
&= \sum_{\boldsymbol{k}} \left\langle \Phi \left| a^\dagger_{\boldsymbol{k}} \, \mathrm{e}^{-\mathrm{i}\boldsymbol{k}\boldsymbol{r}''} \, a_{\boldsymbol{k}} \, \mathrm{e}^{\mathrm{i}\boldsymbol{k}\boldsymbol{r}'} \right| \Phi \right\rangle \\
&= \left\langle \Phi \left| a^\dagger_0 a_0 \right| \Phi \right\rangle + \sum_{\boldsymbol{k}\neq 0} \left\langle \Phi \left| a^\dagger_{\boldsymbol{k}} a_{\boldsymbol{k}} \, \mathrm{e}^{\mathrm{i}\boldsymbol{k}(\boldsymbol{r}'-\boldsymbol{r}'')} \right| \Phi \right\rangle
\end{aligned}$$

In the limit of increasing distance between $\boldsymbol{r}'$ and $\boldsymbol{r}''$, terms in the sum on the right hand side will vanish due to oscillatory phase. Therefore, in the limit of large separation the one body density matrix is a measure of the condensate fraction n_0:

$$\rho_1(\boldsymbol{r}'', \boldsymbol{r}') \xrightarrow{|\boldsymbol{r}''-\boldsymbol{r}'|\to\infty} \frac{N_0}{V} = \frac{n_0 N}{V}$$

Condensate fraction in helium-II can be found by neutron scattering as proposed by Hohenberg and Platzman [6]. The method consists of studying the distribution of momentum of helium atoms from momentum of scattered neutrons. However, the momentum of neutrons has to be not only large enough so that their wavelength is smaller than interatomic distances in helium-II, but also large enough so that during the time of the collision the neighboring atoms do not adjust their positions due to recoil. The necessary approximations and extrapolation (condensate fraction also varies strongly with temperature) led to a long series of experiments (see for in-

stance Refs. [7–9]) that did not easily converge to a single definite value for n_0. The currently agreed value for the condensate fraction is about 9%. Unfortunately, the final agreement relied heavily on theoretical predictions [4,10–14]. While there is little reason to doubt the current value for the condensate fraction, neutron scattering remains the only tool for probing condensation in helium-II. As such, it is a very energetic probe far separated from energies characteristic for such a delicate phenomenon as is superfluidity or the Bose-Einstein condensation. Neutrons used for these studies have momenta of at least an order [15] of magnitude larger than low lying features of helium-II excitation spectrum, and it was suggested [16] that at least two orders of magnitude are in fact necessary for a clean measurement of the condensate fraction.

Halley et al. proposed [17, 18] that condensation phenomenon may be probed directly by observing a transmission of atoms through a slab or a droplet of superfluid helium. Such an experiment would use a probing mechanism alternative to neutron scattering. The process would also be directly related to the OLDRO and the one-body density matrix as the experiment effectively introduces an atom in one location and removes an atom at another. Transmission of atoms has indeed been observed [19,20], however none of the performed experiments confirmed or ruled out the possibility of transmission via coupling to the condensate fraction of superfluid. The motivation of this project to continue and improve on our past efforts [21, 22] to characterize the transmission by numerical methods. We believe such calculations may

shed light on the details of the process and provide important guidance for future experimental studies. We modified quantum many-body computational methods to make them capable of characterizing the transmission and applied them to this problem. We find that our results indeed support the condensate-mediated transmission hypothesis.

Chapter 2

Condensate mediated transmission

2.1 Transmission experiment

The motivation of this work is to characterize a series of existing and possible experiments to which we will refer as the *transmission experiments*. These are experiments in which one observes a transmission of atomic beam of helium through a film or cluster of superfluid helium four. Physical process of interest here is coupling of the impinging atoms somewhere near surface to the bulk which should be dependent on the nature and properties of the superfluid, in particular its excitation spectrum. It can also perhaps depend on the existing condensate fraction in the film, roughly the number of bosons in one-particle ground state orbitals. We believe that investigating the latter

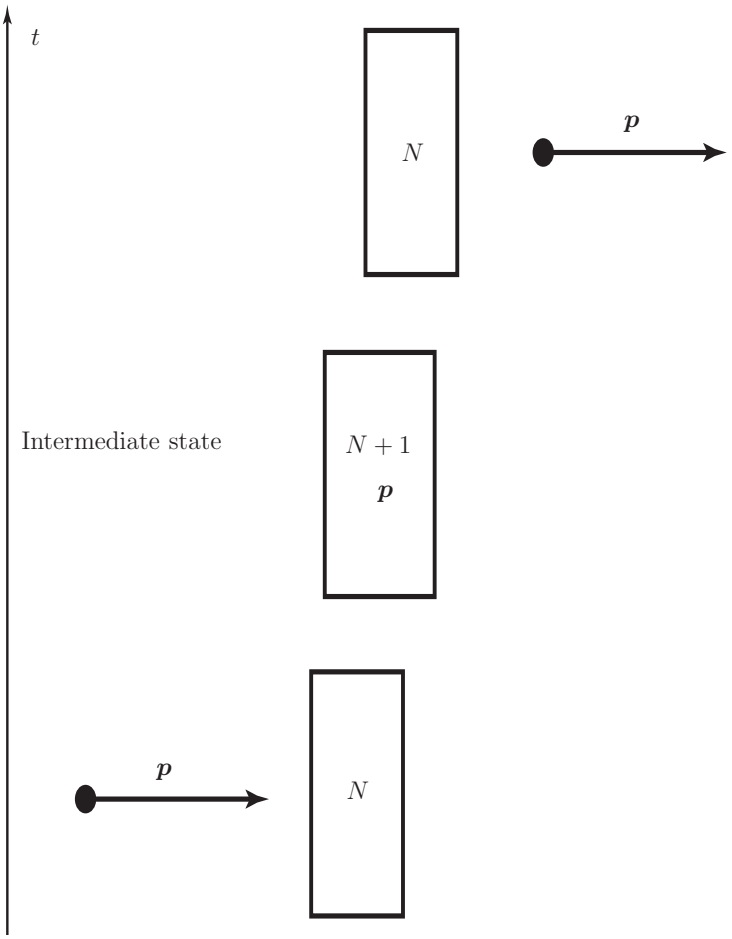

Figure 2.1: Diagram depicting stages of the transmission process with time increasing bottom to top. The intermediate state carries a film with one extra particle and corresponding conserved momentum. However if the intermediate process is short compared to Heisenberg's principle's limitation $\Delta t < \hbar/\Delta e$, the state may be virtual with corresponding violation of energy conservation.

possibility may provide better understanding of the nature and physics of Bose-Einstein condensation in strongly interacting systems of which liquid helium is a prime example.

The experimental arrangements for transmission experiments may differ though they normally consist of shooting a beam of atoms onto a macroscopically thick suspended film of superfluid helium. Some atoms are ejected on the other side of superfluid and their energy flux is detected and recorded as a function of time. Comparing the energy flux of atomic beams that traveled with and without the film in place, one tries to draw conclusions about the underlying physical processes. However, the integral nature of the signal requires interpretation, including extensive numerical modeling. Considering the transmission of a single atom, timeline of the process can be separated into three stages, as illustrated in Fig. 2.1:

- Impinging and coupling: When the impinging atom is far from the film, it can be distinguished and has a well defined momentum. The film is in its ground state determined by the geometry and the means by which it is suspended (or none if it is a free-falling droplet etc.). Once the particle approaches the surface, it has to somehow couple to the structure of the superfluid.

- Transmission stage: "Information" about the impact has to be transmitted through the film. The means by which this occurs is said to *mediate* the transmission. A possible mechanism is propagation of one

or more quasiparticles excited by the incoming atom. It can perhaps also be done thought the entire wavefunction of the condensate in the superfluid [18], a hypothesis which is the subject of this work.

- Ejection stage: To conserve the momentum, one or more atoms have to decouple and be ejected from the opposing surface of the film. Given carefully chosen parameters of the beam with respect to the chemical potential of superfluid helium-4, it can be arranged that only one atom can possibly decouple from the film.

The most peculiar result of the transmission experiments is of course that there are any transmitted particles at all. Simple and convincing analysis leads to the conclusion that atoms are transmitted *elastically*, i.e. any transmitted atom corresponds to some impinging atom which had the same momentum vector[a]. Because of this fact, the transmission is a significantly quantum effect and may be considered a manifestation of quantum mechanical nature of superfluidity.

[a]It is usually concluded that the atoms from the incoming beam do not interfere in a sense of exchange between impinging atoms or mixing of pathways for the transmission mechanism. Because the atoms are coming from the same vapor cloud, their properties are described by Maxwell statistics for a particular beam. Collisions within the beam may also determine the coherence of wavepackets which may be chosen to represent the atoms. (Collisions are measurements of position and therefore determine the uncertainty in momentum.)

2.2 Quasiparticle mediated transmission

When helium particles are shot onto helium-II, they may be absorbed by exciting a single quasiparticle inside the liquid, usually a phonon or a roton, in a process known as *quantum condensation* [23, 24]. As such quasiparticle travels and reaches another free surface, it may terminate by ejecting a single atom in process known as *quantum annihilation* [25–28]. Both processes have by now been well established experimentally[b]. One may imagine them combined to produce transmission given a volume of helium-II with two free surfaces. We refer to such processes as *quasiparticle mediated transmission*. Incoming atoms may excite a single quasiparticle which travels to the other free surface and emits an atom via quantum annihilation.

The energy of the excited quasiparticle (Fig. 2.2) comes from the kinetic energy of the incoming atom and that atom's chemical potential. Atoms at the lowest energies excite phonons. Atoms with kinetic energy above 1.5 K can also excite rotons [29] with momentum higher than that for roton minimum and which therefore have positive group velocity (R^- rotons with negative group velocity are much less likely to be created during condensation and their quantum annihilation is also suppressed [30, 31]). Atoms with even higher energy may in principle also excite single quasiparticles, but their energies are also sufficient to create multiple phonons and rotons from a sin-

[b]Confirming quantum condensation by itself was and remains a much harder task than confirming quantum annihilation because it is more difficult to detect and characterize quasiparticles than to do that for ejected atoms

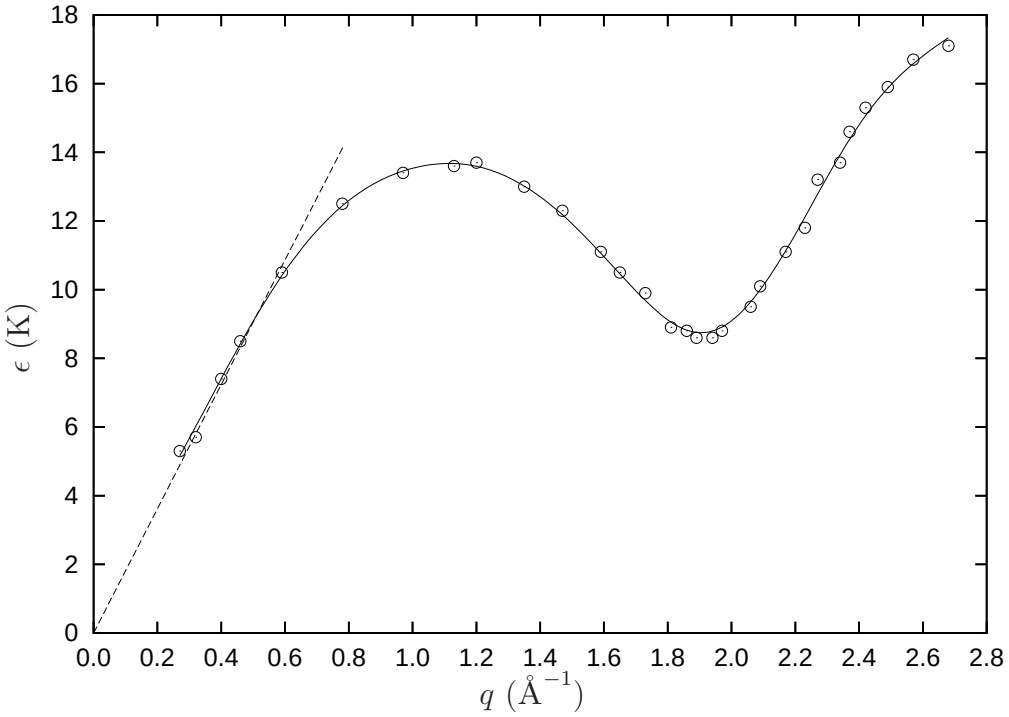

Figure 2.2: Helium-II excitation spectrum. Data from [33]. Solid line is a smooth fit to the data. Dashed line in the phonon region corresponds to $\epsilon = \hbar ck$ with the speed of sound $c = 237^{\mathrm{m}}/_{\mathrm{s}}$. See Donnelly and Barenghi [34] for a review of rather more detailed data for the excitation spectrum.

gle impact and therefore dissipate the energy. Such multi-particle processes will dwarf the elastic processes [32]. For this reason the phonon and roton-mediated transmission is associated with impact atoms of low enough energy low enough so as not to create multiple quasiparticles. Such elastic quasiparticle mediated transmission was indeed observed in experiments conducted by our group [19] and in experiments by Williams and Wyatt [20]. These experiments are described in greater detail in section 2.4.

2.3 Condensate mediated transmission

This study is part of an ongoing effort to test the proposal [17, 18, 35, 36] that due to Bose-Einstein condensation in superfluid helium-four, part of the incident atoms may be subject to an anomalously fast reemission in the transmission experiments. One of the possible scattering processes in the transmission experiment is what we refer to as condensate mediated transmission. In this virtual process, an incoming particle becomes part of the condensate system, still in its ground state but now with one extra particle, which leads to elastic reemission from the other surface of the film. The transmission is not mediated by a density wave, but rather by exchange of the incoming particle with the condensate as a whole.

Energy cannot be conserved in the intermediate state of such an event, and is violated by

$$\Delta E = -\mu + K \tag{2.1}$$

where μ =-7.17 K is chemical potential and K is kinetic energy of the incoming particle. According to the uncertainty relation, such a state may only exist for such times Δt that

$$\Delta t < \hbar/\Delta E < \hbar/|\mu| \approx 10^{-12} \text{ s}$$

which evaluates to less than the light time-of-flight through the condensate if the slab is thicker than a few hundred micrometers. While a relativistic

calculation taking account of potential retardation would be required to estimate this time correctly for thicker slabs, it seems safe to assume that *the condensate mediated transmission times are vanishingly small compared to times associated with any other process involved.* In this sense, we will refer to condensate mediated transmission as an "immediate" process. To summarize, transmission times for condensate mediated transmission are vanishingly small compared to other processes, and will appear independent of the slab thickness. Transmission times for the quasiparticle mediated transmission on the contrary scale proportionately to the slab thickness and must be consistent with group velocity of the corresponding quasiparticles which are known from the excitation spectrum of helium. The amplitude for both processes is likely to vary with the slab thickness. While little can be deduced beforehand for such dependence in the condensate-mediated transmission, the amplitude for quasiparticle mediated transmission has to be consistent with existing (but unfortunately incomplete) knowledge about the mean free path of the corresponding quasiparticles.

Due to its short time of flight, condensate mediated transmission would produce distinct features in the transmission experiment data. If observed, the presence of such features would be a signature of Bose-Einstein condensation in the system. Results could possibly be used to extract information about the superfluid, such as the condensate fraction.

Role of coupling to the substrate and restricting the center of mass motion

During the intermediate stage of the condensate mediated transmission, the entire slab carries the momentum. While this stage is very short and resulting speed and the involved displacements will be small, this intermediate stage still needs to be allowed in order for the process to occur. The implication is that in any experiment aimed at observing condensate mediated transmission, the slab or film of helium may not be strongly bound. The binding has to be sufficiently weak so that the momentum transfer to the film during this intermediate stage be much less than momentum of the incoming particle. A proper simulation of the condensate mediated transmission has to be able to describe this intermediate motion of the center of mass. Center of mass should also be allowed to move freely, or be bound only weakly as in VMC calculations that we refer to on p. 26.

Uncertainty principle considerations

Assuming that the information about the incoming particle cannot propagate faster than light and combining this with Heisenberg principle's limitation on the time of a virtual process, we obtain

$$\frac{L}{c} = \frac{\hbar}{\epsilon - \mu}$$
$$L = \frac{c\hbar}{\epsilon - \mu} \leq \frac{c\hbar}{|\mu|} = 320\ \mu\text{m}$$

For slabs thicker than a critical value (which has to be lower than the above estimate), the amplitude for the condensate mediated transmission will be decreasing. It is however impossible to make a good estimate of this effect without a calculation taking account of potential retardation during exchange of helium atoms in the condensate mediated transmission.

All experiments to date used helium slabs smaller than this size. In order to distinguish transmission times between condensate mediated transmission and transmission mediated with low or high energy rotons through a 320 μm slab, one would need experimental resolution varying from about 100 μs to as low as 1 μs. Existing calculations calculations use much smaller systems (under 100 Å).

2.4 Previous experimental results

Creating a helium slab with open opposite surfaces to allow for both incoming beam to enter the surface and the transmitted beam to exit on the other end is a necessary and challenging part for transmission experiments of the kind described above. Making free standing films with helium is particularly difficult because helium wets almost all known materials. In fact, for a long time it was thought that liquid helium wets all surfaces without exception.

Consider that the attractive force between helium atoms is exclusively of van der Waals origin. Because of the closed shell of the helium atom, this force also has a small amplitude, and the van der Waals force between a

helium atom and any other atom is expected to be larger than such a force between helium atoms per se. In other words, helium is attracted more to almost any other material than to itself. Such "superwetting" behavior for a long time made it impossible to suspend free films as is commonly done with other materials — the film simply flows away from any hole toward the bulk of the surface.

Phonon mediated transmission

An exception to wetting behavior of helium is its interaction with cesium [37]. It was discovered in the early 1990s that helium in fact does not wet cesium surfaces under certain conditions. While cesium is understood to still have larger van der Waals attraction for helium atoms than the helium atoms themselves, the large diameter of the repulsive core of the Cs-He interaction prohibits atoms from coming close enough to realize the energetic gain from the van der Waals force and raises the minimum of the interaction potential. This exception was taken advantage of by our group to perform a version of the transmission experiment. Williams et al. [38] suspended free standing helium films on a Cs-coated orifice, in a setup which was later used by Lidke and coworkers to observe transmission of atoms through such films [19].

The "probe" atomic beam was created by evaporating helium from a film coating a heating element in contact with bulk helium liquid. The transmitted beam was recorded as time-of-flight graph of kinetic energy of matter arriving at annealed titanium-film superconducting bolometers. The size of

the orifice was 50 μm, and transmission was observed when films were thinner than 0.1 mm. Meniscus or shape of the surface could not be measured or controlled. The observed transmission was attributed to phonon mediated quasiparticle processes.

Signals from freely propagating beams (open orifice) matched remarkably well a gas dynamics simulation of beam creation and propagation [39]. This allowed extraction of properties of the beam, in particular kinetic energies of the atoms. Using this data in conjuncture with calculations of Sobnack, Inkson and Fung [40], the authors concluded that the majority of quasiparticles created during the impact of the atomic beam onto the helium film were phonons. This is mostly a result of low kinetic energy of the incoming particles. The slab surface was presumed flat in all the modeling. This interpretation was also consistent with the strong attenuation of the transmitted beam with thickness of the film, as the photon mean free path [41–43] tends to be much shorter than m.f.p. for the rotons.

Overall, modeling of pulse propagation and elastic transmission through helium slab supports the phonon mediated transmission as dominant mechanism explaining atom transmission through the superfluid.

No signature of condensate mediated transmission was observed in these experiments. However, such a transmission would be masked by the phonon signal, and the time of flight resolution was insufficient to resolve the corresponding difference in the propagation times. Additionally, strong coupling of helium slab to the orifice may suppress the condensate mediated transmis-

sion as it requires a freely moving slab in the intermediate process.

Roton mediated transmission

Another version of the transmission experiment was performed by Williams[c] and Wyatt at the University of Exeter, UK. In their experiment [20], helium was suspended in an array of cylindrical capillary channels passing perpendicular to the surface through a thin plate of glass.

The level of liquid helium below the glass plate set the chemical potential which controlled the meniscus of liquid in the channel, which in turn affected the least thickness of helium in the channel. Under the experiment's conditions, open surfaces could be rather close to being normal to the incoming atomic beam. The thickness of the slabs was fixed under these conditions and essentially matched that of the glass plate.

The atomic beam was created by a pulse of current through a heating element embedded in saturated vapor. Energy flux from the transmitted pulses was detected with zinc-based superconducting bolometers, with magnetic field-controlled transition temperature. This allowed tuning of the bolometers to the temperature of the surrounding cell. Helium slabs were just under 0.2 mm thick and 50 μm in diameter.

Williams and Wyatt observed arriving transmitted beams and interpreted these as atoms transmitted via quasiparticle-mediated transmission mediated by R^+ rotons[d]. The authors employed a model which included elastic creation

[c] C.D.H. Williams is not related to M. Williams from the Minnesota group.

[d] R^+ rotons are rotons with wavevectors above roton minimum. These have positive

of R^+ rotons, their ballistic propagation through the slab of superfluid and refraction on the helium-vacuum boundaries consistent with conservation of the transverse component of momentum. Quasiparticles reaching helium-glass walls were assumed to vanish, either due to diffusive scattering or mode shift to R^- rotons. This model was remarkably successful in describing the net fraction of transmitted atoms, and yielded a transmission amplitude of 12 to 15%. Dalfovo, Pitaevskii and Stringari predicted (reference 26 in [20]) that the probability of quantum evaporation should be the same for quantum condensation as for quantum evaporation. With this assumption, Williams and Wyatt's results predict these *probabilities* to be close to 35%, rather close to the value predicted by Campbell et al. [32] for a broad range of momenta of the incoming atoms.

It is worth pointing out that the transmission was strongly (by over an order of magnitude) suppressed by increasing surface curvature of the slab meniscus. In other words, near-normal incidence was demonstrated to have considerably larger transmission amplitude. This was however at least in part due to the large aspect ratio of the slab and the refraction at the surface with consequent dissipation of quasiparticles on the walls.

This experiment was a convincing demonstration of roton-mediated transmission. Authors did not consider and made no conclusion regarding possibility of condensate-mediated transmission in these measurements. The

group velocity and are much more likely to be created and to consequently quantum-evaporate than R^- rotons with the wavevector below roton minimum. See Refs. [30, 31]

large time delay due to the heating time constant of the detector bolometers made it impossible to clearly separate phonon-mediated transmission from the roton-mediated effects. This same effect would make it impossible to distinguish signals characteristic of the condensate mediated transmission, which one may speculate is more likely to occur for slower-moving atoms.

As in the Cs-surface experiment, helium slabs in this experiment were strongly bonded, in this case to the glass surface. Constraining the center of mass motion of the condensate is likely to suppress the condensate mediated transmission, which requires a virtual state with a freely moving center of mass.

Transmission through ballistic droplets

Instead of suspending helium films, one may attempt experiments on helium droplets that are not in a contact with any surface. This was the path chosen in an earlier transmission experiment by Harms and Toennies [44]. In their experiment, a jet of helium-4 gas expanded rapidly through an orifice to produce moving helium droplets or clusters. These droplets entered a chamber with uniform gas of another or the same atomic species, where most of the scattering took place. The flux of droplets was recorded as they arrived at the other end of this chamber. The scattering of atoms on the incoming droplets causes the droplets to slow down and the distribution of their velocities to disperse. Analyzing time of flight graphs of flux along with known temperature and density of the background gas allowed the authors to

compute the momentum transferred on average from colliding gas atoms to the droplets. Looking at the mass loss due to rapid evaporation [45] allowed them to deduce the amount of transferred energy, in an independent but somewhat less precise manner. The droplets had a macroscopically large number of atoms $N \sim 10^9$, and had velocities about 75 $^{\mathrm{m}}/_{\mathrm{s}}$.

Harns and Toennies studied transmission of droplets through argon and both ^{4}He and ^{3}He gas. They observed that Ar atoms tend to deposit their entire momentum and energy upon incident with helium droplets. (This was also observed in earlier work by Toennies group [46,47].) ^{4}He and ^{3}He atoms however, had a considerable fraction of their momentum and energy that was not transferred to the droplet. Transmission, as deduced from the lack of momentum transfer, was in fact enhanced for ^{3}He compared to ^{4}He. Most likely cause for this was the fact that a single ^{3}He atom has a much smaller binding energy (chemical potential) in bulk ^{4}He than the chemical potential of ^{4}He by itself. This is a consequence of ^{3}He having smaller mass. Small binding energy of 2.7 K gained by ^{3}He atoms upon an impact with a droplet resulted in smaller total kinetic energy compared with that for impinging ^{4}He atoms. The spectrum of a single ^{3}He atom in bulk ^{4}He is effectively that of a single particle [48–50] (albeit with a large effective mass) up to quite large velocities where it first intercepts the ^{4}He excitation spectrum near the roton minimum. It is therefore possible that ^{3}He moving at velocities below the Landau velocity [1] could enter the droplet, transit through it without loss and exit on the other side. It is thus believed that transmission of such slow

^{3}He atoms was indeed a demonstration of superfluidity. Because the kinetic energy of ^{3}He atoms was just below the threshold of quantum evaporation for phonons, such frictionless transition of ^{3}He was interpreted as the most likely explanation for the lack of momentum transfer in the case of ^{3}He scattering.

Larger loss of ^{4}He atoms compared with ^{3}He may be attributed to larger energy of ^{4}He atoms due to their larger chemical potential in bulk ^{4}He. This allowed ^{4}He atoms to lose their energy and momentum by exciting quasiparticles in the droplet. It was also suggested that observed transmission may be in part via phonon mediated transmission or by a process in which a few ripplons are excited at the impact point, which then traveled around the droplet to eject an atoms in the form of multiple-quasiparticle quantum evaporation event. However, the energy deposited into the droplets by incoming ^{4}He atoms was in excess of 13 K, sufficient to excite various combinations of multiple quasiparticles inside the droplet. Because of the involved energies being too high, this experiment did not allow one to distinguish between various possible transmission processes for impinging ^{4}He atoms.

Reflection experiments

There has been a number of atom reflection experiments [51–53], usually from adsorbed films. These experiments are simpler in the sense that no film suspension is necessary. It is observed that there's very little reflection if atoms are incident normally to the surface. Some experiments observed large reflection amplitudes for grazing angles. These results laid down the ground

for past and current theoretical investigation (see for example [54,55]). They are interpreted in terms of various quasiparticle process. However, these results cannot be directly interpreted in relation to this study.

Implications for this study

The above experiments demonstrated the possibility of elastic transmission of a current of low density single helium atoms through a macroscopically large volume of superfluid by means of various mechanisms. Understanding the data in these experiments would benefit greatly from additional theoretical work. They were accurate enough to test certain hypotheses that may be extracted from theoretical work, such as transmission probabilities or dominant channels for various quasiparticle processes. From this perspective, attempting to describe the transmission in a numerical simulation is a viable path toward better understanding of the structure of superfluid.

As for the possibility of condensate mediated transmission, none of these experiments provided a hint of its existence, but did not rule it out either. None of the experiments had sufficient resolution in the time-of-flight graphs to quantify the number of atoms transmitted via various channels. Factors such as curvature of the surface and the large speed of incoming atoms as in the droplet experiment also enable various other transmission channels, further complicating the picture. This lack of understanding provides motivation for this research.

2.5 Previous computational results

In this section we review past theoretical efforts important in the context of this work. Each used different methods; one should refer to particular publications for details.

Transmission through a weakly interacting gas

Transmission through a weakly interacting Bose-Einstein condensate may be calculated by means of Bogoliubov approximation and properly fixed boundary conditions for the excitations in the condensate. These conditions should describe the scattering and carry away the momentum of the impinging atom. This approach was used in our group by Wynveen et al [22, 56]. Wynveen considered scattering off a suspended spherical droplet. It was found that the transmission was much larger than provided by the Hartree-Fock approximation. At large momenta of the incoming particles, coupling to the condensate enhanced the transmission, and this effect was insensitive to the coupling strength.

Paulsen and Mølmer later performed a similar transmission calculation [57] for a one-dimensional bound slab of weakly interacting BEC. They observed a rich structure in the transmission amplitude, most likely due to the geometrical effects. A careful phase shift analysis allowed them to extract the transmission times. Their results indicated negative transmission times which the authors expected to actually occur in this system. While

we do not observe such effects in present calculations, the results of Paulsen and Mølmer support the hypothesis of condensate mediated transmission or similar exchange effects.

HNC-EL calculation

Campbell, Krotscheck and Saarela applied the Hypernetted Chain Euler-Lagrange theory to the problem of transmission of ^{4}He atoms through a slab of superfluid [32, 58]. Only normal incidence was considered. The slab was 80Å thick. Within approximations made, the method allows a complete treatment of a number of scattering and dissipation channels including excitation of multiple quasiparticles and quasiparticle mediated transmission. Authors observed large sticking and dissipative processes which were found to occur mostly near the surface. Nonetheless, a considerable amplitude for elastic transmission was found with dependence on the energy deposited by the incoming particle.

The absolute value of the transmission amplitude was found to be about $|T| = 0.5$ near $E = 8$ K (relative to the vacuum). There was a sharp drop in the value of $|T|$ near the energy where hybridization can first occur between different quasiparticles of the same energy near 10 K, and a broad plateau of $|T| \approx 0.3$ for deposited energies ranging between 11 and 14 K, likely due to roton mediated transmission events. We will not be able, however, to compare directly with these results as our calculation will be limited to elastic events.

These calculations, performed long before confirmed transmission experiments, predicted a likelihood of observing a macroscopically large fraction of incoming atoms causing an elastic transmission. The calculations however, did not allow the center of mass motion and therefore could not possibly account for condensate mediated transmission as described earlier. The method is also only accurate to the order of N^{-1}, N being the number of particles in the system [59]. This means that effects associated with the center of mass motion may not be readily described by such calculations. This result encourages us to continue with further investigation of the transmission processes.

Variational calculations

The work presented here is an improvement on past variational calculation of the transmission problem by Setty, Halley and Campbell [21, 36]. Setty used a model for the transmission wavefunction which included a mixture of two terms. The first term described N particles in the slab and a particle moving on the outside, conforming to the boundary condition $T\,\mathrm{e}^{\mathrm{i}kz}$ on one side of the slab and $\mathrm{e}^{\mathrm{i}kz} + R\,\mathrm{e}^{-\mathrm{i}kz}$ on the other — symmetrized over all particles. The moving particle term was constrained from penetrating deep into the slab and the particles in the slab were confined by an envelope. The other *boost* term described the motion of the entire $(N+1)$-particle system. The two terms were mixed with a variational parameter. The slab was held in place by a term of the form $\exp(-\alpha z_{\mathrm{c.m.}})$ where α was set sufficiently small so as

not to interfere with any involved energy scales. Correlations were described by pair products of Jastrow type. These terms will be described later when I give details of the trial function used in the present work.

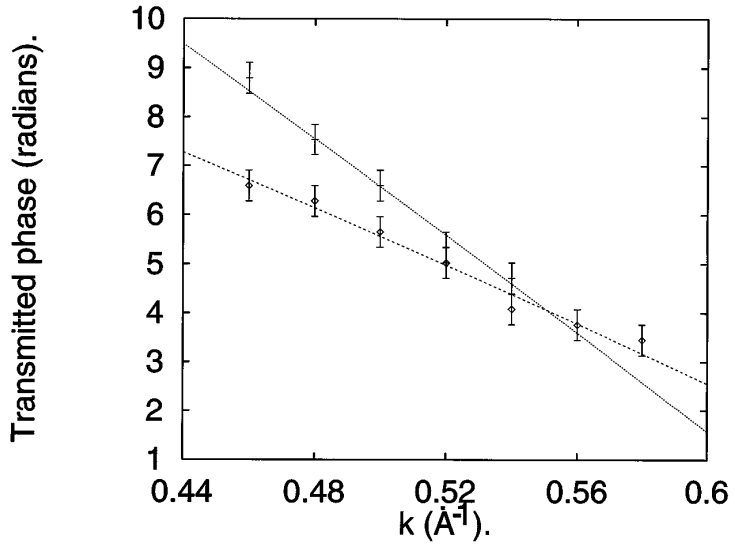

Figure 2.3: Variational results for the phase of the transmission coefficient for two different slab width as obtained by Setty and colleagues. See the original publication [36] for details.

Setty performed a search in a rather large space of variational parameters to optimize the wavefunction. The criteria consisted of a requirement that the state energy be as close as possible to the correct value of the sum of energies of free-moving particle and an N-particle slab, *and* that the current be constant throughout the volume. Reasonable optimization were achieved, and the amplitude and phase of the transmission coefficient along with its phase could be extracted. This information is reproduced in Fig. 2.3. Phase results can be used to extract the transmission times as described in Sec. 6.4.

The transmission time depends on the slope of $d\phi_{\mathrm{T}}(k)/dk$ and the straight lines in Fig. 2.3 correspond to times independent of the incoming particle's speed. The two lines correspond to calculation done for slabs of two different widths — 20Å and 40Å. The corresponding slopes of the phase of the transmission coefficient are such that the transmission times are the same for both calculations and are within their standard deviation from zero. These findings support the hypothesis of condensate mediated transmission: The transmission times turn out to be negligible compared to possible competing processes and are independent of slab thickness for the calculation (so long as it does not account for the relativistic retardation effects in the potentials).

Setty used systems with 66 and 132 helium atoms. Slab dimensions were correspondingly chosen to be 20Å $\times$ 12.21Å $\times$ 12.21Å and twice wider. Wavevectors between 0.45Å^{-1} and 0.60Å^{-1} were considered. The transmission amplitudes that were found varied between 0.55 and 0.65.

Quantum variational calculations, though, are inherently limited by the choice of the variational wave functions and the optimization criteria. The choice of functions used for the optimization carries inherent bias as it is necessarily hand-picked with certain properties in mind, and because the simulated wavefunctions can never be improved beyond the selected model for the wavefunction — no matter how extensively the optimization is performed. Our current research is an attempt to expand on this approach and to simulate the transmission with a method that is less constrained by the choice of the model wavefunction.

DMC scattering calculations

In this project we will study the transmission problem with the diffusion Monte Carlo method. It is well suited to compute ground state properties of bosonic systems such as helium, but in its basic form cannot be used to simulate an excited state problem such as the transmission process. As far as we are aware, the only previous attempt to address scattering with DMC methods in condensed matter physics was undertaken by Shumway and Ceperley [60]. They successfully calculated cross-sections for elastic exciton-exciton scattering on a neutral background. The approach relied on a method previously developed by Carlson, Pandharipande and Wirinda [61] and by Alhassid and Koonin [62]. Both works considered scattering on small nuclei. These methods rely on fixing phase shift by nodes in the wave function far from the interaction region, and on finding the energy spectrum of the system constrained in such a way. The scattering matrix elements are extracted from this energy spectrum.

In the DMC case, the energy spectrum is extracted using the excited-states method of Ceperley and Bernu [63]. It relies on sampling with the usual ground-state approach and recording matrix elements for a trial set of excited state wavefunctions. There is little control over precision and reliability in this method. Finding a suitable set of the excited states is also challenging for a many-body problem like ours and this method has not yet been applied successfully to bulk helium. In conclusion, these previous works demonstrated the possibility of using DMC to successfully compute

scattering amplitudes in few-body quantum problems. However this method is not directly applicable to our problem and the existing approach had to be further modified to tackle the scattering on a many-body slab of superfluid.

Chapter 3

Quantum many-body calculations

3.1 Many-body Schrödinger equation

Solving an N-body quantum problem means solving the many-body Schrödinger equation:

$$\left(-\sum_{i}^{N}\frac{\hbar^2}{2m_i}\nabla_i^2 + V(\boldsymbol{r}_1,\ldots,\boldsymbol{r}_N) - E\right)\Psi\left(\boldsymbol{r}_1,\ldots,\boldsymbol{r}_N\right) = 0$$

where $\boldsymbol{r}_i$ is coordinate of i-th particle and in case of three dimensional space $\boldsymbol{r}_i = (x_i, y_i, z_i)$ and

$$\nabla_i^2 \equiv \frac{\partial^2}{\partial x_i^2} + \frac{\partial^2}{\partial y_i^2} + \frac{\partial^2}{\partial z_i^2}$$

Throughout this thesis, I will use lowercase bold symbols like $\boldsymbol{r}$ to denote individual particle's coordinate, and the set of coordinates of all particles in the system (coordinate in the configuration space) will be denoted by capital bold symbols like $\boldsymbol{X} \equiv \{\boldsymbol{r}_1, \cdots, \boldsymbol{r}_N\}$.

The large dimensionality of a typical system makes it impossible to solve the Schrödinger equation in any straight forward way as one would approach partial differential equation. To appreciate this, consider that it is not even possible to store the resulting wave function. If one wanted to tabulate the wave function by m points in each direction in the configuration space, it would require to store m^{3N} values, which is a prohibitively large number already for systems with only several particles. This multidimensionality problem and practical need to solve many-body problems led to development of a number of distinct methods. Among these those of purely numerical kind are mostly of Monte Carlo flavor due to their suitability for integration in the multidimensional space (for this the Schrödinger equation may be reformulated in an integral form). In the following sections I will describe several approaches relevant to this project.

3.2 Metropolis sampling and Variational Monte Carlo

Variational Monte Carlo (VMC) is by far a starting point for most many-body simulations. It samples a *trial wavefunction* that is one's best guess to the

correct solution of the problem, and is usually dependent on a set of numerical parameters. This sample is used to calculate expectation values of desired operators. One then varies parameters that the wavefunction depends on, to approach desired value of some optimization criteria. For example, if one is seeking to find ground state properties, the criteria is simply the expectation value of Hamiltonian that one attempts to minimize. In this form, VMC benefits from *variational principle* in that it provides an upper bound on the ground state energy [64].

To sample the trial wavefunction, VMC uses a chain of configurations in the configuration space. In a simplistic approach, these are generated with the original Metropolis [65] Monte Carlo approach. Calculation [66,67] begins with a reasonable guess for a coordinate of the system in configuration space (representing positions of all atoms and all relevant quantum numbers; we will only consider the positions). The algorithm then proceeds as follows:

1. Randomly select one or more of the components from the set of coordinates $\boldsymbol{X}$.

2. Randomly displace these coordinates to anywhere in the simulation volume, resulting in new configuration $\boldsymbol{X}'$.

3. Evaluate new value of the trial wavefunction $\Psi(\boldsymbol{X}')$, and compare it to the previous value $\Psi(\boldsymbol{X})$ by computing

$$æ \equiv \left| \frac{\Psi(\boldsymbol{X}')}{\Psi(\boldsymbol{X})} \right|^2 \tag{3.1}$$

4. If æ > 1, accept the new configuration, i.e. set $\boldsymbol{X}' \rightarrow \boldsymbol{X}$. Otherwise, accept the new configuration with probability equal to æ. (Typically one generates a random variable η distributed uniformly on $[0, 1]$ and accepts the new configuration if $\eta >$ æ.). Repeat at the first step.

Sequence of configurations generated with such acceptance criterion will be distributed with probability equal to the square of the trial wavefunction:

$$dP\left(\forall i : X_i \in [Y_i, Y_i + dY_i]\right) = \frac{\left|\Psi(\boldsymbol{Y})\right|^2}{\int \left|\Psi(\boldsymbol{Y})\right|^2 d\boldsymbol{Y}} \prod dY_i$$

This constitutes the Metropolis sampling of $\left|\Psi_{\mathrm{T}}\right|^2$.

It is easy to see that expectation value of some observable $\mathcal{A}$ can be estimated by averaging value of $\Psi^{-1}(\boldsymbol{X})\,\mathcal{A}\Psi(\boldsymbol{X})$ over the configurations $\{\boldsymbol{X}\}$ produced by VMC:

$$\left\langle \frac{\mathcal{A}\Psi}{\Psi} \right\rangle_{\mathrm{run}} = \frac{\int \left(\Psi^{-1}\mathcal{A}\Psi\right) \left|\Psi\right|^2 \, d\boldsymbol{X}}{\int \left|\Psi\right|^2 \, d\boldsymbol{X}} = \frac{\int \Psi^* \mathcal{A}\Psi \, d\boldsymbol{X}}{\int \left|\Psi\right|^2 \, d\boldsymbol{X}} \approx \left\langle \Psi \left| \mathcal{A} \right| \Psi \right\rangle \qquad (3.2)$$

Of course subsequent configurations produced by VMC are correlated and should not be used together with each other. Usually a certain number of sampling steps is performed in between performing calculations for operator expectations.

VMC is a robust method but it is limited in that the result is constrained by a particular functional choice of the trial wavefunction. Regarding our

calculations, it is used in two ways. Firstly, VMC-optimized wavefunction is used as a guiding function for the DMC calculations. Secondly, Metropolis-generated configurations (distributed as $|\Psi|^2$) are a good choice of initial condition for DMC ensemble.

3.3 Fokker-Planck sampling

Fokker-Planck sampling of the trial wavefunction is another sampling approach that can be used for VMC and is also closely related to DMC. One may refer to Hammond, Lester and Reynolds [67, Section 2.2.2] for a good introduction to the topic.

Consider a drift-diffusion equation or a time-dependent density function $f(\boldsymbol{X}, t)$. Given isotropic diffusion, time dependence of f follows the following Fokker-Planck equation:

$$\frac{\partial f}{\partial t} = \sum_i D \frac{\partial}{\partial X_i} \left(\frac{\partial}{\partial X_i} - F_i(\boldsymbol{X}) \right) f \tag{3.3}$$

where D is the diffusion constant and F_i is the i-th component of a drift velocity field. We are seeking a stationary distribution of f that is distributed as the square of the trial wave function. Demanding that each term in the Eq. (3.3) equals to zero independently, one arrives at the equation for the drift field:

$$\frac{\partial^2 f}{\partial^2 X_i} = f \frac{\partial}{\partial X_i} F_i + F_i \frac{\partial}{\partial X_i} f$$

Searching for the drift field in the form proportional to the gradient of f gives

$$\boldsymbol{F} = \frac{\boldsymbol{\nabla} f}{f} = 2\frac{1}{\Psi}\boldsymbol{\nabla}\Psi$$

One can now use the Langevin equation to simulate Fokker-Planck equation (3.3) with this velocity field. At a given step, a coordinate in the configuration space is replaced by a random shift according to the diffusion constant D and by a drift according to $\boldsymbol{F}$, giving $\boldsymbol{X}' \rightarrow \boldsymbol{X} + D\boldsymbol{F}(\boldsymbol{X})\Delta\tau + \boldsymbol{\xi}$, where $\Delta\tau$ is a small assumed timestep and $\boldsymbol{\xi}$ is a vector of random variables drawn from a (usually normal) distribution with variance $2D\Delta\tau$. Repeating this procedure for a some time with sufficiently small $\Delta\tau$, one arrives at a stationary distribution for f which samples $|\Psi|^2$.

3.4 Diffusion Monte Carlo

In 1970's, a series of new methods were developed for stochastic solution of quantum many-body problems. Among them was Kalos's Green's function Monte Carlo (GFMC) method [14, 66] which simulates the problem by iterating ${}^{(E-z)}/_{(\mathcal{H}-z)}$ to eventually find the correct ground state of the system (E and z are constants and $\mathcal{H}$ is the Hamiltonian). Given sufficient (but realistic) computing power, GFMC is capable of providing exact answer to a class of many-body problems. Powerful as it is, the GFMC method is algorithmically complex and requires certain limitations on the system's potential energy. It inspired a family of other exact methods, of which *diffusion Monte*

Carlo (DMC) soon replaced GFMC as the method of choice for a large class of problems. It was proposed by Anderson [68, 69], and developed in the 70's and 80's with the addition of importance sampling, fixed node and node release methods [70–74].

DMC methods proved to be a reliable and precise way to find ground state properties of bosonic systems, and provided excellent results for bulk and clusters of helium-II [75–77]. It was also applied to a variety of problems including the electron gas [72], molecular simulations [73,74] and the electron gas in a magnetic field (in 2D) [78]. We applied the DMC method for simulating the transmission process. While the details of our approach will be discussed later, the remainder of this chapter is devoted to a review of details and methodology of the DMC as described in the literature or developed for our purpose. DMC applies the operator $\mathrm{e}^{-(\mathcal{H}-E)\tau}$ on some initial guess Ψ_{I} for the ground state until at $\tau \to \infty$ contributions from all the excited states vanish leaving only a term $\mathrm{e}^{-(E_0-E)\tau}\,\phi_0$, where the ground state wavefunction ϕ_0 has energy E_0. E is chosen as close as possible to the ground state energy. The projection is done by stochastically sampling the configuration space. In order to achieve useful convergence, an importance sampling of the configuration space is necessary. This is done by introducing an importance sampling function Ψ_{T} which is usually called the trial function.

To describe the method in more detail, consider some function $\Psi_{\mathrm{I}}(\boldsymbol{X})$, which is an initial estimate for the system's ground state wave function. Let

$\phi_n(\boldsymbol{X})$ be the (unknown) energy eigenstates of the system's Hamiltonian:

$$\mathcal{H}\phi_n(\boldsymbol{X}) = E_n\phi_n(\boldsymbol{X}).$$

Then in principle it is possible to expand

$$\Psi_{\rm I} = \sum_n \langle\Psi_{\rm T}|\phi_n\rangle\phi_n(\boldsymbol{X}) = \sum_n A_n\phi_n(\boldsymbol{X})$$

defining A_n. Let function $f(\boldsymbol{X},\tau)$ be constructed by definition as

$$\begin{aligned} f(\boldsymbol{X},\tau) &= \Psi_{\rm T}(\boldsymbol{X})\,{\rm e}^{-(\mathcal{H}-E_{\rm ref})\tau}\,\Psi_{\rm I}(\boldsymbol{X}) \\ &= \Psi_{\rm T}(\boldsymbol{X})\sum_n \exp\big[-(E_n-E_{\rm ref})\tau\big]A_n\phi_n(\boldsymbol{X}). \end{aligned} \tag{3.4}$$

($\Psi_{\rm T}$ is assumed to be real, for reasons discussed below.)

If the *reference energy* $E_{\rm ref}$ is equal to ground state energy then

$$\lim_{\tau\longrightarrow\infty} f(\boldsymbol{X},\tau) = \Psi_{\rm T}(\boldsymbol{X})A_0\phi_0(\boldsymbol{X})$$

so that

$$\frac{1}{\Psi_{\rm T}(\boldsymbol{X})}\lim_{\tau\longrightarrow\infty} f(\boldsymbol{X},\tau) \propto \phi_0(\boldsymbol{X}) \tag{3.5}$$

because the exponential factors in the sum will cause all terms in the equation (3.4) for which $E_n > E_0$ to vanish in the limit of large imaginary time τ. It is said that excited states are projected out of the initial $\Psi_{\rm I}$.

If $E_{\rm ref} \neq E_0$, then f either vanishes or diverges at large τ. Therefore, if

a value is found for $E_{\rm ref}$ such that f neither vanishes nor diverges, then the ground state energy $E_{_0} = E_{\rm ref}$ and the ground state wave function is given by (3.5). (It is assumed that $\Psi_{_{\rm T}}$ has non-zero overlap with the ground state: $A_{_0} \neq 0$.) In order to compute f, let us look at its evolution with parameter τ. Using (3.4),

$$\begin{aligned}
\frac{\partial}{\partial\tau} f(\boldsymbol{X},\tau) &= \frac{\partial}{\partial\tau}\Psi_{_{\rm T}}(\boldsymbol{X}) e^{-(\mathcal{H}-E_{\rm ref})\tau}\Psi_{_{\rm I}}(\boldsymbol{X}) \\
&= -\Psi_{_{\rm T}}(\boldsymbol{X})\left(\mathcal{H}-E_{\rm ref}\right) e^{-(\mathcal{H}-E_{\rm ref})\tau}\Psi_{_{\rm I}}(\boldsymbol{X}) \\
&= -\Psi_{_{\rm T}}(\boldsymbol{X})\left(\mathcal{H}-E_{\rm ref}\right)\frac{f(\boldsymbol{X},\tau)}{\Psi_{_{\rm T}}(\boldsymbol{X})}
\end{aligned}$$

Using the explicit form of the Hamiltonian (3.1), the evolution of f can be rewritten (see details in Appendix A) as

$$\frac{\partial f}{\partial\tau} = \sum_i \frac{\hbar^2}{2m_i}\left[\nabla_i^2 f - \nabla_i\left(f\nabla_i \ln|\Psi_{_{\rm T}}|^2\right)\right] - \left(\frac{\mathcal{H}\Psi_{_{\rm T}}}{\Psi_{_{\rm T}}} - E_{\rm ref}\right) f \qquad (3.6)$$

Lets interpret the above equation by considering f as a density function in the configuration space $\boldsymbol{X}$ consisting of all the particle coordinates in the system. Further imagine that this function is represented by an ensemble of points defined in this space with density f. We will refer to them as system points, or walkers. Each term of Eq. (3.6) can be simulated by an operation on such an ensemble. The operations are independent between system points and do not depend on past history. The first term corresponds to diffusion with diffusion coefficients $\hbar^2/2m_i$ for directions corresponding to i-th particle

in the configuration space. The second term (under the sum) corresponds drift of the points representing f with a velocity field $\nabla \ln |\Psi_{\mathrm{T}}|^2$.

While the first two terms on the right-hand side of (3.6) conserve the norm of f, the last term does not. It represents a source or sink for points representing f according to the "local energy" $\mathcal{H}\Psi_{\mathrm{T}}/\Psi_{\mathrm{T}}$ of the trial function. This term is called branching. In order to account for the branching term, a point may be removed, stay in the system, or be replicated by adding another point with the same position. Therefore the total number of points is constantly changing. Tuning the value of E_{ref} to find the value at which the number of system points is at a steady state allows one to find the ground state energy of the system. At such a value of E_{ref}, the local density of system points is representing the ground state wave function according to (3.5). Such an interpretation allows a stochastic representation of the evolution by a Markov chain generated with a Monte Carlo approach. System points diffuse, drift and branch according to Eq. (3.6). The limit of large imaginary time is achieved by repeating the evolution equation multiple times with a small timestep. This constitutes the DMC method.

A steady state for the population of system points in this context is a state that does not exhibit systematic drift toward either increased or decreased population. However, the net number of walkers will inevitably fluctuate and in general is not bound from either top or bottom. Further details on handling the branching term are given on p. 57.

The trial function Ψ_{T} 'guides' the ensemble by means of the drift term,

assuring that only regions of space where Ψ_{T} is not small are being sampled. Regions of space where Ψ_{T} vanishes are prohibited because the logarithmic derivative in (3.6) will necessarily diverge, driving the system points away. Importance sampling turns out to be essential for systems with a large number of particles such that only small regions of the configuration space should be sampled while sampling the entire space is not feasible computationally. In a DMC calculation, the choice of the trial function determines a problem that is being solved together with the interaction potential. This trial function is typically obtained from previous variational calculations and physical models for the problem at hand.

3.5 Calculating observable expectations with DMC

Operator estimators

A desired outcome of a quantum ground state simulation is obtaining observable values. In case of DMC, these are called *pure* estimators for an observable A:

$$\langle A \rangle_{\mathrm{p}} = \frac{\langle \phi_0 | \mathcal{A} | \phi_0 \rangle}{\langle \phi_0 | \phi_0 \rangle} \tag{3.7}$$

Evaluation of such quantities however is not always directly accessible[a]. Alternatively, biased expectation values of an operator in DMC can be evaluated by calculating values of the operator acting on the trial function, evaluated on configurations sampled with the algorithm. Values evaluated in such a way, when divided by values of the guiding function, are called local:

$$A_{\mathrm{local}}\left(\boldsymbol{X}\right) \equiv \frac{\mathcal{A}\Psi_{\mathrm{T}}\left(\boldsymbol{X}\right)}{\Psi_{\mathrm{T}}\left(\boldsymbol{X}\right)} \tag{3.8}$$

Because the system configurations sampled during the simulation are distributed according to $\phi_0\Psi_{\mathrm{T}}$, a run-time average of local values (3.8) approximates in the statistical limit what is termed mixed estimator

$$\langle A\rangle_{\mathrm{m}} = \frac{\langle\phi_0|\mathcal{A}|\Psi_{\mathrm{T}}\rangle}{\langle\phi_0|\Psi_{\mathrm{T}}\rangle} \tag{3.9}$$

Estimation of diagonal operator expectations in DMC

Ground-state eigenvalues of those operators that commute with Hamiltonian can be estimated with DMC *exactly* in the statistical sense (that is the computed value converges to the correct one in the limit of infinitely long projected imaginary time performed with infinitely small time steps on infinitely large ensemble of walkers), *and such estimates do not inherit a bias*

[a]The closest DMC comes to directly computing such quantities is in computing the ground state energy in *pure* DMC algorithm (PDMC), which is a simulation without importance sampling. Bias is introduced by the discrepancy between the trial function and the true ground state. Run-time average of stabilization energy directly yields a pure estimator for the ground state energy.

from the choice of the trial function. Indeed, consider estimation of some observable's operator $\mathcal{A}$ as an average of local values of this operator on the trial function evaluated on the set of configurations sampled by the method. Since the operator $\mathcal{A}$ commutes with the Hamiltonian, $\mathcal{A}$ can be expanded in its basis: $\mathcal{A}\left|\Psi_{\mathrm{T}}\right\rangle = \sum_i \left\langle\phi_i\right| \left.\Psi_{\mathrm{T}}\right\rangle \mathcal{A}\left|\phi_i\right\rangle = \sum_i \left|\phi_i\right\rangle \left\langle\phi_i\right| \left.\Psi_{\mathrm{T}}\right\rangle A_i$. Then

$$\begin{aligned}\left\langle \frac{\mathcal{A}\Psi_{\mathrm{T}}(\boldsymbol{X})}{\Psi_{\mathrm{T}}(\boldsymbol{X})} \right\rangle_{\mathrm{run}} \approx & \frac{\left\langle\phi_0\right|\mathcal{A}\left|\Psi_{\mathrm{T}}\right\rangle}{\left\langle\phi_0\right| \left.\Psi_{\mathrm{T}}\right\rangle} \\ = & \frac{\sum_i \left\langle\phi_0\right.\left|\phi_i\right\rangle \left\langle\phi_i\right| \left.\Psi_{\mathrm{T}}\right\rangle A_i}{\sum_i \left\langle\phi_0\right.\left|\phi_i\right\rangle \left\langle\phi_i\right.\left|\Psi_{\mathrm{T}}\right\rangle} \\ = & \frac{\left\langle\phi_0\right.\left|\Psi_{\mathrm{T}}\right\rangle A_0}{\left\langle\phi_0\right.\left|\Psi_{\mathrm{T}}\right\rangle} = A_0 \equiv \frac{\left\langle\phi_0\right|\mathcal{A}\left|\phi_0\right\rangle}{\left\langle\phi_0|\phi_0\right\rangle}\end{aligned} \tag{3.10}$$

(Approximation sign above signifies that the equality holds only in the statistical sense.) Hence if $[\mathcal{H}, \mathcal{A}] = 0$, then $\langle A\rangle_{\mathrm{m}} \equiv \langle A\rangle_{\mathrm{p}}$. In particular, the value of the ground state energy is not biased by Ψ_{T} . Results that are independent of the choice of the approximate wave function or other subjective parameters is perhaps the greatest strength of the DMC method.

However, estimation of eigenvalues of operators that *do not* commute with the Hamiltonian is much more involved.

Estimation of off-diagonal operator expectations in DMC: Extrapolated estimators

Calculating the run-time average of the 'local value' of an operator that does not commute with Hamiltonian yields a mixed estimator (3.9) which does

not asymptotically approach the exact quantum mechanical quantity. In fact such an estimate is only as good as the "quality" of the trial function. Assuming that the trial function is a good approximation for the ground state: $\Psi_{\mathrm{T}} = \phi_0 + \delta\Psi$, we can write (all function are real)

$$\begin{aligned}\langle \phi_0 \left| A \right| \phi_0 \rangle &= \langle \Psi_{\mathrm{T}} \left| A \right| \Psi_{\mathrm{T}} \rangle - 2\langle \delta\Psi \left| A \right| \Psi_{\mathrm{T}} \rangle + \langle \delta\Psi \left| A \right| \delta\Psi \rangle \\ &= 2\langle \Psi_{\mathrm{T}} \left| A \right| \Psi_{\mathrm{T}} \rangle - \langle \Psi_{\mathrm{T}} \left| A \right| \Psi_{\mathrm{T}} \rangle - 2\langle \delta\Psi \left| A \right| \Psi_{\mathrm{T}} \rangle + \langle \delta\Psi \left| A \right| \delta\Psi \rangle \\ &= 2\langle \phi_0 \left| A \right| \Psi_{\mathrm{T}} \rangle - \langle \Psi_{\mathrm{T}} \left| A \right| \Psi_{\mathrm{T}} \rangle + \langle \delta\Psi \left| A \right| \delta\Psi \rangle\end{aligned}$$

Presuming that $\delta\Psi$ is small in some sense, we can use the first two terms on the right side to compute to the second order in $\delta\Psi$ an approximation for the pure estimator which is called the extrapolated estimator [14, 66]:

$$\langle A \rangle_{\mathrm{e}} = 2\langle \phi_0 \left| A \right| \Psi_{\mathrm{T}} \rangle - \langle \Psi_{\mathrm{T}} \left| A \right| \Psi_{\mathrm{T}} \rangle = 2\langle A \rangle_{\mathrm{m}} - \langle A \rangle_{\mathrm{v}} \tag{3.11}$$

The utility of such a procedure lies in the fact that both terms on the r.h.s. of the equation above are readily available. $\langle A \rangle_{\mathrm{m}}$ is the mixed estimator from DMC calculation, and $\langle A \rangle_{\mathrm{v}}$ is the estimator one obtains for an observable $\mathcal{A}$ with variational calculations if using Ψ_{T} as the variational wave function (Sec. 3.2). Such a calculation can be in fact readily performed with the DMC code by disabling the branching stage. The algorithm then samples Ψ_{T}^2 and not $\phi_0\Psi_{\mathrm{T}}$, but with Fokker-Planck sampling (Sec. 3.3).

The level of improvement achieved with estimators (3.11) is hard to quan-

tify and to control as the level of correction depends not just on the "goodness" of Ψ_{T} but also on the particular form of the operator that is being evaluated. An easy way to see the kind of problem one gets with extrapolated estimators is to consider expectation values of the energy. As noted before (Eq. 3.10), the mixed estimator of energy in fact yields the correct (pure) estimator, i.e. $\langle H \rangle_{\mathrm{m}} = \langle H \rangle_{\mathrm{p}}$. Attempting an extrapolated estimator for energy $\langle H \rangle_{\mathrm{e}} = 2\langle H \rangle_{\mathrm{m}} - \langle H \rangle_{\mathrm{v}}$ yields a result that is in fact biased by the trial function. It can be intuitively understood that the quality of mixed estimates is better for operators which have large commutators with Hamiltonian such as functions of position alone.

Estimation of off-diagonal operator expectations in DMC: Unbiased estimators

It was found by Liu et al. [79] that the asymptotic number of offspring eventually generated by a walker originally located at some position $\boldsymbol{X}$ is equal to the ratio $q = \phi_0(\boldsymbol{X})/\Psi_{\mathrm{T}}(\boldsymbol{X})$. By collecting these asymptotic population results and then using these *numbers* as weights when computing operator expectation on configurations drawn from the original set of $\boldsymbol{X}$, one obtains the *unbiased estimator*

$$\langle A \rangle_{\mathrm{u}} = \frac{\left\langle \phi_0 \left| \mathcal{A} \, \frac{\phi_0}{\Psi_{\mathrm{T}}} \right| \Psi_{\mathrm{T}} \right\rangle}{\left\langle \phi_0 \left| \frac{\phi_0}{\Psi_{\mathrm{T}}} \right| \Psi_{\mathrm{T}} \right\rangle} = \frac{\langle \phi_0 \, | \mathcal{A} | \, \phi_0 \rangle}{\langle \phi_0 | \phi_0 \rangle} \tag{3.12}$$

The sampling has to be done on multiple sets and the correct amount of time that has to be allowed to pass before the "asymptotic" number of descendants is recorded is somewhat of an art, at least in this original approach. Various tagging algorithms may be constructed to count the asymptotic number of descendants [80–83], in methods generally known as forward walking algorithms. Because the number of descendants is a fluctuating quantity, such estimates are known to be computationally expensive and may be unreliable. Scale of this problem is easy to appreciate if one considers that given sufficient time, only one of the current walkers will be the parent to the entire future ensemble. Descendant information from all the other walkers will be therefore zeroed and lost, and the number of descendants from the parent walker will be biased ever more strongly by the population stabilization. In practice we observe that the timescale for this 'common ancestor' phenomenon is much shorter than a typical simulation. The implication is that the time for which the walkers should be allowed to reproduce before the number of the descendants is recorded is selected individually for each problem. The setup has to accommodate a tradeoff between the need to make this time long enough to achieve asymptotics, and the need to have it shorter than the time to common ancestor.

Casulleras and Boronat proposed [84, 85] a method for computing the descendant weights on the fly, without building branching tables to be analyzed after the calculation. In their method, local values of observables (3.8) are passed to descendant walkers and added to whatever values these

descendant walkers incur as they sample the space. After appropriate normalization, these values properly take account of descendant weights and result in unbiased estimators (3.12). Though more reliable than the previous methods, computing estimators with this scheme requires breaking the simulation into accumulation and "equilibration" stages which have to be selected by hand.

Unbiased estimators computed by the scheme of Casurellas and Boronat are established for computing expectation values of diagonal operators. However, they can only take account of operators that are local in $\boldsymbol{X}$, making them inappropriate, for example for calculating the condensate fraction.

In our scheme for the transmission calculation, the energy is found as a function of the boundary conditions imposed on the calculation by the trial function. These are exact in the sense that they an external input to the problem. At the same time, we are looking for energy which is best calculated with the mixed estimator form (which for energy in particular gives the unbiased estimator as shown in Eq. 3.9). We carefully considered using unbiased estimators in our calculations, but doing so would require is some sense inverting the problem. Such approaches are not available. While the developed code has some ability for computing unbiased estimates, this was not used or extensively tested.

3.6 Considerations and practicalities for DMC simulations

Overview

The DMC algorithm, as it is formulated for ground state of bosonic systems, is an exact method in statistical sense and should provide us with correct answers for the ground state energy regardless of our input in the form[b] of the trial (importance sampling) function and its parameters. However, the formulation of the method requires among other things the following:

1. The net projection (imaginary) time must in principle be infinite.

2. The imaginary time step for projecting the state must again in principle be infinitely small.

3. If branching is used, the number of walkers used for the simulation must not be bound. (Branching is necessary as divergent errors will otherwise result; see p. 57.)

Significantly violating any of these condition may not only worsen the statistics, but may also bias the results. Implications of these requirements are discussed below.

[b] It is required that the trial function overlaps with the ground state, but this is a condition easy to satisfy if only due to numerical round-off fluctuations. In gravest cases it is therefore hypothetically, if not practically, still just a question of projecting the system long enough. It is also required that $\Psi_T \neq 0$ where $\phi_0 \neq 0$.

Choosing projection time

Condition 1 from the above list signifies that runs have to be monitored to ensue that a steady distribution of walkers has been achieved, the memory of the initial conditions has been wiped out, and all relevant quantities are randomly wandering about their mean values from that point forward. Information should only be accumulated after this initial "equilibration" period. Using an overall too short a projection time or accumulating values too early will introduce bias from initial conditions.

On the other hand, improving the initial conditions will shorten the time it takes for the system to "equilibrate" and will speed up the execution allowing for longer "useful" parts of the calculation. In our calculations, we used a set of walkers $\{\boldsymbol{X}\}$ sampled from a distribution proportional to $\Psi_{\mathrm{T}}^2(\boldsymbol{X})$ with preliminary Metropolis sampling steps[c] (Sec. 3.2). Input to the Metropolis sampling was in most cases simply an fcc lattice best filling the appropriate volume, with one added small random displacement of the atoms from the lattice sites. Assuming Ψ_{T} is our best (yet computationally affordable) guess for the ground state, it should take the least amount of time for the distribution of system points to move from the distribution characteristic of Ψ_{T}^2 to the distribution characteristic of $\phi_0\Psi_{\mathrm{T}}$ once the DMC starts. The effect of Metropolis stage was especially important in the transmission simulations (Ch. 6). The nodal nature of the trial function used in these calculations

[c]Input from this stage was also used to monitor VMC energies of our wavefunction model.

results in local energy values and drift velocity that can vary greatly and assume extreme values. Using the Metropolis stage for initial conditions removed the problem of massive population fluctuations in the beginning of the simulation and therefore shortened the equilibration period.

Choosing time step and convergence scheme

The imaginary time step is the small parameter in the DMC method. The "smallness" of the time step is used twice. First time it is used to approximate the Green's function corresponding to importance sampling, and the second time it is used to decompose the evolution operator into separate algorithm steps, for example by choosing $\mathrm{e}^{\hat{K}\Delta\tau+\hat{V}\Delta\tau} \approx \mathrm{e}^{\hat{K}\Delta\tau}\,\mathrm{e}^{\hat{V}\Delta\tau}$. For this reason, the smaller the time step, the more accurate is the simulation. At the same time one wants to project the system as far as possible in the imaginary time (to better project out the excited states). This leads to trade off between choosing smaller timestep or longer projection time which has to be determined separately for each particular problem.

The traditional DMC algorithm is outlined in Table 3.1. It relies on decomposition of the evolution equation in the already mentioned form $\mathrm{e}^{\hat{K}\Delta\tau+\hat{V}\Delta\tau} = \mathrm{e}^{\hat{K}\Delta\tau}\,\mathrm{e}^{\hat{V}\Delta\tau}$, is correct only to the first order in $\Delta\tau$. This can be immediately seen from Campbell-Baker-Hausdorff (CBH) formula:

$$\mathrm{e}^{A}\,\mathrm{e}^{B} = \exp\left(A + B + \frac{1}{2}[A,B] + \frac{1}{12}\left[(A-B),[A,B]\right] + \cdots\right)$$

In our case A and B are operators corresponding to kinetic and potential energies each multiplied by small parameter $\Delta\tau$. Therefore the second term (commutator) in the l.h.s. of CBH relation (which is effectively discarded in DMC) is of order $\Delta\tau^2$. Additionally, the importance sampling step which is done with Langevin algorithm (see Ref. [67]) is also simulated only to the first order in $\Delta\tau$. For these two reasons DMC algorithms tended to be in a way notoriously first-order despite attempts to improve the convergence. With this standard form one needs to perform several calculations with varying time step and extrapolate for $\Delta\tau \to 0$.

Table 3.1: Outline of a standard DMC algorithm step which has linear convergence with imaginary timestep.

0. Store local energy value E_i (may be used from the previous step). Compute the drift velocity and make a full drift step.
1. Make a full diffusion step. The new position is final.
2. Record energy in the final position E_f. Use $\frac{1}{2}(E_i + E_f)$ for local energy in the branching term. Refresh branching weights.
3. Perform reweighting by branching and any necessary data accumulation. Return to step 0.

Numerous attempts were made to develop DMC algorithms with higher order of convergence. This would ease the trade off between shorter steps and longer total projection time and would effectively allow for simulations

of larger systems and more complex problems[d]. Most of these methods work only for rather specific problems. The only two methods that proved themselves with time are the step rejection methods and second order decomposition of the evolution operator.

Rejection methods combine the Fokker-Planck sampling methods of DMC with the importance sampling of Metropolis (see Ref. [67], section 2.2.3). A step is made according to the usual drift scheme but may be rejected if the trial function is small in the new location. These methods often suffer from locked configurations with particles remaining at the same location because of repeated rejection events. This is a notorious problem for models with nodal wavefunction like the one which we are using for the transmission simulation (see Ch. 6; the moves have to be rejected on each node crossing). Our tests with a simple transmission model indeed showed very persistent locked states.

Chin proposed [86] three second order decompositions of the evolution operator. These algorithms address both the problem of decomposing the evolution operator and of simulating the importance sampling stage to the second order. The first one, labeled as DMC 2a in Chin's nomenclature, has been found to be most reliable (although more costly computationally) and has been since tested on various systems including helium [76, 77, 85, 87].

[d] Another argument put against first order algorithms is often as follows. Assume the calculation accumulates in some sense an error proportional to the time step at each time step: $\Delta \propto \alpha\Delta\tau$. If there's no cancellation, then the net error for given full simulation time T is equal to $N \times \Delta = {}^{T}/_{\Delta\tau} \times \alpha\Delta\tau = \alpha T = \text{const}$. That is, such portion of the error does not reduce regardless of how small a step one takes.

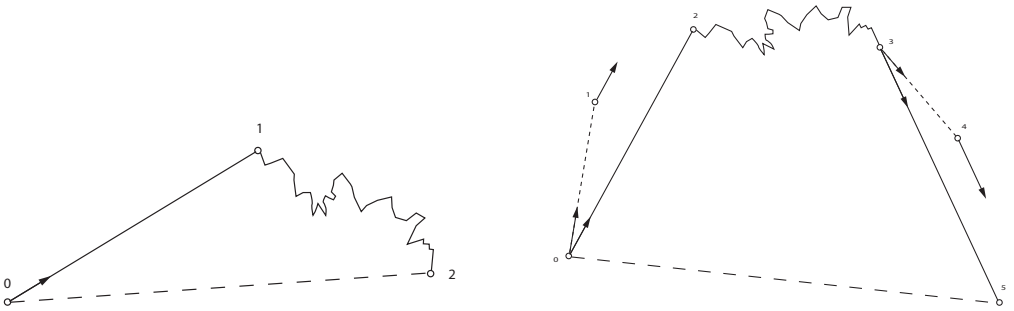

Figure 3.1: Schematic diagrams for traditional (left) and second-order (right) methods which we used, as explained in the text. Straight solid line denotes drift steps. Short-dashed line labels trial steps. Vectors stand for direction of the "quantum force". Dashed line signify that values of local energy at the points that it connects are used for the branching term. Wiggly line depicts the diffusion stage.

Decompositions up to fourth order were also proposed in later works [88, 89] and are yet to be tested in various many-body problems. Because of possible instabilities at large timesteps, it appeared not to provide improvement beyond the second order algorithm and so these methods were not used. One should refer to [86] for derivations and detailed explanation of the second order algorithm. The simulation stages are listed in Table 3.2 and are symbolically shown in Fig. 3.1 along with traditional DMC. We used the second order algorithm for most of the simulation results shown in the following chapters. However some of the early tests were done with regular DMC.

We verified that this approach indeed yields second order convergence, including the transmission simulations. Typical results are shown in Figs. 3.2 and 3.3 for a simulation of bulk He. Projection time in these tests was fixed with smaller timestep calculations taking considerably more computer time

Table 3.2: Outline of a DMC algorithm which has second order convergence with imaginary timestep.

0. Begin at some position x_0. Store local energy value E_i (may be used from the previous step). Compute the drift velocity v_0 and make a drift step corresponding to a quarter of actual timestep to position $x_1 = x_0 + \frac{1}{4}v_0\Delta\tau$.

1. In this new position compute drift velocity v_1.

2. Return to previous position and make step corresponding to the drift velocity computed in the intermediate position and half time step: $x_2 = x_0 + \frac{1}{2}v_1\Delta\tau$

3. Make the diffusion step corresponding to full timestep to position x_3.

4. Repeat steps 0–2 by making a trial quarter drift step, returning and making a half drift step with the intermediate drift velocity.

5. Refresh weights and perform branching steps if necessary. Energy E_f at this final position is used together with E_i in the branch term as $\frac{1}{2}(E_i + E_f)$ for local energy. Return to step 0.

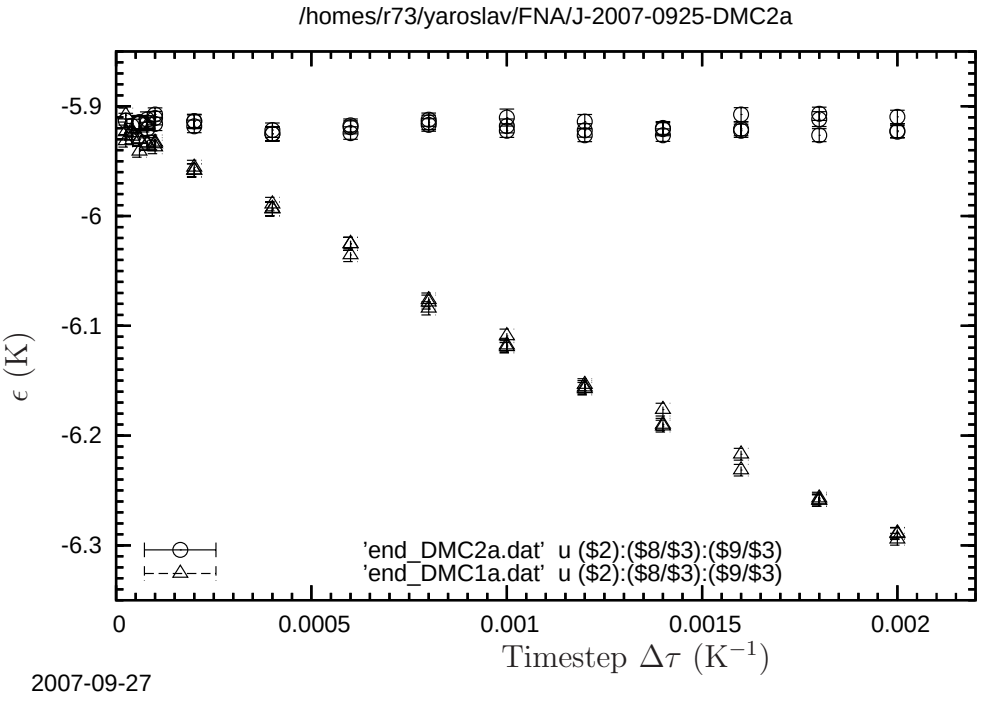

Figure 3.2: Energy per atom vs. imaginary timestep for different DMC algorithms: standard DMC (triangles) and DMC 2a (circles).

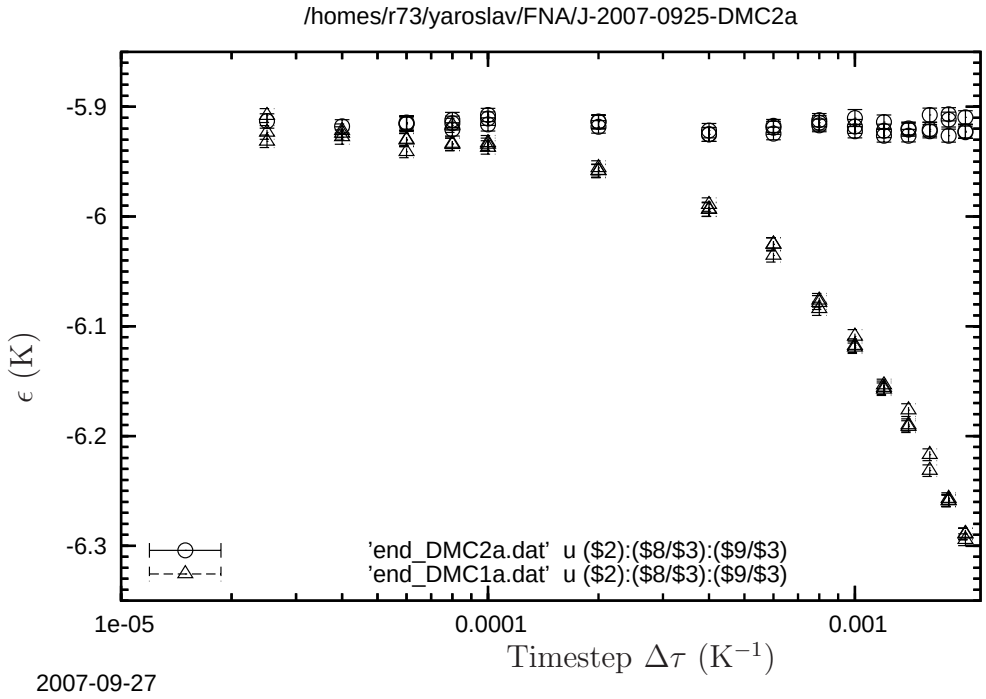

Figure 3.3: Energy per atom vs. imaginary timestep for different DMC algorithms: standard DMC (triangles) and DMC 2a (circles). This is a portion of the data from figure 3.2. Logarithmic scale allows to better spot the convergence point.

than the ones with large $\Delta\tau$. The calculations with smaller timestep provide the correct answer, while a significant linear bias can be observed at large timesteps for the first order method. Convergence of linear and quadratic results at small timesteps can be observed in Fig. 3.3. When the net *computer* time is fixed instead, the runs with smaller timesteps experience fluctuations due to small projection time and one observes a region in the intermediate values for the timestep where the normal calculation needs to be performed. This window is much larger for the second order algorithm. We used a small system for these tests which is a reason why the energy does not reach correct binding energy of 7.17 K per atom. Similar although not as detailed tests were performed before the transmission simulations.

Choosing and maintaining walker population

Assigning weight to each system point (we will sometimes abbreviate system points to "s.p.") according to the branching factor given by the last term in the evolution equation (3.6) is an essential part of DMC. Without it, the procedure becomes simply a Fokker-Planck sampling of the square of the trial function. That is, without the branching term the results have provide the variational estimate for energy (Sec. 3.2). Using too small a population for a particular problem introduces a bias in the results which becomes more severe as the population decreases. This is illustrated in Fig. 3.4 for a test bulk simulation. (Energy never reaches true chemical potential for bulk He because of finite size effects in this small system). As can be seen from

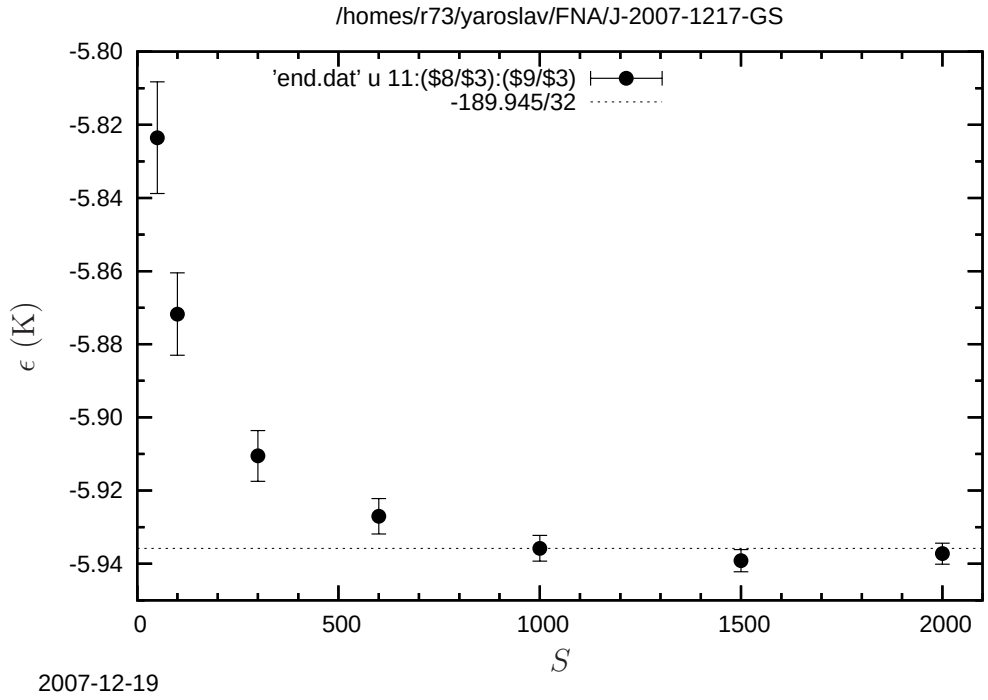

Figure 3.4: Energy per system point for different maximum number of system point. Dotted line is guide for the eye. It passes through value of energy for calculation with population threshold equal to 1000.

this test, there's a threshold population above which the algorithm begins to work properly. This threshold has to be determined separately in each case and depends among other things on complexity of the energy landscape and quality of the trial function.

The direct approach to keep track of reweighting is to track the weight of individual system points:

$$w_i(t_n) = \prod_{j=1}^{n} \exp\left[-\left(\frac{\mathcal{H}\Psi_{\mathrm{T}}\left(\boldsymbol{X}_i(t_j)\right)}{\Psi_{\mathrm{T}}\left(\boldsymbol{X}_i(t_j)\right)} - E_{\mathrm{ref}}(t_j)\right)\Delta\tau\right]$$

where i refers to walker's index and t_j to the imaginary time slice, imaginary timestep $\Delta\tau = t_j - t_{j-1}$. These weights could be used to compute averages of observables as

$$\mathcal{A} = \left\langle \frac{\sum_i w_i \mathcal{A}_i}{\sum_i w_i} \right\rangle_{\text{run}} \tag{3.13}$$

Because each s.p. samples the space independent of its past history, it's weight will fluctuate. More rigorously, $\log w_i$ will perform a random walk in one dimension. This random walk is unbound, and therefore the dispersion of the distribution of weights among the ensemble of system points will tend to infinity as the run proceeds. While the estimate (3.13) should in principle yield correct result, it will fluctuate and the error in this estimate will tend to infinity rather quickly as the run proceeds.

To remedy this, *branching* of system points is employed. At some intervals (possibly every step) the evolution is stopped and branching is applied to each system point or to the ones which accumulated extreme values of weight. Each system point is replaced by stochastically chosen number of its own replicas. The probability of this number equals to the previous weight of the parent. The width and form of the distribution of stochastic variable that is used to select the number of replicas (or offspring) is not pre-determined. It is however reasonable to choose as narrow a distribution for the number of offspring as possible. Usually, the following approach is used:

1. Let the weight w be written as $w = n + r$ where $n \equiv \lfloor w \rfloor$ is largest integer smaller or equal to w.

2. Select a random number ξ uniformly distributed on $[0, 1]$. If $\xi \leq r$ then the number of offspring's is chosen as $n + 1$, otherwise it is set at n.

It is easy to see that this indeed yields the correct expectation for the number of offspring. The above two steps are equivalent to choosing $\lfloor w + \xi \rfloor$ as the number of offspring. This is the procedure which we followed. Results presented in this work had branching performed immediately after every step for all system points.

The weights of all the offspring are set to unity. For this reason we sometimes refer to branching as *reweighting*.

If the reference energy is chosen improperly, the number of system points will drift to either extreme. However, even if the reference energy is chosen correctly, number of system points that are constantly copied or removed is a fluctuating quantity. Without any feedback, this number performs a random walk and is bound to either collapse or diverge. For this reason the population of system points has to be stabilized. Stabilization is done by adjusting the reference energy. The common way to do this [90] is by setting

$$E_{\text{ref}} = \langle E_{\text{L}} \rangle + \Upsilon \log \frac{S^*}{S} \tag{3.14}$$

where $\langle E_{\text{L}} \rangle$ is average of the local energy during the run up to that step, S^* is the desired average number of system points and S is their count at a given step. Parameter Υ should be made as small as possible and is chosen empirically.

When the population reaches preset (hi and low) limits, it may need to be adjusted momentarily by either removing or adding system points (by branching the existing ones). This is fully equivalent to momentarily adjusting the reference energy. To perform this procedure, we adjusted the weights according to $w_i^* \rightarrow w_i \times \exp(\zeta\tau)$, where parameter ζ is the adjustment and has to be solved for to produce the desired number of system points. With a pre-drawn vector of random variables $\{\xi_i\}$, the new populations is again given by $\sum_i \lfloor w_i^* + \xi_i \rfloor$. The parameter Υ in Eq. (3.14) is chosen to be as small as possible without allowing too many sudden population adjustments.

In the course of developing the code, we have experimented with several models for population stabilization. It was found that, within a reasonably large window of parameter and adjustment scenarios, the final answers for energy were unaffected within the uncertainties. The outcome was by far more sensitive to having large enough population. However, extreme values of Υ and some extreme scenarios did turn out to bias the results, sometimes to the point of making extraction of the results impossible.

Effect of the trial function on the simulation

Nodes in the trial function can determine the conditions of the problem that is being calculated (i.e. fermionic vs. bosonic symmetry etc.), but apart from that its main purpose is guiding the importance sampling. The closer the trial function is to the actual ground state, the easier it is to perform DMC calculation. The quality of the trial function effects all the points from the

list on p. 48:

1. If the overlap between Ψ_{T} and excited states is already small, then it will take less imaginary time to project these out down to some given tolerance. That is, the requirement on the total length of imaginary time is smaller.

2. The accurate Ψ_{T} means that the time steps can be made larger. It is sufficient to consider that the branching will be small and with $\Psi_{\mathrm{T}} \approx \phi_0$ the importance sampling is only necessary for computational speed but not the accuracy. Sampling ϕ_0 even with Metropolis sampling would give the right answer!

3. If reference E_s is at the correct ground state energy E_0 and $\Psi_{\mathrm{T}} = \sum_{i=0} \alpha_i \phi_i$ then the branching term becomes

$$\frac{H\Psi_{\mathrm{T}}}{\Psi_{\mathrm{T}}} - E_s = \frac{\sum_{i=1} \alpha_i (E_i - E_0)\phi_i}{\Psi_{\mathrm{T}}}$$

   which vanishes as $\Psi_{\mathrm{T}} \to \phi_0$ and $\alpha_{i\neq 0} \to 0$. In other words, branching is infrequent for a good trial function and therefore the fluctuation in the number of system points is small. This means there's less need to stabilize the population and therefore less chance to introduce stabilization bias. This also means that smaller number of system points will be sufficient, making it is easier to meet the last condition of having sufficient number of system points.

Correcting for finite-size effects

In a typical simulation of the kind that we are performing, neither the trial function nor the interparticle potential vanish on the distances of largest particle separation (or of nearest-image separation in case of periodic boundary conditions). This leads to bias in the results for which one may try to correct [91]. Consider a bulk simulation with some cut-off length $L/2$ (which is the case if nearest image is used and the box side measures L). We can use a mean-field expression to correct for the potential energy as follows:

$$\frac{\Delta V}{N} = 2\pi\rho \int_{L/2}^{\infty} V(r) r^2 \, dr$$

where ρ is the density. In case the trial function is expressed as product of two-body correlation factors of the form[e] $f = \exp\{u(r)\}$, the correction to the kinetic energy is estimated by

$$\frac{\Delta K}{N} = -\frac{\hbar^2}{m} 2\pi\rho \int_{L/2}^{\infty} \left(\frac{2}{r} u'(r) + u''(r) \right) r^2 \, dr$$

The above equations imply that the rest of the energy is computed within a sphere of radius $L/2$. Actual bulk simulations are done in a cube and the volume accessible to nearest neighbor is also a cube with largest length equal to $\sqrt{3}L/2$. A proper correction therefore needs to take account of this extra volume, a procedure that does not seem to be mentioned by practitioners.

[e] This is usually referred to as the *pseudopotential* form.

Our slab geometry would require even more careful consideration. We used the correction equations to judge on the size of the effect, but the results presented here do not include any corrections.

It is a peculiar feature that the sum of kinetic and potential energy corrections may vanish by canceling at certain values of L (dependent on $u(r)$ and $V(r)$), even before each correction decays on its own.

3.7 Estimating run-time averages

Operator estimates are usually performed by collecting averages over a large part of the run. Successive DMC configurations are correlated, and so are the values to be averaged. To properly compute statistical errors in such an average, one needs to take into account that measurements are not independent. The square of the standard deviation of an average is in this case given [92, Section 4.2.4] by

$$\sigma^2_{\langle A\rangle} = \frac{\langle A^2\rangle - \langle A\rangle^2}{N}\left(1 + 2\frac{t_{\mathrm{A}}}{\Delta\tau}\right)$$

where N is the total number of measurements, $\Delta\tau$ is the timestep and t_{A} is the *relaxation time* for quantity A calculated from autocorrelation in series of measurements on A:

$$t_{\mathrm{A}} \equiv \int_0^\infty \frac{A(0)A(t) - \langle A\rangle^2}{\langle A^2\rangle - \langle A\rangle^2}\, dt \tag{3.15}$$

The autocorrelation usually fluctuates[f] at large times and so it is practical to select a cutoff at which to stop the integration. We usually summed to the point where the autocorrelation first becomes equal to zero. This was our preferred method of computing averages and all the results for energies were computed in this manner unless otherwise noted. An additional check [67,90] to verify that the procedure is performed correctly is to bin the data and then treat the average within each bin as an independent measurement. Once the bin size becomes much larger than the correlation time, the estimate on errorbars should stop depending on the binning. Too small a bin size corresponds to overestimating the number of independent measurements and hence underestimating uncertainties. This is demonstrated in Fig. 3.5. The example had a rather large relaxation time. It was an odd transmission simulation (see Ch. 6) with constrained center of mass which tended to behave this way. The simulation used first-order of convergence algorithm (see p. 50) and therefore had a small timestep.

In our transmission simulation we deal with trial functions that have nodes. Energy is ill-behaved near the nodal region. In fact the distribution of energies that can possibly be sampled during the simulation is not bound from either extreme. This invalidates a straight forward application of the Central Limit Theorem which is the foundation for the usual estimates of standard deviation such as Eq. (3.7). A leptokurtotic (with tails decaying

[f]Notice that the averages in Eq. (3.15) should be computed on the same sample as can be accessed by products $A(t_i)A(t_i+t)$ in the integrand. We found that this reduces the fluctuations considerably.

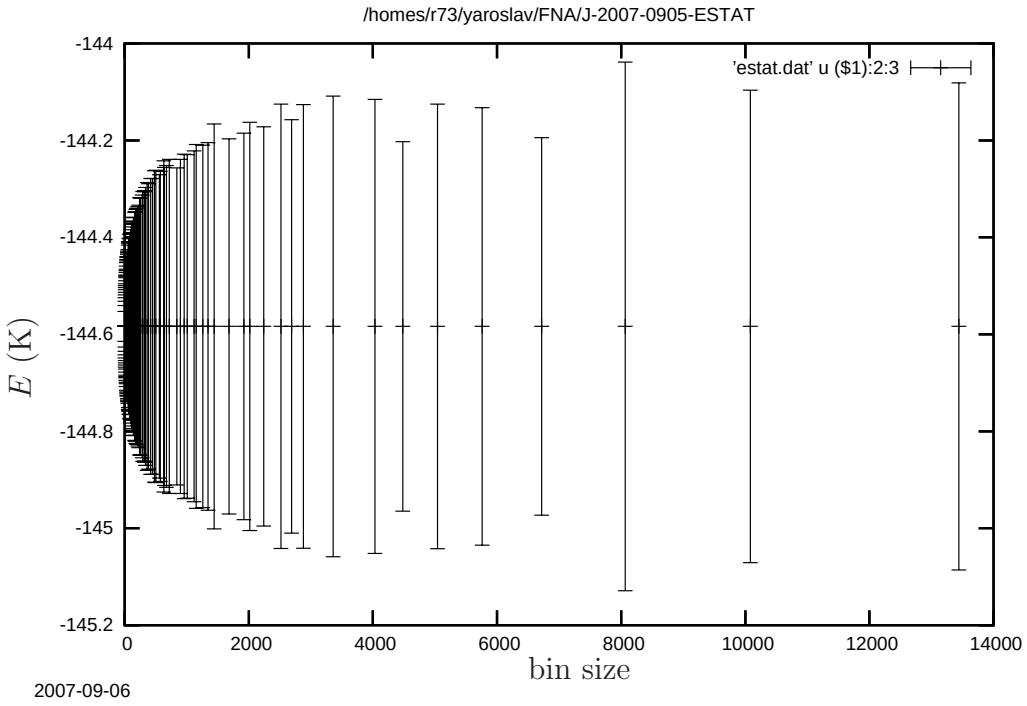

Figure 3.5: Error estimate for different rebinning of the same data.

slower than Gaussian) distribution of energy samples may lead to divergence of standard deviation estimates. However, weaker analogs of the central limiting theorem may still hold in these cases. See Ref. [93] for a study of this topic for variational calculations. We observed that the distribution of energies in the transmission calculations indeed had a non-Gaussian tails but that the consecutive measurements fell reasonably within standard deviation computed in the usual way of Eq. (3.7).

Our prescription for estimating statistical errors for energy averages was tested with a series of runs for identical system. The only difference between these runs was a different pseudorandom number sequence. Results are shown

in Fig. 3.6. The horizontal axis there is just an index used to identify the calculations. Values of energy are spread as indicated by error bars. The solid line indicates the weighted mean average for the entire set. A simple average computed from these points falls within one standard deviation from weighted mean (at this point we refer to the standard deviation of the mean itself), which is expected for large number of data points with close values of uncertainties.

The simulation was done on a bulk (uniform and periodic) helium system with only 32 particles, so size effect are significant and should be expected. Obtained values are therefore one degree above the expected value for chemical potential. (We used bulk helium density at zero vapor pressure for these simulations.) Values were not corrected for finite size effects. We used the McMillan form for the trial function (Eqs. 4.4, 4.5) and a Lennard-Jones potential with deBoer-Michels parameters (4.2). Each simulation used an average of 150 system points projected with second-order algorithm (p. 50) at time steps of 10^{-4} K^{-1} for a total of 5×10^5 steps, therefore projecting each system for 50 K^{-1}. Data was accumulated and used for analysis after 10 K^{-1}.

Reduced chi squared test for these results yields $\chi^2_{\mathrm{r}} = 0.47$ and likelihood close to 100%. For such a large number of points, this indicates that error bars are consistently overestimated, in fact by about 30%. However at this level of consideration, we should not expect to have error bar estimates be this precise. We therefore find this level of accuracy for the *error bar* esti-

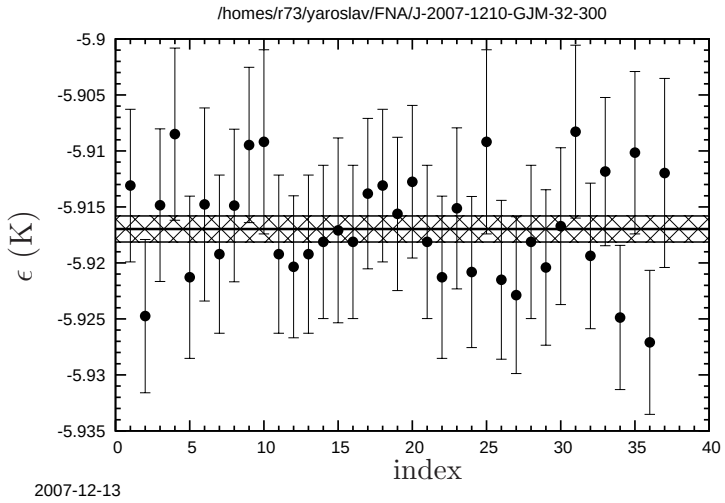

Figure 3.6: Energy and uncertainty for repeated simulation at equilibrium density performed with identical setups. Simulation only used 32 atoms. Markers: energy values with errors computed with relaxation time technique described in this section; solid horizontal line: weighted mean of these values; shaded area: one standard deviation values below and above weighted mean.

mates to be highly satisfactory. It is even more so for automatic calculations like this one. It is worth emphasizing that this approach utilizes as much data produced by simulation as possible (for estimating the errors) and still is capable of properly accounting for correlations in the data series. A more detailed algorithm would require taking into account the fact that the correlation times change during the simulation, and therefore different blocks of data should ideally be given different weight.

Chapter 4

Simulating He with DMC

4.1 Overview of available forms of potential for He

Accurate description of helium-II with quantum Monte Carlo methods relies on accurate knowledge of interaction energy. The lowest electronic excitation of a helium atom lies at 2.3×10^5 K above the ground state energy [94], therefore at these temperatures the atoms are very well represented as elementary particles. Taking into account that helium atoms have closed shells with only the s-orbital filled, the potential energy can be generally expanded as:

$$V(\boldsymbol{X}) = \sum_{i<j} V(r_{ij}) + \sum_{i<j<k} V(r_{ij}, r_{ik}, \angle(\boldsymbol{r}_{ij}, \boldsymbol{r}_{ik})) + \cdots$$

While certain calculations of helium properties require the three-body term (see Axilrod and Teller [95]) for the potential energy, keeping just the two-body term suffices for most calculations.

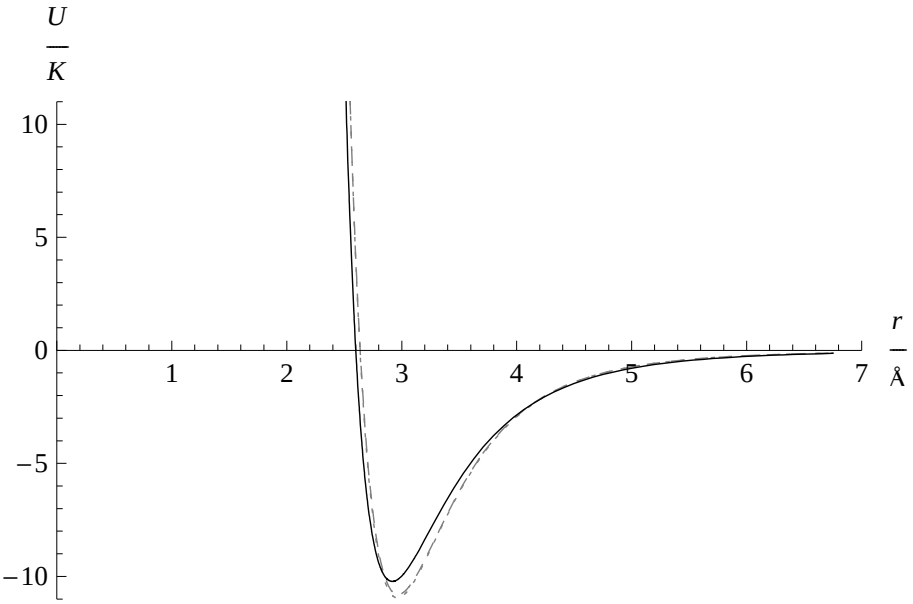

Figure 4.1: Helium interatomic potentials: Lennard-Jones with de Boer-Michels parameters (solid line), HFDHE2 and HFD-B(HE) (dashed and dotted lines) potentials.

The two-body interactions are remarkably well described with Lennard-Jones '6–12' potential [96] which is usually written in the form

$$V(r_{ij}) = 4\epsilon \left[\left(\frac{r_0}{r_{ij}} \right)^{12} - \left(\frac{r_0}{r_{ij}} \right)^{6} \right] \tag{4.1}$$

Parameters for the Lennard-Jones potential for helium were first derived by de Boer and Michels [97, 98] from atomic scattering data and are given

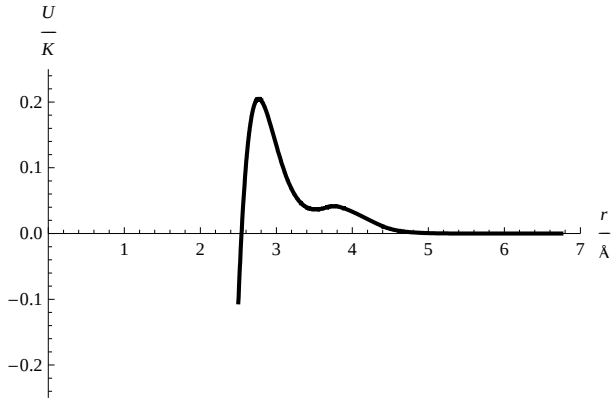

Figure 4.2: Difference between HFDHE2 and HFD-B(HE) potentials.

by[a] [99] as

$$\begin{aligned} \epsilon &= 10.22\text{K} \\ r_0 &= 2.556\text{Å} \end{aligned} \tag{4.2}$$

Description of helium-II with this potential gives quite satisfactory results as will be shown in the following section. However, early calculation with GFMC [14] have shown some discrepancy between calculation and experiment. An improved potential for interatomic interactions in liquid helium would inevitably include averaged effect of the surroundings[b]. Such new form of potential [100] was derived from a compilation of experimental and computational results by Aziz et al. This is commonly referred to as the HFDHE2 or Aziz-I potential. Later refinements to fit further calculations with the

[a]Original value for the "core size" r_0 was determined to within two significant figures as $r_0 = 2.6$Å.

[b]It is in principle possible to simulate the entire system as nuclei and electrons interacting with (precise but for relativistic correction) Coulomb interactions. However simulating a fermionic system of this kind and size with quantum Monte Carlo methods is impractical and has not been achieved so far.

Aziz-I potential [101] led to the HFD-B(HE) or so called Aziz-II [102] potential. The HFDHE2 and HFD-B(HE) potentials are similar and yield similar results with slight improvement for the second one. However, binding energy is overestimated with Aziz-II [77]. None of the subsequent refinements [103] to the potential form led to significant improvements in the simulations of the kind relevant to this work. These potentials have been extensively applied and tested in the GFMC and PIMC family of methods [77, 94, 104–106].

The Lenard-Jones, HFDHE2 and HFD-B(HE) are shown in Figure 4.1. The difference between the two Aziz potentials for helium in the significant range of atomic separations is shown in Figure 4.2. Both HFDHE2 and HFD-B(HE) potentials are given by the following form:

$$V(r) = \epsilon \left(A \exp\left(-\alpha x + \beta x^2\right) - F(x) \sum_{j=0}^{2} \frac{C_{2j+6}}{x^{2j+6}} \right)$$

where

$$x = r/r_m$$

and

$$F(x) = \begin{cases} \exp\left(-\left(\frac{D}{x} - 1\right)^2\right) & , \quad x < D \\ 1 & , \quad x \geq D \end{cases}$$

with coefficients given in Table 4.1.

Because of the simplicity and established reliability of Lennard-Jones form helium interaction, and because our investigation does not require extremely high energy accuracy at the present stage, we used this form of potential

Table 4.1: Coefficients for Aziz I (HFDHE2) and Aziz II (HFD-B(HE)) potentials.

	HFDHE2	HFD-B(HE)
ϵ	$10.8K$	$10.948K$
r_m	2.9673 Å	2.963 Å
A	0.5448504×10^6	1.8443101×10^5
α	13.353384	10.43329537
β	0	-2.27965105
D	1.241314	1.4826
C_6	1.3732412	1.36745214
C_8	0.4253785	0.42123807
C_{10}	0.1781	0.17473318

for our investigation. The superfluid fraction, static structure function and other characterizations of fluid are all quite well replicated with Lennard-Jones potential[c].

The main purpose of this work is to demonstrate a computational method and to determine the nature and an estimate of the probability of the transmission processes. For this purpose we found that the simple form of Lennard-Jones potential is sufficient. Unless otherwise specified, the interaction between helium atoms is assumed to be of two-body Lennard-Jones type with

[c]It ought to be noted that small corrections to potential and its maximum attractive strength become important in reduced geometries where the net binding energy is much smaller, and especially in He-3 systems, for which this difference determines whether a two-dimensional film [107–114] is a self-binding system [115–120].

de Boer-Michels coefficients (4.2).

4.2 Bijl-Jastrow wavefunction

The hard core of He-He interatomic potential, which makes perturbative approaches unreliable, does not pose a problem for microscopic Monte Carlo methods if a proper form of trial or sampling wave function is chosen. A successful trial function must vanish where atomic cores overlap. This condition is satisfied by choosing the trial function as product of two-body correlation functions, a form that was first introduced by Bijl [121]:

$$\Psi = \prod_{i<j} f_2 \left(r_{ij} \right) \tag{4.3}$$

Function f_2 vanishes when $r < \sigma$, σ being the "size" of the hard-core part of the interaction, or cross section. This form was later elaborated by Dingle [122] and Jastrow [123], and became known as the Bijl-Jastrow or simply Jastrow wave function.

The Jastrow wave function was used by McMillan [10] when he applied Metropolis [65] sampling methods to the problem of liquid helium in his foundational paper (Section 3.2). McMillan used the following form for the

Jastrow wave function[d]:

$$f(r) = \exp\left(-\frac{1}{2}\left(\frac{b\sigma}{r}\right)^m\right) \tag{4.4}$$

For $m = 5$ this form for f solves, to the leading order in r^{-1}, the Schrödinger equation for two particles in a system interacting with a Lennard-Jones potential (4.1). The result is that the expectation value of the energy varies more smoothly as two helium atoms approach each other during the simulation than it would with other values of m. In a diffusion MC calculation which samples situations where many such pairs exist in most configurations, large energy fluctuations would make these calculations impractical.

4.3 Test simulations of bulk helium-II

One of our first tests was a bulk helium simulation. Simulations included between 32 and 108 atoms in a periodic box at various densities. Interactions between atoms were described by the Lennard-Jones potential with de Boer-Michels coefficients (4.2), and the trial function was of Jastrow type as described above:

$$\psi_J = \prod_{i<j} \exp(-u_{ij}) \tag{4.5}$$

[d]Factor 1/2 is commonly used in the "pseudopotential" form to emphasize mapping onto thermodynamic problem. We will often incorporate this factor into function under the exponent, as specified.

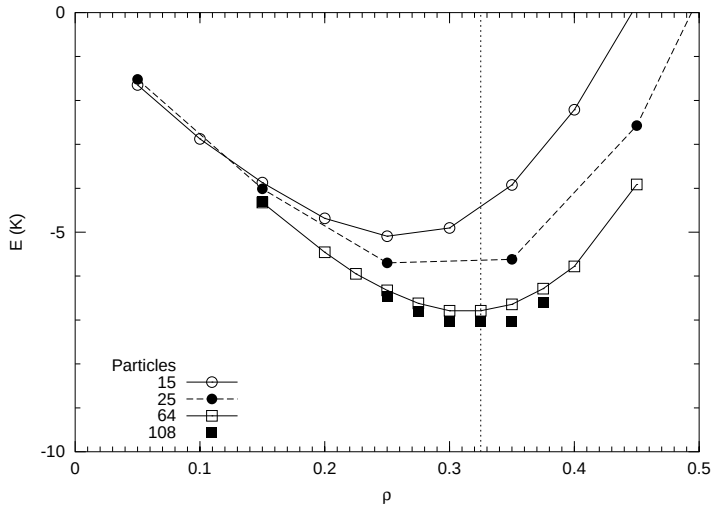

Figure 4.3: Computed dependency of energy per particle on density of the condensate for bulk periodic systems consisting of 15, 25, 64 and 108 particles. Lines are guides for the eye. Density of liquid helium is 0.325 in the used units, marked by the dashed line.

with

$$u_{ij} = \frac{1}{2}\left(\frac{a}{r_{ij}}\right)^5 \tag{4.6}$$

and a such as to solve to the two-body Schrödinger equation at small distance between atoms:

$$a = \left(\frac{8}{25}\varepsilon \Big/ \frac{\hbar^2}{2mr_0^2}\right)^{1/10} r_0 \tag{4.7}$$

where ϵ and r_0 are parameters for Lennard-Jones potential. For helium this yields $a = 2^{1/5}0.991r_0 = 1.138r_0$.

Results of these simulations are presented in Fig. 4.3. As expected, the energy diverges rapidly for large densities as particles are being pressed into each others core. The energy approaches zero for small densities. For sparse systems, values of energy are close for systems with different number of par-

ticles. This indicates that the size effects become unimportant at those densities, as one would expect.

Values of energy and the location of the minimum converge with increasing number of particles. The calculated minimum is between $\rho = 0.30$ and 0.35, expressed in reduced units that we find most convenient (unit of length ξ is such that its characteristic kinetic energy $\hbar^2/2m\xi^2 = 1$K for mass of ^{4}He atom; this yields $\xi = 2.4615$Å). In those units, the experimentally observed number density of liquid helium at zero temperature is 0.325 [34].

It should be expected that for small densities the particles will condense into clusters with densities corresponding to the minimum in energy. However the uniform state turns out to be metastable. The region to the left of the minimum of $E(\rho)$ corresponds to negative pressures which can estimated from[e]

$$P = \rho^2 \frac{\partial(E/N)}{\partial\rho}$$

Once the pressure becomes negative and low enough, the system reaches its spinodal point — the speed of sound $c = 1/\sqrt{m\kappa\rho} = 1/\sqrt{m(\partial\rho/\partial P)_T}$ vanishes and the system becomes unstable to infinitesimal fluctuations of density and should therefore collapse into droplets. That is, actual physical systems at negative pressure are metastable down to the spinodal point. The spinodal point for bulk helium-II at zero temperature is estimated to be at about $\rho = 0.23$ in our units. This is about the point where the $E(\rho)$ depen-

[e]Since all the calculations are done at the limit of zero temperature, it is appropriate to use isothermal thermodynamics expressions.

dence becomes linear in our test calculations. Helium has been observed to form clusters of very small number of atoms, and this behavior can be replicated with QMC calculation [76,124] so long as there is a way to sample such configurations. However, uniform-density quantum Monte Carlo calculations such as this one are typically metastable to much lower density so long as the guiding wavefunction does not provide a sampling opportunity for the collapsed state.

It should be pointed out that even for while the calculations presented in Fig. 4.3 manifest the minimum energy of about -7.2 K, there was no correction made for finite-size effects (p. 63) and even for the case of largest number of atoms in that simulation the finite-size effects may not be considered negligible. It is however the case that the kinetic and potential energy corrections cancel almost completely for the 64-particle arrangement.

Chapter 5

Simulating helium films

5.1 Guiding function for helium films

Constructing helium films is an important part of performing the transmission simulation. In this section I will discuss the trial function used for simulating helium films and which was also used as part of the transmission simulation's trial wave function.

The geometrical setup for film simulations was an elongated box with equal transverse dimensions. For the transverse direction, we used periodic boundary conditions everywhere. The problem by its nature called for films with two open surfaces and an unconstrained motion of the center of mass which would not be possible had we used a mirror image of half the film.

All the calculations involved pair-product wavefunctions just as for the bulk calculations (Section 4.3) to account for strong core repulsion between

helium atoms. This is a function of the coordinates of all the atoms.

It is possible with DMC to simulate a self-bound film with just the bulk term. Given box that is long enough, the longitudinal boundary is never reached in practice but it was also set with periodic boundary conditions. We found that such a simulation indeed yields a bound profile statistically. System points with configurations in which the film breaks into several chunks have higher energy due to the large open surface and eventually they either reconnect or are removed by the branching process.

We performed test simulations with helium films that were not forced to be bound by the trial function and observed that the density expectation was in fact a bound film of helium atoms. However encouraging, the results were not yielding sufficiently good qualitative results at that time. The binding energy was not high enough, and the density at the center of the profile did not quite reach the bulk value as one would expect. In order to obtain good statistics in this way we needed to perform rather long simulations. The quality of the results was also very sensitive to the width of the simulation box. Narrow and long films behaved much better than the wide ones which tended to break up more easily, as one would expect. Examples of resulting density profiles are shown in Figure 5.1.

These runs allowed us to test the profile function and to choose early test setups both for film and transmission simulation. In particular, the run in the figure 5.1 used transverse size of the box $L_\perp = 2.5\xi = 6.154$Å yielding a qualitatively "better" density profile than other geometries, most likely due

to better filling in the transverse direction (we use periodic boundary in the transverse direction). This dimension was chosen for most test simulations that followed and later was doubled as a starting point for 128-atom systems.

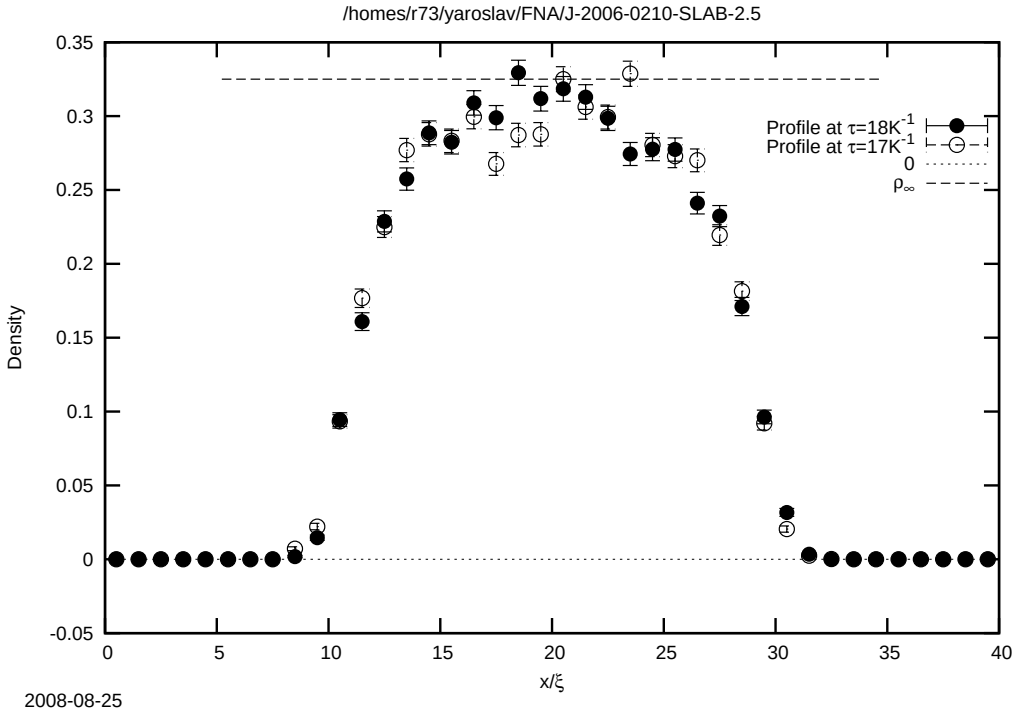

Figure 5.1: Example of density profile as resulting from unbound-film simulations. Open and closed circles show density at τ=18 and 17 K^{-1} correspondingly. Error bars correspond to (uncorrelated sample) statistical error during collection interval (each $1K^{-1}$). Error bars are underestimated demonstrating the extent of correlation in time series. Dashed line marks bulk helium density. Abscissa is coordinate in our reduced units ($\xi = 2.4616$Å).

5.2 Trial function for film simulations

Our simulations of the film allow us to adopt a guiding function that describes the results received from self-bound film simulations. Properly guiding the sampling in DMC speeds up the calculation significantly by lowering the required number of system points and net projection time. Using the profile was also important for the transmission simulations on their own.

Free surfaces of helium are believed to be best described by Fermi-like envelope functions [125]:

$$f_{\text{Fermi}} = \frac{1}{\exp\left(\frac{z-a}{b}\right) + 1} \tag{5.1}$$

at least inside and at close distance to the film[a]. Such envelope function can be used in a product of single-particle terms in the trial function of the DMC simulation to speed up execution. The trial function has the general form

$$\Psi_{\text{T}} = \Psi_N \prod_j f(z_j^*)$$

where z_j^* are the atom coordinates used for the slab profile which are coordinated to the center of mass:

$$z_j^* = z_j - z_{\text{c.m.}} = z_j - \frac{\sum_{i=1}^{N} z_i}{N}$$

[a]Is is also sometimes found that functions which are slightly asymmetric in the sense explained below may describe the film surface somewhat better.

and Ψ_N describes pair and other correlation effects between atoms. Ψ_N is normally identical to a trial wavefunction describing bulk systems as mentioned earlier.

The coordinates that are used for profile functions have center of mass coordinate subtracted from them everywhere, unless noted otherwise. This also applies to most of the work referenced in this Chapter.

5.3 Asymmetric profile envelope

Marín et al. [126] suggests possible asymmetry in the profile function. Asymmetry in this context should be understood as asymmetry in the profile function with respect to reflection about the point where the function reduces to half its value deep into the film. Marín used the usual Fermi-type trial functions and used the following expression to fit the density profile:

$$\rho = \frac{1}{\left(\exp\left(\frac{z-a}{b}\right)+1\right)^{\delta}}$$

Assuming that the pair correlations do not change the picture significantly, one expects $\rho \propto f^2$, which implies the usual symmetric form for f with $\delta = 2$. It was found that only films with large number of atoms (more than 162 in that study) should have resulting density profiles fitted with $\delta \approx 2$. In fact authors found $\delta = 1.91 \pm 0.15$ for large films. Smaller films were fitted with $\delta = 1$ which in turn implies that the optimized envelope may need to be

asymmetric. However the main conclusion seems to be that smaller systems did not allow to distinguish $\delta \neq 2$ from $\delta = 2$ with statistical significance.

Because any small asymmetry in the trial function can in principle be expanded, we experimented with modifying the trial function in the following way:

$$f = \frac{1 - c(z - z_{\mathrm{c.m.}})^2}{\left(\exp\left(\frac{z - z_{\mathrm{c.m.}} - a}{b}\right) + 1\right)}$$

where c can be of either sign. In fact the density profiles for rather small early simulations required non-zero value of parameter c to make satisfactory fits. However this form proved unsuitable and unnecessary for larger systems. All the results presented here used the equivalent of $c = 0$.

5.4 Selecting parameters for the profile trial function

Having an optimized form of f is important for good quality of the trial function. It is also important if using mixed or extrapolated estimators (Section 3.5) for quantities such as the border thickness of the film.

Krotscheck and collaborators found the optimized value of surface thickness parameter b in (5.1) to be equal to 1.33Å [118, 127]. This value is also consistent with the one found by Setty [36] in VMC calculation of the transmission process (see Sec. 2.5).

Various quantum Monte Carlo methods were applied to helium surfaces

in the past. Liu et al. [125] first performed variational calculations of helium surface. Later, Vallés and Schmidt [128] used GFMC to describe this problem. Marín et al. [126] simulated helium films with DMC. All of these works employed Fermi-like functions in the trial function. Lennard-Jones and both HFDHE2 (Aziz-I) and HFDHE2 (Aziz-II) potentials were used correspondingly in [125], [126, 128] and [126].

Recent experimental data [129, 130], microscopic simulations of helium surface [126, 131] and DFT calculations [132] suggest that the 10–90% thickness of the helium films ranges between 4.5 and 6.5Å. This is defined as distance between locations in the surface density profiles where the density reduces from 0.9 to 0.1 fraction of the bulk (or deep inside the film) value. Assuming again $\rho \propto \Psi^2$, Eq. (5.1) suggests that 10–90% width W of helium surface is given by

$$W = b \log \left[3 \frac{\sqrt{10} - 1}{\sqrt{10} - 3} \right] \approx 3.7b$$

and therefore existing works suggests values for b in the range between 1.2 and 1.8Å or slightly larger. In units used in our simulation[b], this corresponds to $b \sim 0.5\xi$ to 0.7ξ. It is also worth pointing out that in the DMC calculation of Marín et al. [126], the width obtained for systems with smaller number of atoms which was even smaller than this range.

The single-particle slab envelope function that we use in most of our

[b] Unit of length $\xi = 2.4616$Å

calculations has the following complete form:

$$f = \frac{1}{\left(\exp\left(\frac{z - z_{\mathrm{c.m.}} - a}{b}\right) + 1\right)\left(\exp\left(\frac{-z + z_{\mathrm{c.m.}} - a}{b}\right) + 1\right)} \tag{5.2}$$

The "steepness" parameter b which was used varied between 0.5Å and 1.5Å for different calculations. The size was chosen with the consideration that the density inside the slab should normally reach bulk values. It therefore depends on number of particles and transverse size of the system. Typical size of the slab was between $2a = 40$ and 60Å.

Fig. 5.2 shows results for density profiles for a few runs. These calculations used 128 particles. The difference between the two calculations is the "steepness" of the border in the trial function envelope. Despite having a constant density profile, the density does not reach the s.v.p. value inside the slab. The form of trial function used for these calculations is also shown on these graphs. The function was scaled to a point on density profile for convenience (they have different units). Despite the density being too low, these profiles tend to extend beyond trial function's profile. A wide range of trial function parameters was used in that calculation all leading to a similar outcome. We believe this is due to the finite size effects in the transverse direction[c]. If the transverse size of the system in not congruent with some

[c]The filling in the cross section plane was estimated to be 4×4 atoms. Because a reasonable slab depth is needed for transmission calculations, we cannot afford to increase the transverse size significantly beyond this number. The required number of atoms scales as square of the transverse length of the system box and the computational time scales as square of number of atoms at best.

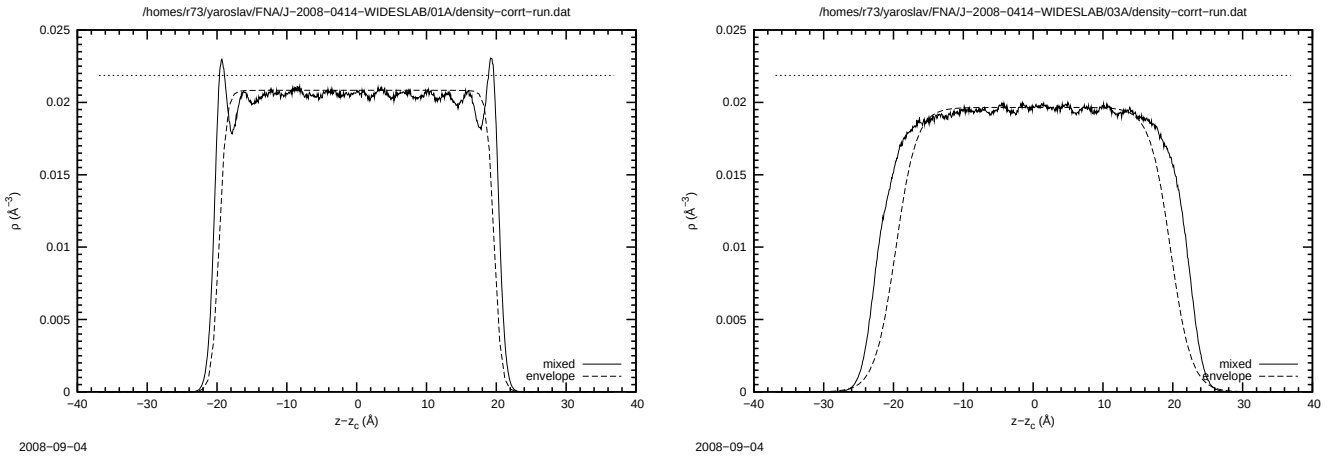

Figure 5.2: Mixed density estimates for different envelope parameters. The width was set to $2a = 39.4$Å for both simulations. Steepness parameter b was 0.5Å (right figure) and 1.5Å (left figure). Short-dashed line corresponds to bulk s.v.p. density. Dashed lines show corresponding envelope functions. They are scaled to the same height as the density profiles to better guide the eye.

ideal interparticle spacing, one would expect to observe similar effects. Varying the transverse size indeed allowed us to manipulate the density. The best results in terms of filling the envelope correctly were achieved when using density slightly lower than the bulk and choosing the profile width correspondingly. The transmission results from the following chapter were obtained with slightly narrower slab profile and the resulting density was in fact close to the bulk value. Simulating the transmission in such a way that the resulting density profile is commensurate with the envelope is a subject for further studies.

Chapter 6

Simulating the transmission process with DMC

6.1 Simulating excited states with DMC

Since the DMC method requires interpretation of function f from equation (3.5) as a density function, the method is suitable for problems in which the wave function is positive everywhere. Because of the wave function's arbitrary normalization, this is equivalent to requiring that the wave function does not change its sign anywhere. This is only the case for Bose systems in their ground state. It is significant however that the transmission process occurs while the system as a whole is not in its ground state. The excitation is due only to the kinetic energy of the incoming particle. Proper simulation of the transmission process therefore has to involve a careful selection of the

trial function in order to properly describe this excited state built from the ground state of helium in the film.

Simulating excited bosonic or any fermionic wavefunctions with DMC is possible by taking account of the nodes by methods that are commonly called fixed node DMC (FN DMC) and released node DMC (RN DMC), as described below.

Fixed node diffusion Monte Carlo

Recall that the importance sampling or "guiding" term in the evolution equation (3.6) keeps the walkers from entering the regions where the trial function is vanishing. In particular, given sufficiently small imaginary time steps, walkers may never cross a zero subspace of the guiding wavefunction. On the boundary of such a region the logarithmic derivative of the guiding wavefunction in Eq. (3.6) will necessarily diverge. In the part of configuration space enclosed by a nodal area (which is usually some kind of hypersurface), the wavefunction has a constant sign and obeys the Schrödinger equation. Each nodal region can therefore be simulated as a separate simulation in DMC. In practice, one simulates the entire system simultaneously, prohibiting rare crossing of the nodal surfaces due to the finite time step.

In such a simulation, each system point is assigned a marker according to the sign of Ψ_{T} at the position where the point was originally created. (In case of branching, the sign marker is passed on to the offspring system points.) This marker is carried with the system point and is used to interpret

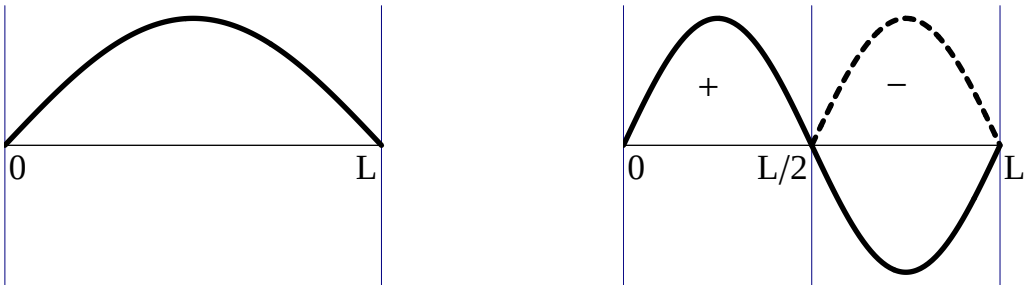

Figure 6.1: Problems with nodes in the wave function may be reduced to several independent problems, one for each nodal region. This is precise only if nodal positions are known exactly.

the contribution of a point to results of the simulation. This approach is illustrated in Fig. 6.1. System points contribute as if the wave function in their location in the configuration space had the sign equal to that of the marker. This is only relevant for some quantities. For example, the expectation value of the energy is computed from the "local energy" of the form (3.8) and does not depend on the sign of the trial wavefunction (however, it will be biased by the fact that the trial function has nodes that do not match exactly the solution to corresponding problem). On the other hand, any kind of one-particle density profile has to make use of the markers. The calculation in which nodes of the guiding function are fixed in this way is called the *fixed node* DMC, or FN DMC [68,69,72,73]. It has been successfully applied to a variety of problems [80, 133–137].

During DMC simulation, the accumulated statistics are essentially an improvement on the initial approximation Ψ_{T}. Since system points cannot cross a region where Ψ_{T} has a node, the resulting simulated wave function will

also have a node at the same position. In other words, while DMC improves on Ψ_{T}, it cannot improve on the nodes of Ψ_{T}.

Released node diffusion Monte Carlo

Correct positioning of nodes is important in order to properly find the energy of the system. Having the nodes fixed is therefore a serious drawback of the method. There are two common approaches to overcome this problem. First, after relaxation with fixed nodes one may move the nodes to satisfy some criteria. This is in a sense optimization of the trial wave function. The second method is the released node DMC simulation [72]. It is usually started once a fixed-node DMC has completely equilibrated. The trial wavefunction is then replaced by a new trial wave function Ψ_{RN} which has constant sign throughout the configuration space. System points are evolved according to Ψ_{RN}, but one keeps track of the number of times σ that a walker crosses the former nodes (of the original trial function Ψ_{T}). Each walker is assigned weight

$$w_i = (-1)^{\sigma_i} \frac{|\Psi_{\mathrm{T}}(\boldsymbol{X}_i)|}{\Psi_{\mathrm{RN}}(\boldsymbol{X}_i)}$$

and the energy is computed as run time average of the released-node expectation

$$E_{\mathrm{RN}} = \frac{\sum w_i E_{\mathrm{L}}(\boldsymbol{X}_i)}{\sum w_i} \tag{6.1}$$

If we denote the original location (at the instance when the nodes were released) of each walker as $\boldsymbol{X}'_i$, then the weight can also be written as

$$w_i = \text{sign}\left(\frac{\Psi_{\text{T}}(\boldsymbol{X}'_i)}{\Psi_{\text{T}}(\boldsymbol{X}_i)}\right)\frac{|\Psi_{\text{T}}(\boldsymbol{X}_i)|}{\Psi_{\text{RN}}(\boldsymbol{X}_i)} = \text{sign}\left(\Psi_{\text{T}}(\boldsymbol{X}'_i)\right)\frac{\Psi_{\text{T}}(\boldsymbol{X}_i)}{\Psi_{\text{RN}}(\boldsymbol{X}_i)}$$

The released-node energy (6.1) approaches the correct energy of the excited (or fermionic etc.) state given by Ψ_{T} and its nodes. However, the error in the expectation value (6.1) is unbound and increases exponentially with the simulation time. The amplitude of this error is determined by the quality of nodes in Ψ_{T}. Successful RN DMC can yield excellent results for both fermionic and bosonic systems [72, 138]. In practice however, one rushes to obtain the relaxed value of energy (which is normally less than the fixed-node value) before the fluctuations resulting from the cancellations from walkers with different signs and the resulting uncertainty in the calculation explodes. (This is a manifestation of so-called *minus sign problem.*) Applicability of the method therefore has to be carefully judged for individual problems.

In our simulations, the nodal surface will be somewhat simple, and it will in fact be exact in certain regions of the simulation volume as it will set the boundary conditions for the simulation. The implication is that we can limit the calculations to a fixed-node DMC with nodal surfaces adjusted in a well controlled way to describe the correct state. This is in flavor similar to methods in which nodes are adjusted within a fixed node simulation, but the underlying motivation and prescription are quite different. Within each such

fixed node simulation, we may eventually attempt the released node method. For the purpose of testing the method and obtaining preliminary transmission results, we remained within the fixed node approach. The method of determining the nodal surface is discussed in detail in the following sections.

6.2 Boundary conditions for the transmission simulation

In this section I will describe our prescription for finding the transmission probabilities for the transmission process with diffusion Monte Carlo. Because the wave function describing the process is nodal, we reformulate the transmission in terms of scattering states for this problem. Each scattering state is described by incident particle's wave vector and a phase shift. Adjusting the phase shifts until the correct one is found for different values of wavevector allows us to calculate various transmission parameters.

Let the elastic transmission involving $N+1$ identical bosons be described by a state $\Psi(\boldsymbol{X}) \equiv \Psi(\boldsymbol{r}_1, \ldots, \boldsymbol{r}_{N+1})$. From the physical nature of the experiment, the energy of this state E_{TR} has to be equal to the sum of the kinetic energy of the particle approaching the slab and the energy of atoms in the ground many-body state of the slab. Then the energy condition can be written exactly as

$$E_{\text{TR}} = \frac{\hbar^2 k^2}{2m} + E_N \tag{6.2}$$

where $\hbar k$ is the momentum of incoming atom and E_N is energy of the remaining N-particles in the slab.

Notice that the ground state energy of all the atoms in a slab with $N+1$ particles E_{N+1} for sufficiently large N is given by

$$E_{N+1} = E_N - |\mu| \tag{6.3}$$

where $\mu = -7.17$ K is chemical potential of particles in helium-II. (We are considering a zero-temperature limit.) Therefore the energy of the transmission state is above the ground state by $\hbar^2 k^2/2m + |\mu|$. (A more exact estimate of E_{N+1} is be obtained by including surface and finite size effects into a separate calculation of this energy.) We are interested in setting the correct boundary conditions describing the transmission process. Such conditions must be consistent with the system being composed of some N particles in a film, and sufficiently far from this film, one and only one particle moving with a defined momentum $\hbar k$. The wavefunction has to properly account for bosonic symmetry of the particles.

Let us denote individual atomic coordinate as $\boldsymbol{r}_i$. We choose a system of coordinates in which z-axis is perpendicular to the slab surface, the transmission direction. We label the remaining *transverse* coordinates as $\boldsymbol{r}^\perp$, so that individual particle's coordinates can be written as $\boldsymbol{r}_i \equiv (\boldsymbol{r}_i^\perp, z_i)$ and the entire set of atomic coordinates comprising a coordinate of a system in the configuration space as $\boldsymbol{X} \equiv (\{\boldsymbol{r}_i\}) \equiv (\{\boldsymbol{r}_i^\perp\}, \{z_i\})$. We employ periodic

boundary conditions with respect to all the transverse directions, so that the wavefunction is periodic with respect to all the transverse components $\boldsymbol{r}_i^{\perp}$. We used the nearest image convention in all the calculations.

In the impact direction $\hat{\boldsymbol{z}}$, we seek to set the remaining boundary conditions as the impact coordinates of atoms tend to infinity. Not more than one atomic coordinates may be allowed to infinity at a time, because the energy of the incoming particle is insufficient to knock out more than one atom from the slab, and therefore the wavefunction must tend to zero for configuration space coordinates with more than one z_i too far from the slab. Similarly, a state in which none of z_i's is allowed to extend infinitely from the slab cannot describe an elastic transmission process. To summarize, we seek non-zero boundary conditions for the many-body wavefunction as

$$z_1, \ldots, z_{N+1} \longrightarrow z_1, \ldots, z_{i-1}, \pm\infty, z_{i+1}, \ldots, z_{N+1}$$

for any i and all $\boldsymbol{r}_i^{\perp}$. We abbreviate this boundary condition as $z_i \to \pm\infty$. The many-body wavefunction $\Psi(\boldsymbol{X})$ at these boundaries will then take the following form:

$$\begin{aligned} &\Psi\left(\boldsymbol{r}_1^{\perp}, \ldots, \boldsymbol{r}_{N+1}^{\perp}, z_1, \ldots, z_{N+1}\right) \xrightarrow{z_i \to \pm\infty} \\ &\qquad \psi_k^{\mathrm{R/L}}(z_i)\Psi_N\left(\boldsymbol{r}_1, \ldots, \boldsymbol{r}_{i-1}, \boldsymbol{r}_{i+1}, \ldots, \boldsymbol{r}_{N+1}\right) \end{aligned} \tag{6.4}$$

Here

$$\psi_k^{\mathrm{R}}(z_i) = T_k \, \mathrm{e}^{\mathrm{i}kz_i}$$

and

$$\psi_k^{\mathrm{L}}(z_i) = \mathrm{e}^{\mathrm{i}kz_i} + R_k \, \mathrm{e}^{-\mathrm{i}kz_i}$$

would properly describe a particle incident onto the slab from the left (negative z-axis direction). These are the similar to the boundary conditions for a one dimensional scattering problem[a], except that the boundary conditions are set on the wavefunction in the complete $3(N+1)$-dimensional space and the final wavefunction is symmetrized over all the $N+1$ particles in the system. These boundary conditions were used in our group by Setty et al. [21,36] in variational Monte Carlo study of the transmission problem as described in section 2.5. However the function ψ_k is complex-valued and therefore unsuitable as a DMC trial function. For our calculations, it is convenient to calculate approximations to the scattering states obeying different boundary conditions and to reconstruct T_k and R_k from the results of simulations with the scattering states. First, we describe the "scattering state" boundary conditions in terms of a one dimensional single particle elastic scattering problem.

[a]Notice that function ψ_k only depends on the impact coordinate z_i. Because only one particle at a time can leave the slab, there is no dependence on transverse component in the r.h.s. of (6.4).

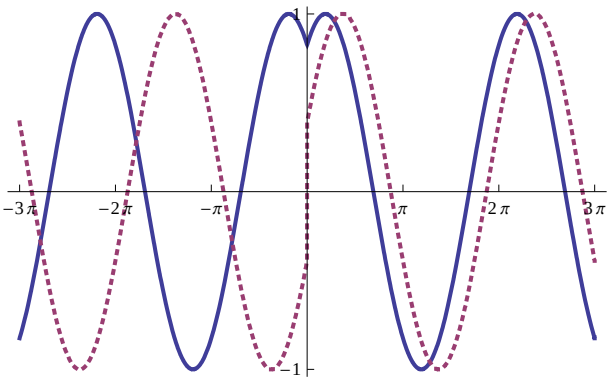

Figure 6.2: Visualization of even and odd single-particle scattering states with phase shifts (correspondingly solid and dashed lines).

Single particle scattering states for normal elastic transmission

In many simple three dimensional scattering problems the symmetry group of the Hamiltonian is the rotation group and the natural choice for scattering states are eigenstates of angular momentum. The boundary conditions are then expressed using combinations of angular momentum eigenstates with different boundary conditions at the origin and with properties at $r \to \infty$ expressed as a phase shift. The phase shifts are then calculated as a function of energy and the cross sections are constructed from them. (A similar procedure was followed by our group in [56].)

In the present problem the symmetry group is the reflection group (elements E, R). The states of even and odd parity with respect to reflection transform like the relevant (and only) irreducible representations. Parity eigenstates replace the angular momentum states in the corresponding 3D problem. In empty space at fixed k, these are simply $\cos(kz)$ and $\sin(kz)$. In

the scattering problem the corresponding phase shifted states are

$$\begin{aligned} \psi_k^+ &= \cos(kz + \delta_e \operatorname{sign} z) = \cos(k|z| + \delta_e) \\ \psi_k^- &= \sin(kz + \delta_o \operatorname{sign} z) = \operatorname{sign}(z) \sin(k|z| + \delta_o) \end{aligned} \tag{6.5}$$

which are easily seen to have even and odd parity and correspond to properly shifted versions of $\cos(kz)$ and $\sin(kz)$ while preserving the parity. These phase-shifted functions have discontinuities at the origin as illustrated in Fig. 6.2. The discontinuities are irrelevant because the functions are in fact only used to establish boundary conditions at $z \to \pm\infty$. This choice of functions was also used by Paulsen and Mølmer [57] to establish boundary conditions in a weak coupling calculation of elastic transmission through a slab of low density bosons via Bogoliubov approximation.

It is straightforward to show that

$$\psi(z) = \mathrm{e}^{\mathrm{i}\delta_e}\, \psi_k^+(z) + \mathrm{i}\, \mathrm{e}^{\mathrm{i}\delta_o}\, \psi_k^-(z)$$

gives the limits

$$\psi_k(x) \to \begin{cases} \mathrm{e}^{\mathrm{i}kx} + R_k\, \mathrm{e}^{-\mathrm{i}kx} & \text{as} \quad z \to -\infty \\ T_k\, \mathrm{e}^{\mathrm{i}kx} & \text{as} \quad z \to +\infty \end{cases} \tag{6.6}$$

with coefficients given by

$$\begin{aligned} R_k &= \tfrac{1}{2}\left(\mathrm{e}^{2\mathrm{i}\delta_e} - \mathrm{e}^{2\mathrm{i}\delta_o}\right) \\ T_k &= \tfrac{1}{2}\left(\mathrm{e}^{2\mathrm{i}\delta_e} + \mathrm{e}^{2\mathrm{i}\delta_o}\right) \end{aligned} \tag{6.7}$$

The above pair of equations is used to determine the transmission coefficient and through it other observables from scattering phases. This result shows that the problem can be mapped between scattering states representation and the usual incident plane wave form. It is also implied that the pair of complex-valued transmission and reflection coefficients can in fact be represented by only two real numbers (the odd and even phase shifts). Lets consider this in a little more detail. The coefficients in the wavefunction (6.6) have to obey the usual condition for the conservation of current: $|R|^2 + |T|^2 = 1$. Consider additionally a superposition of the wavefunction given by (6.6) and a similar one corresponding to particle incident from the right. On the right-hand side of the barrier such a superposition may look like $(T + R^*)\,\mathrm{e}^{\mathrm{i}kx} + \mathrm{e}^{-\mathrm{i}kx}$, and because it describes zero net current, $|T + R^*|^2 = 1$. Combining this with the above equation for the conservation of current, it is straightforward to show that also

$$|T \pm R| = 1$$

That is, the complex coefficients R and T have two constraining equations and the transmission problem has only two degrees of freedom.

For convenience, lets introduce complementary angles Δ and ϕ in the following way:

$$\begin{aligned} \phi &= \delta_e + \delta_o \\ \Delta &= \delta_e - \delta_o \end{aligned}$$

we can then represent relationship (6.7) as

$$\begin{aligned} R_k &= \mathrm{i}\,\mathrm{e}^{\mathrm{i}\phi} \sin\Delta \\ T_k &= \mathrm{e}^{\mathrm{i}\phi} \cos\Delta \end{aligned}$$

Fig. 6.3 illustrates the above expressions and relationships between transmission and reflection coefficients and the phase factors.

Boundary condition for many-body transmission problem in the scattering state form

We use the above results to set the boundary conditions for the many-body problem as well. This is straight-forward in particular because we are considering only elastic and low-energy situation (so that only one particle may be outside of the slab eventually). Because of this, we can demand the boundary condition in the form (6.4) symmetrized over all the particles in the system:

$$\begin{aligned} &\Psi\left(\boldsymbol{r}_1^{\perp}, \ldots, \boldsymbol{r}_{N+1}^{\perp}, z_1, \ldots, z_{N+1}\right) \xrightarrow{z_i \to \pm\infty} \\ &\quad \sum_{i=1}^{N+1} \psi_k^{\pm}(z_i) \Psi_N\left(\boldsymbol{r}_1, \ldots, \boldsymbol{r}_{i-1}, \boldsymbol{r}_{i+1}, \ldots, \boldsymbol{r}_{N+1}\right) \end{aligned} \tag{6.8}$$

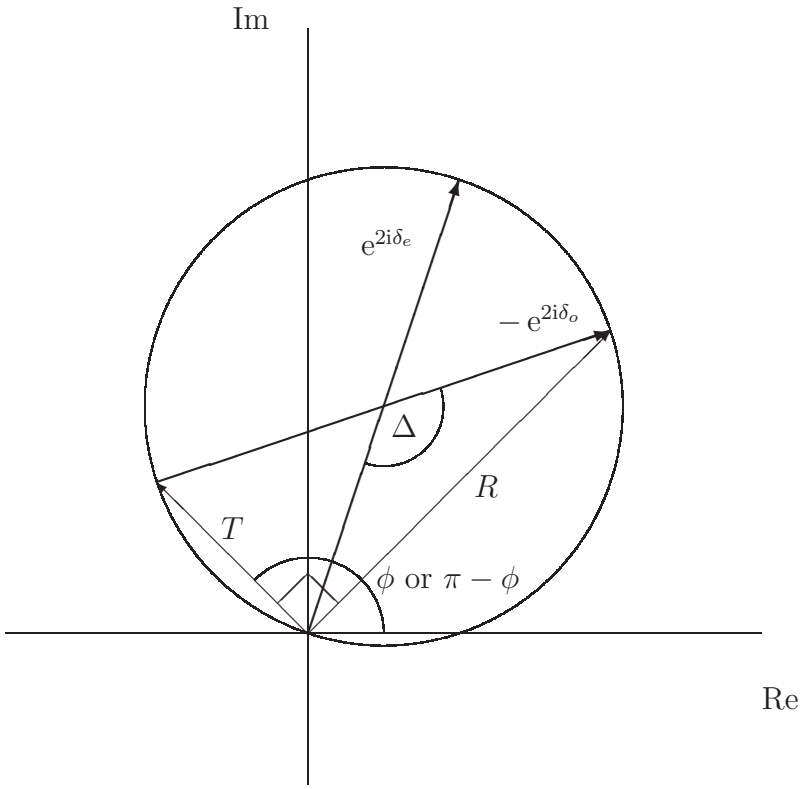

Figure 6.3: Illustration of reflection and transmission coefficients R and T, and their relation to scattering phase factors on the complex plain.

where the functions $\psi^{\pm}$ are the same for each term in the sum and are one of the functions in Eq. (6.5). To find these phase shifts δ_e and δ_o, we make, for given k, a pair of DMC calculations constrained by (6.8) for a set of pairs of values of δ_e and δ_o. We select the correct phases for this wavevector by finding the values of δ_e, δ_o which give the correct energy (6.3).

6.3 Trial function for the transmission simulation

The trial function for our DMC calculation has to incorporate the boundary condition form of Eq. (6.8) and be optimized to describe the slab geometry of the problem. The N-particle terms describing the film in its ground state are constructed in the same way as the film trial wavefunction described in chapter 5. They consist of Jastrow pair-product terms excluding the helium atom hard cores from overlapping, and of a product of one-particle film profiles guiding the atoms towards the bulk of the film. Profiles are calculated with respect to the center of mass of the entire system.

Jastrow pair products ought to be added between the incident particle at each term of the sum and the particles remaining in the film. This term simplifies with the pair products for particles in the film and forms an $(N+1)$-particle Bijl-Jastrow type wavefunction that can be factored out of the sum in Eq. (6.8).

The impact particle in each term in Eq. (6.8) is prohibited from attempting to penetrate too deep into the slab directly by a term which goes to zero inside the slab.

All of these terms follow the trial function used in variational calculations

in [21,36]. Putting them together, the trial function takes the following form

$$\Psi_{\mathrm{T}}\left(\boldsymbol{r}_1,\ldots,\boldsymbol{r}_{N+1}\right) = \sum_{i=1}^{N+1}\psi_k^{\pm}(z_i)\left(1-f(z_i^*)\right)\prod_{j\neq i}f(z_j^*)\Psi_{\mathrm{J}}^{N+1}\left(\boldsymbol{r}_1,\ldots,\boldsymbol{r}_{N+1}\right) \tag{6.9}$$

where

$$z_i^* = z_i - \frac{\sum_s z_s}{N+1}$$

and function f is given by Eq. (5.2), $\psi^{\pm}$ are given correspondingly by even and odd functions from Eq. (6.5), and Jastrow wavefunction Ψ_J is defined in Eqs. (4.5–4.7).

In the variational calculations described in section 2.5, a boost term was used to describe the motion of the center of mass during the intermediate process:

$$\Psi_{\mathrm{B}} = \Psi_{\mathrm{J}}(\boldsymbol{r}_1 - \boldsymbol{r}_{\mathrm{c.m.}},\cdots,\boldsymbol{r}_{N+1} - \boldsymbol{r}_{\mathrm{c.m.}})\exp\left[\mathrm{i}k' z_{\mathrm{c.m.}}\right]$$

Wavevector k' was a variational parameter ensuing that the boost term carries sufficient amount of momentum to satisfy current conservation throughout the volume. The term itself was mixed with the rest of the wavefunction with a variational parameter.

It is in our plans to observe how the addition of a boost term of this form affects the outcome of our simulations. The boost term allowed for momentum conservation in the variational calculations and significantly improved optimization. However the scattering states that we are using do not

carry momentum on their own. For this reason, a DMC calculation may in principle be able to find the state which is a standing wave representation corresponding to momentum being carried by the bulk of the film. Our preliminary results indeed turned out similar to the variational ones although the trial function did not include any boost-like terms.

6.4 Transmission time analysis

Phase information extracted from the transmission calculations can be used to obtain the transmission times. Consider a wavepacket describing a free particle propagating toward the detector after leaving the surface of the film. It is described by

$$\psi(\boldsymbol{r},t) = \int \frac{d^3k}{(2\pi)^3}\, g(\boldsymbol{k}) \exp\left[\mathrm{i}\left(\boldsymbol{k}\cdot\boldsymbol{r} - E(\boldsymbol{k})t/\hbar + \phi(\boldsymbol{k})\right)\right]$$

where $g(\boldsymbol{k})$ is a function that is non-zero in narrow region around the particle wavevector $\boldsymbol{k}_0$. Provided $g(\boldsymbol{k})$ is sufficiently narrow so that the particle has a well-defined momentum, we can follow the stationary phase argument. Wherever the phase factor in the integrand is oscillatory the integral will be vanishing. The condition for the location of the wavepacket's maximum in coordinate space is therefore an extremum in the integrand's phase with respect to $\boldsymbol{k}$. Considering the motion along a single impact axis z and substituting $E = \hbar^2k^2/2m$, the condition becomes

$$\frac{\partial}{\partial k}\left(kz - \frac{\hbar k^2 t}{2m} + \phi(k)\right)\bigg|_{k_0} = 0$$

The atom will reach the detector at some distance L_{det} from the surface in time

$$t = \frac{L_{\mathrm{det}} + \frac{d\phi}{dk}}{\frac{\hbar k}{m}} = \frac{L_{\mathrm{det}} + \frac{d\phi}{dk}}{v_k}$$

where we labeled the free particle's speed as v_k. In case of transmission the phase is determined by the transmission coefficient $T_k = |T_k| \, \mathrm{e}^{\mathrm{i}\phi(k)}$ because the wavepacket has the form in which $g(k) \to g(k) \, |T_k| \exp(\mathrm{i}\phi(k))$. A freely moving particle will not have an additional phase dependence and therefore the delay in time between the transmitted particle compared to one which moved without helium slab in place is

$$t_{\mathrm{slab}} - t_{\mathrm{noslab}} = \frac{1}{v_k} \frac{d\phi}{dk}$$

or

$$t_{\mathrm{slab}} = \frac{L + \dfrac{d\phi}{dk}}{v_k}$$
$$t_{\mathrm{slab}} \frac{v_k}{L} = 1 + \frac{1}{L} \frac{d\phi}{dk}$$

where L denotes width of the slab. We can also rewrite this as an expression for phase:

$$\frac{d\phi}{dk} = L \left(\frac{t_{\mathrm{slab}}}{t_{\mathrm{noslab}}} - 1 \right) \tag{6.10}$$

Condensate mediated transmission

In the case of condensate mediated transmission, we expect $t_{\mathrm{slab}} \ll L/v_k$ and therefore Eq. (6.10) integrates to a simple linear dependence:

$$\phi = \phi_{_0} - L(k - k_{_0}) \tag{6.11}$$

Quasiparticle mediated transmission

In the case of quasiparticle mediated transmission, the transmission time is the time that it takes for the corresponding quasiparticle to traverse the slab. This time is determined by quasiparticle group velocity $v_g = \frac{\partial \omega_q}{\partial q} = \frac{1}{\hbar}\frac{\partial \epsilon_q}{\partial q}$. Group velocities for the helium excitation spectrum are shown in Fig. 6.4. Transmission with rotons having negative group velocity is unlikely [30, 31] and maxons[b] have such a large energy that one would expect ejection of multiple particles and decay of maxons into other quasiparticles to be competing mechanisms with large amplitudes [32]. We are therefore interested in the branches corresponding to phonons and rotons with positive group velocity.

With the transmission times given by $t_{\text{slab}} = L/v_g$, Eq. (6.10) integrates to

$$\phi = \phi_0 + L\left[-(k-k_0) + \int_{k_0}^{k} \frac{\frac{\hbar k}{m}}{\left(\frac{\partial \omega_q}{\partial q}\right)}\, dk\right]$$

The energy is conserved in quantum condensation and the momentum of the quasiparticle can be therefore determined from the incoming atom's momentum: $\frac{\hbar^2}{2m}k^2 = \mu + \epsilon(q)$. In certain range on energies, several branches of the excitation spectrum will satisfy the energy conservation. The phase contribution should be summed over all possible branches, with corresponding (unknown) amplitudes. However, on each of the branches the integral

[b] Quasiparticles that correspond to the local maximum in $\epsilon(k)$ near $k = 1.1\text{Å}^{-1}$ are called maxons.

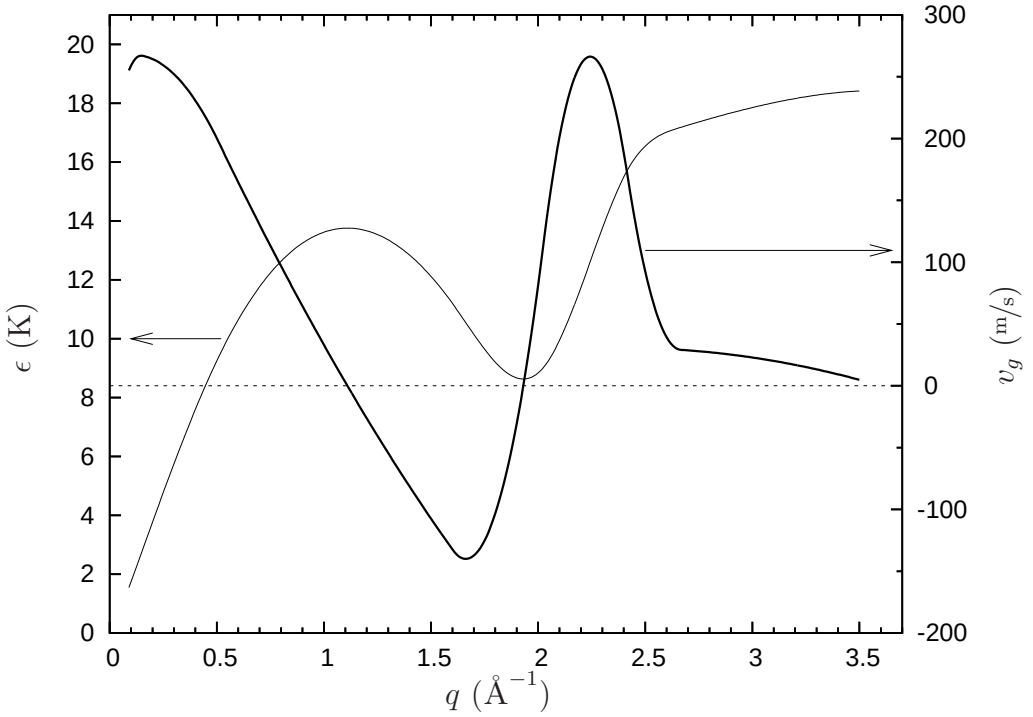

Figure 6.4: Helium-II excitation spectrum (thin line, left axis) and quasiparticle group velocity (thick line, right axis). Built with spline coefficients from [34].

simplifies to a trivial one:

$$\int_{k_0}^{k} \frac{\frac{\hbar k}{m}}{\left(\frac{\partial \omega_q}{\partial q}\right)} dk = \int_{q(k_0)}^{q(k)} dq \left(\frac{\partial k}{\partial q}\right)\left(\frac{\hbar k}{m}\right)\left(\frac{\hbar\, \partial q}{\partial \epsilon}\right) = \int_{q(k_0)}^{q(k)} dq = q - q_0$$

Therefore a phase of the transmission coefficient in case of quasiparticle-mediated transmission by a single branch is given by

$$\phi - \phi_0 = L\left[-(k - k_0) + (q_k - q_{k_0})\right] \tag{6.12}$$

A plot of ϕ/L is shown in Fig. 6.5. It is our intention to attempt to in-

fer the mechanism of transmission from the k-dependence of the phase of the transmission coefficient calculated with DMC. The difficulties in this approach are that there are arbitrary constants defining the phases (separately for condensate-mediated and quasiparticle-mediated transmission), and that the width of the slab is not well defined due to the finite width of the surface layer. The quasiparticle may be excited or destroyed at some small depth into the film and the process may carry additional time delays. However, we expect the general character of the dependence of $\phi(k)$ to hold nonetheless.

The above discussion assumes a single transmission channel. In practice we should expect interference between different transmission channels. This includes interference between quasiparticle mediated transmission with quasiparticles from different branches of the excitation spectrum (possible modes are determined by the fixed energy of the incoming atoms). Even presuming there's no interference between the processes carrying the transmission inside the slab, the resulting phases will still interfere on exit. Lets assume just two transmission channels, with resulting transmission amplitude in the form $T_1(k)\,\mathrm{e}^{\mathrm{i}\phi_1(k)}$ and $T_2(k)\,\mathrm{e}^{\mathrm{i}\phi_2(k)}$, where all the parameters are real. We can present the resulting interference pattern as a transmission with a single phase: $T_1\,\mathrm{e}^{\mathrm{i}\phi_2} + T_1\,\mathrm{e}^{\mathrm{i}\phi_2} = T\,\mathrm{e}^{\mathrm{i}\phi}$ where T and ϕ can be found by considering equality for real and imaginary parts of this equation. In particular, for the phase we can write

$$\phi = \tan^{-1}\frac{\sin\alpha\sin\phi_1 + \cos\alpha\sin\phi_2}{\sin\alpha\cos\phi_1 + \cos\alpha\cos\phi_2} \tag{6.13}$$

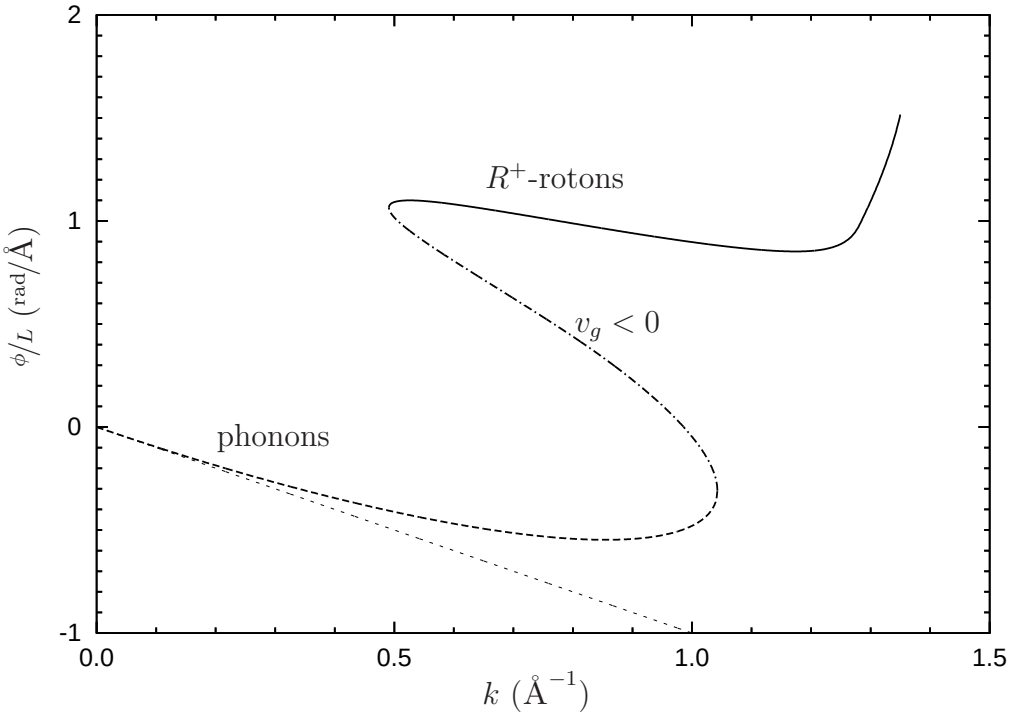

Figure 6.5: Expected dependence of the phase of transmission coefficient in case of quasiparticle-mediated transmission via a single branch, scaled to width L of the slab. Horizontal axis is incoming atom's wavevector. Straight dotted line corresponds to condensate-mediated phase result $(\phi - \phi_0)/L = (k - k_0)$. All phases are defined to within a constant. Built with spline coefficients from Ref. [34].

where we introduced an auxiliary phase $\alpha(k)$ such that $\sin\alpha = \frac{T_1}{\sqrt{T_1^2+T_2^2}}$ and $\cos\alpha = \frac{T_2}{\sqrt{T_1^2+T_2^2}}$. In case we happened to observe a rich behavior in the transmission phase, we would perform fitting and analysis in line of Eq. (6.13), perhaps considering up to four channels for some energies. At this point however, we only observe phases that lie distinctly on a single branch and such interference analysis is not warranted.

6.5 Results for 32-particle simulations

In this section we present results of 32-particle transmission simulations. Boundary conditions, confining to a film and the pair correlations were described by trial function function (6.9) with Ψ_J given by Eqs. (4.5–4.7). Box transverse dimensions were 6.15×6.15Å and film parameter were set at $a = 19.7$Å (half-thickness) and $b = 0.49$Å (corresponding to 10–90% surface layer width of 1.8Å). We used the imaginary timestep of $10^{-4}\mathrm{K}^{-1}$ in half million steps resulting in total projection time of $50\mathrm{K}^{-1}$. Each simulation involved an average of 500 system points, but no more than 1000. We utilized an algorithm with second-order convergence in time step as proposed by S. Chin [86]. This algorithm was classified as DMC 2a in [86] and has since been tested with helium-II [77] and on systems with nodal wavefunctions [85]. The system was allowed to equilibrate from initial conditions for the first one-fifth of the run. Equilibration was monitored by following the energy and density histograms and was found to be well within the allotted period.

Using a small number of particles allowed for a fast turn-around time[c] and made development feasible. The results suffered from finite size effects Because we used only the nearest-neighbor image convention, a significant portion of the Lennard-Jones potential at large particle separations was not

[c]Each energy-value point presented in the graphs in this section would take one and a half days of single-core time on a modern PC. Total wall time for 32-particle simulation results presented in figures 6.22 and 6.23 is almost two years.

accessible for atoms separated only in the transverse direction. Similarly, the simple but short-ranged nature of two-particle correlation function that we used (Eq. 4.6) for the trial function was better suited for such system size. Nonetheless, part of this correlation function was also not accessible for particles in the same normal plane.

Finding the correct intercept energy

The energy that corresponds to the correct phase as described in section 6.2 is given by Eq. (6.2). It contains the readily computed kinetic energy and the energy of a film containing N particles (while the entire system contains $N + 1$ particles). In the case of 32-particle transmission, this calls for simulating 31-particle films. However, the number of particles was chosen to be 32 to allow for better filling of the simulation volume. While helium at zero temperature and s.v.p. does not form a solid, it is closely packed with a structure resembling fcc at short range. The tight packing is manifested by the sharpness of the characteristic first peak in its radial distribution function. Simply removing one atom and performing a film simulation with such a system may therefore have a bias in energy value because of suboptimal filling of the simulation volume. We regard this as a form of finite size effect. If it was absent, we would expect to observe an energy dependence linear in number of atoms (the surface area remains constant and equal to double the cross section of the simulation box — so long as it is well filled): $E_N = \sigma M + \mu(N - M)$ with a fixed surface tension σ and a fixed number

of atoms on the surface M. In practice we observed various features in the energy dependence of films on the number of particles, including the filling effects. For this particular setup in the neighborhood of 32 particles, energy is linear to within errors (see Table 6.1). However using data for 32 and 33 particles to extract the chemical potential and then extrapolating for 31 particles yields an energy almost a degree lower than the 31-particle simulation itself. Our conclusion is that we are dealing with systematic errors due to filling effects of just under 1K, compared to a typical statistical errors of half a degree.

Table 6.1: Energy for film simulation with different number of particles.

E (K)	N_{total}	$E - E_{32}$
-143.72 ± 0.42	31	6.42 ± 0.75
-150.14 ± 0.37	32	—
-155.98 ± 0.30	33	5.84 ± 0.48

The number of system points in these simulations was not sufficient for us to claim a full relaxation. This was manifested by the fact that relaxation to lower energies could be achieved when the number of system points was tripled. Therefore, simulations with larger number of system points are desirable but have not yet been performed. Additional tests with a larger number of system points resulted in energy vs. phase dependence with lower

overall energies but the same peak location. For this reason, we believe that the smaller scale calculation presented in this section are still useful. During some of the simulations we observe very large error bars or obtain energy values far from the apparent trend. These simulations were slow or impossible to equilibrate, usually with one atom expelled to the outside node far from the film. This is apparent in Figure 6.21 located on p. 124 where simulations of odd state at phases -0.65π and -0.85π are stuck at the same energy as the intercept, apparently with one atom expelled to a nodal region outside the film from which it could not find a path back to the film. Using a larger ensemble helps to avoid such "accidents". Energy in the transmission simulations never exceeded the correct phase result dictated by equation (6.2). This is to be expected as any state with energy higher than that for a film and a particle outside could relax by expelling one atom to a region remote from the film. In other words, we should always expect a lesser-or-equal inequality in Eq. (6.2).

As a result of the systematic bias due to the insufficient number of system points and bias in computing the film energy alone due to filling effects, energy scattering states with different phases fell slightly short of the expected sum of the free particle+film energies. For these reasons, for each scan of energy vs. phase shift at a fixed k (and choice of odd or even parity), we found the correct intercept phase by looking at the highest energy, even if it was about a degree short of the condition (6.2). Sample scan results for different wavevectors are presented in the following pages.

Quality and contrast of the intercept varied with the wavevector. Often adding a few more simulations helped to understand data points which correspond to poorly equilibrated runs, especially those with atoms expelled to far from the slab. An example of this is given in Fig. 6.7 on p. 117. At first the data point at $\delta_o = -0.4\pi$ appeared at large energy. However subsequent runs showed that the correct value of energy in much lower at that phase, and the correct phase value for this wavevector is at $\delta_o = -0.1\pi$. There is a similar example is for even scan (Fig. 6.8) on p. 118.‘ For some choices of k, multiple repeated runs were necessary to determine a range for the phase, as in data in Fig. 6.11 on p. 119. Finally, some of the scans were hard to resolve even with multiple repeated calculations as in Fig. 6.14 on p. 121. However, in each of these cases we were able to pinpoint the correct phase, with a combination of repeated simulations where necessary and understanding that we often get the locked states. (We are currently working on improving this aspect of the calculations.)

Occasionally, a scan appears with an apparent double structure. This is demonstrated in Fig. 6.17 on p. 122, which is in fact exceptional as normally one of the apparent peaks is at least slightly but distinctly higher in energy. Another example of this is in Fig. 6.19 on p. 123, which will be discussed later.

Where the intercept was hard to locate, we assigned a larger admissible range for the phase, resulting in larger range for the transmission coefficient and its phase.

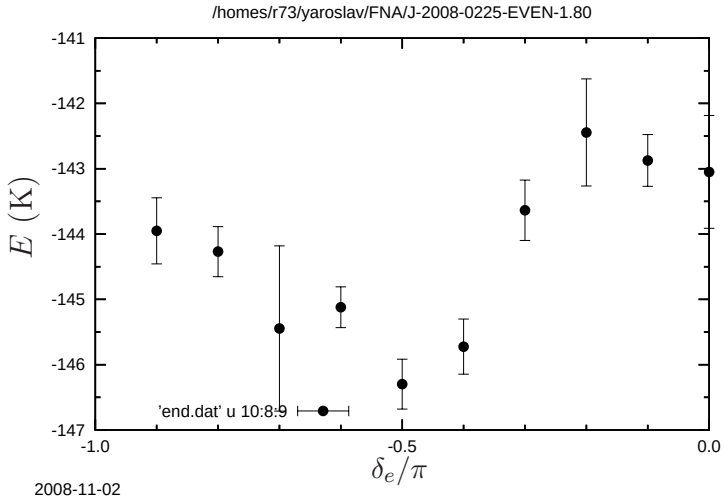

Figure 6.6: Energy vs. phase for even simulation using $k = 0.71\text{Å}^{-1}$.

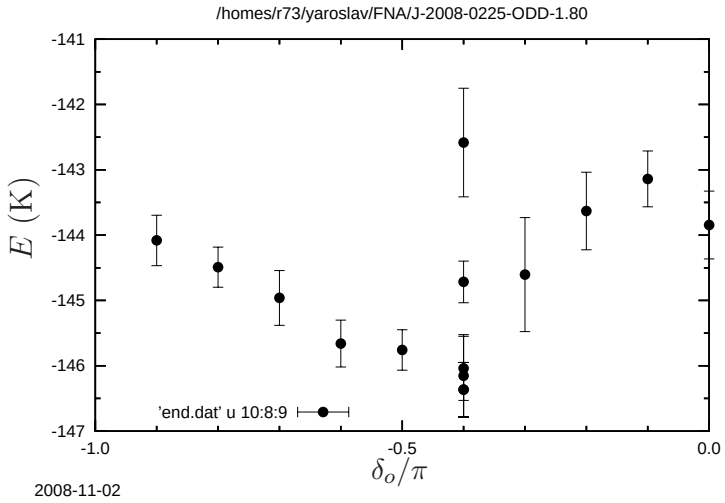

Figure 6.7: Energy vs. phase for odd simulation using $k = 0.71\text{Å}^{-1}$.

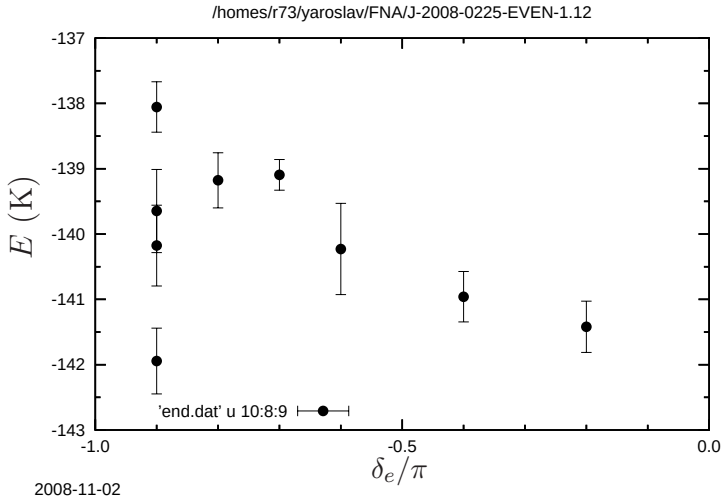

Figure 6.8: Energy vs. phase for even simulation using $k = 1.14\text{Å}^{-1}$.

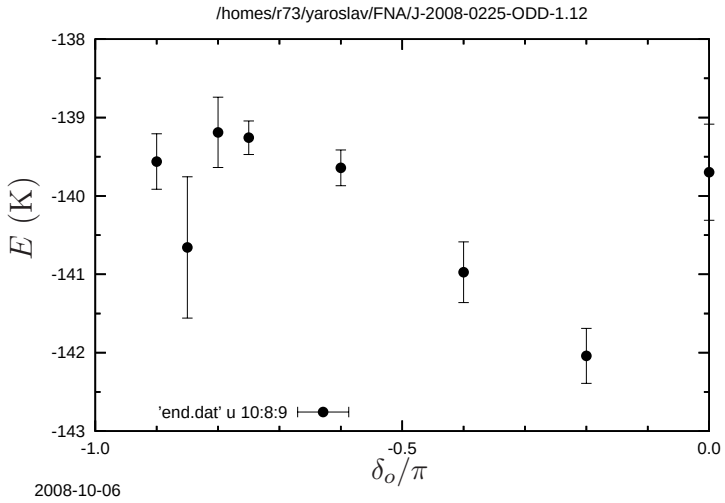

Figure 6.9: Energy vs. phase for odd simulation using $k = 1.14\text{Å}^{-1}$.

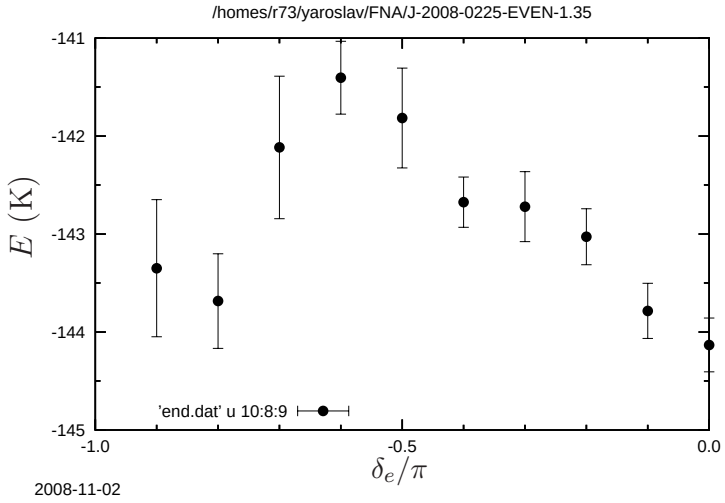

Figure 6.10: Energy vs. phase for even simulation using $k = 0.97\text{Å}^{-1}$.

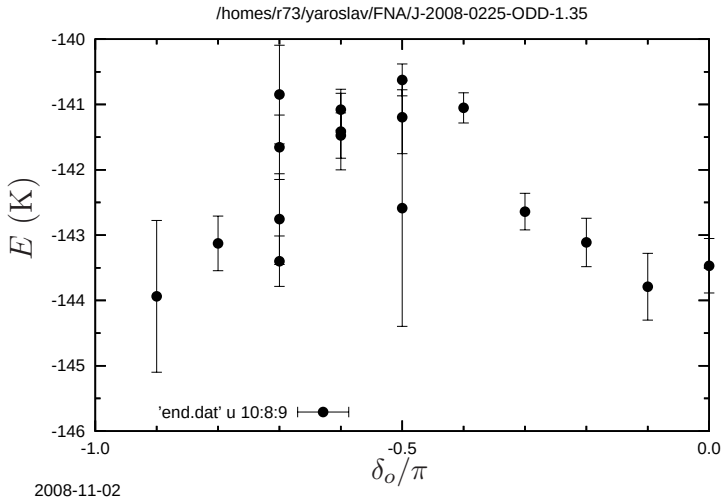

Figure 6.11: Energy vs. phase for odd simulation using $k = 0.97\text{Å}^{-1}$.

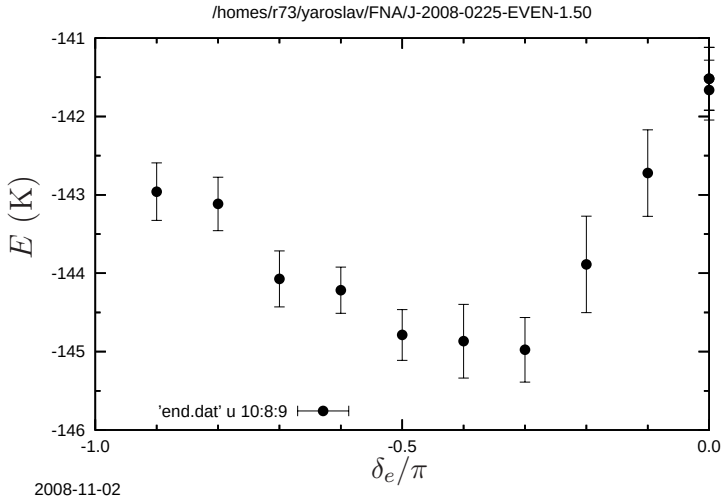

Figure 6.12: Energy vs. phase for even simulation using $k = 0.85\text{Å}^{-1}$.

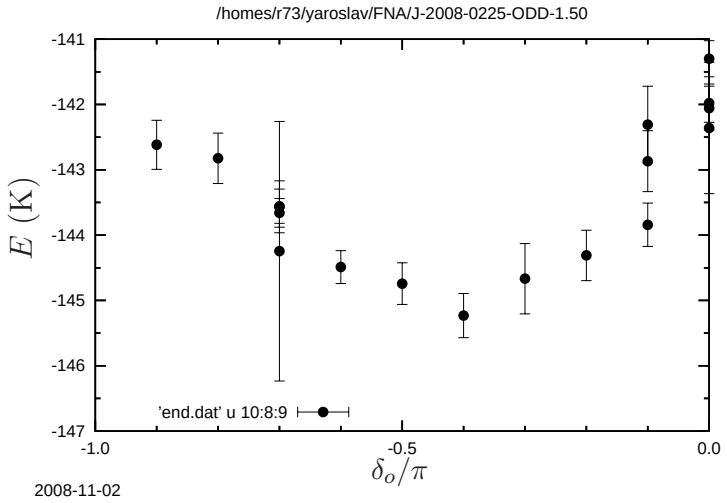

Figure 6.13: Energy vs. phase for odd simulation using $k = 0.85\text{Å}^{-1}$.

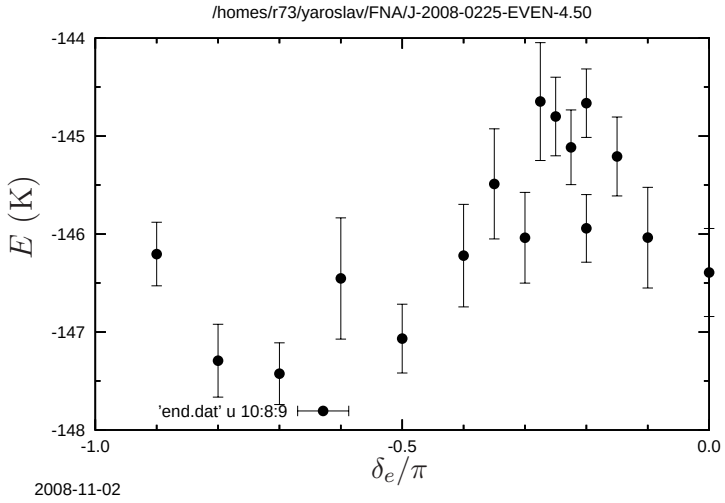

Figure 6.14: Energy vs. phase for even simulation using $k = 0.28\text{Å}^{-1}$.

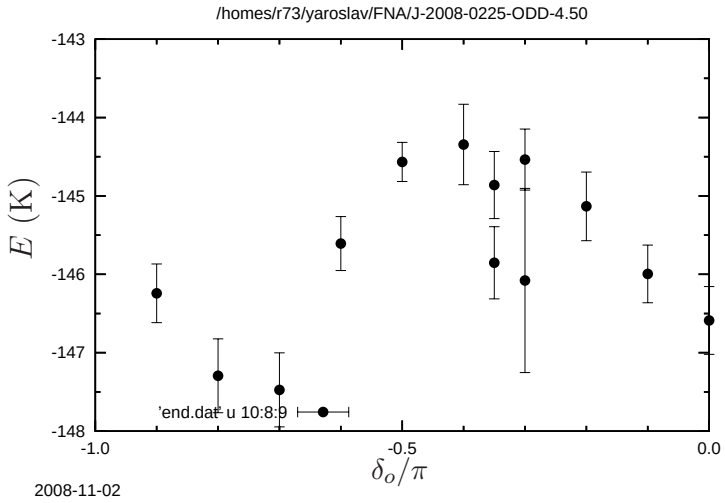

Figure 6.15: Energy vs. phase for odd simulation using $k = 0.28\text{Å}^{-1}$.

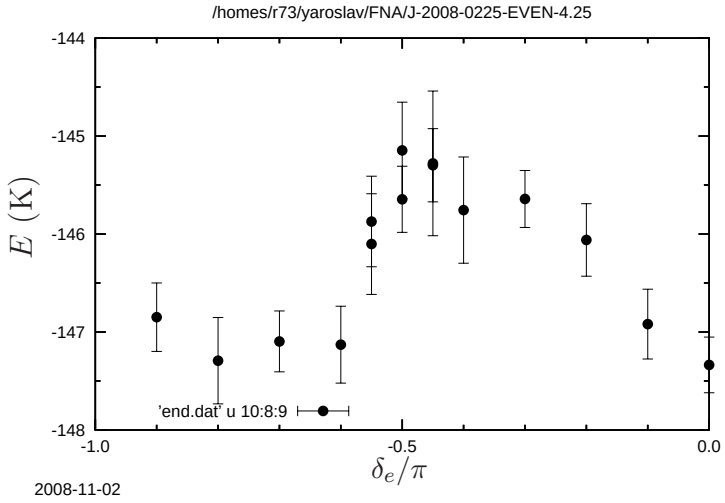

Figure 6.16: Energy vs. phase for even simulation using $k = 0.30\text{Å}^{-1}$.

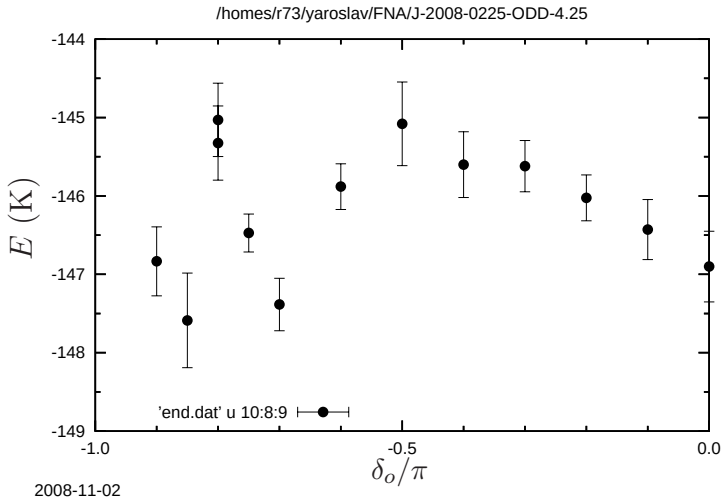

Figure 6.17: Energy vs. phase for odd simulation using $k = 0.30\text{Å}^{-1}$.

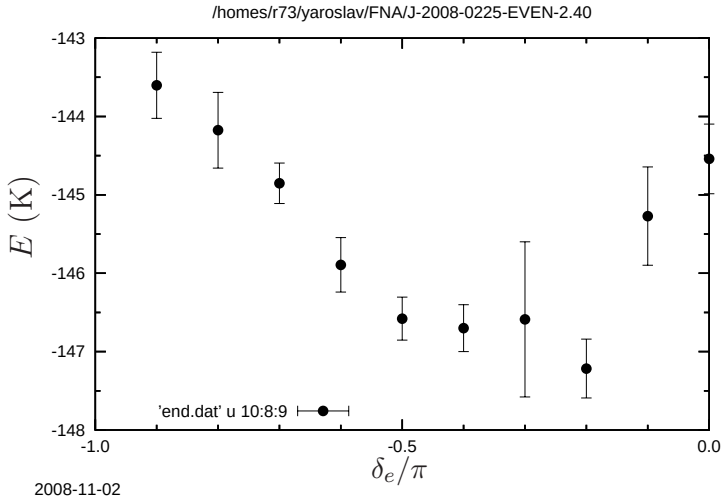

Figure 6.18: Energy vs. phase for even simulation using $k = 0.53\text{Å}^{-1}$.

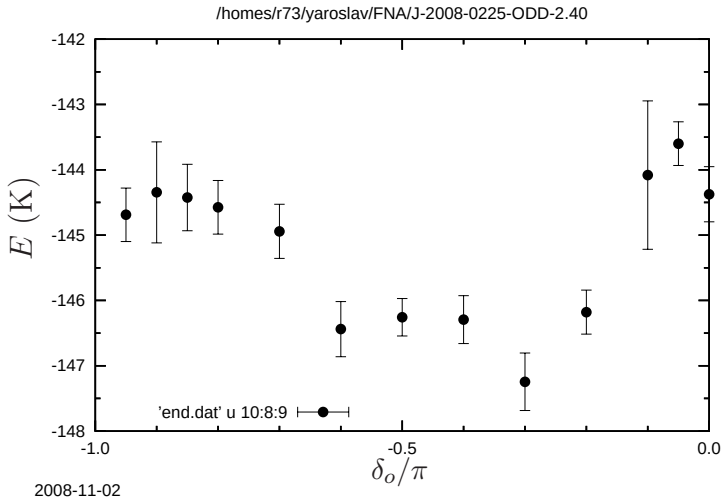

Figure 6.19: Energy vs. phase for odd simulation using $k = 0.53\text{Å}^{-1}$.

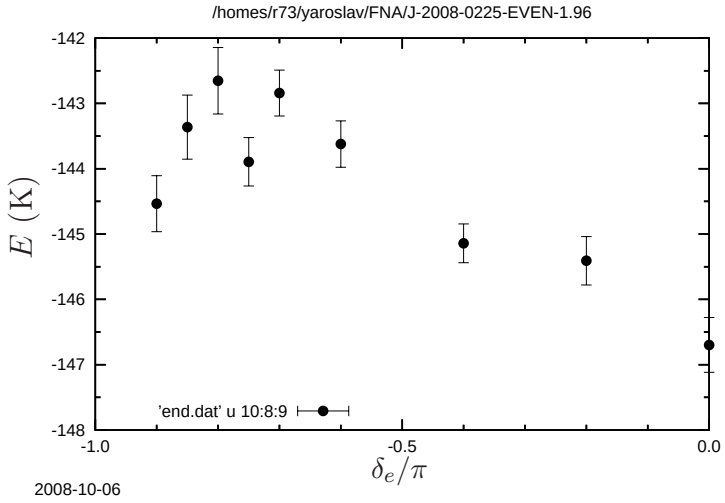

Figure 6.20: Energy vs. phase for even simulation using $k = 0.65\text{Å}^{-1}$.

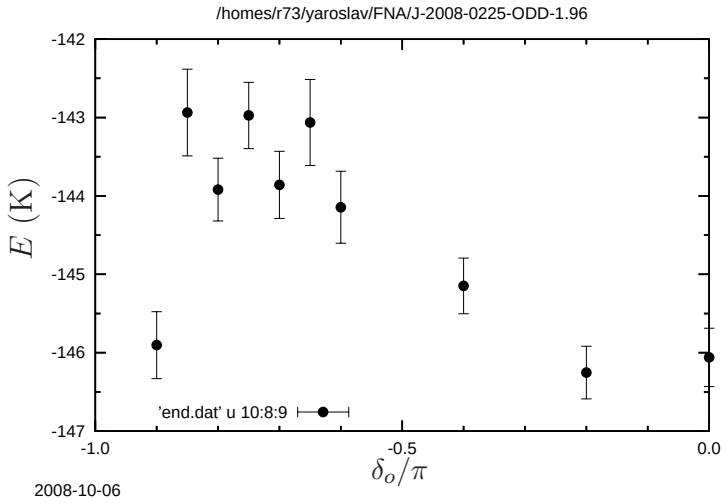

Figure 6.21: Energy vs. phase for odd simulation using $k = 0.65\text{Å}^{-1}$.

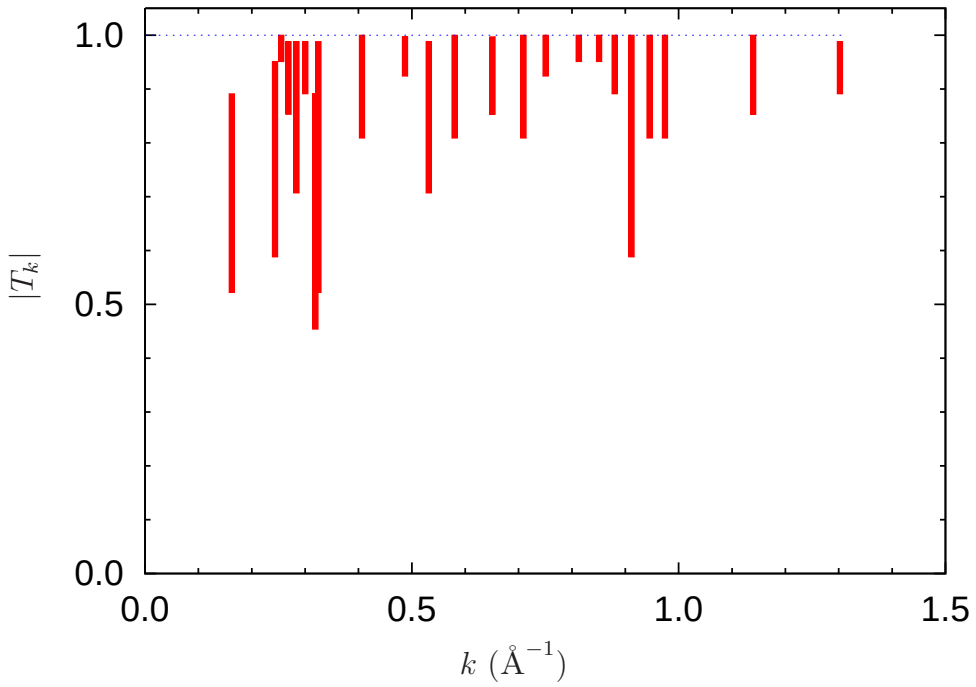

Figure 6.22: Absolute value of the transmission coefficient.

Phase intercept results and discussion

Phases were extracted from each calculation as described above and a range of admissible ranges for transmission coefficients were calculated with the help of Eq. (6.7).

Transmission coefficient turned out to be close to unity and allowed complete transparency at most of the wavevectors. There is some structure and diminution of the calculated $|T_k|$ at low wavevectors. This may be an artifact of the fact that the wavelength of the incoming particle becomes commensurate with the size of the slab at these k's.

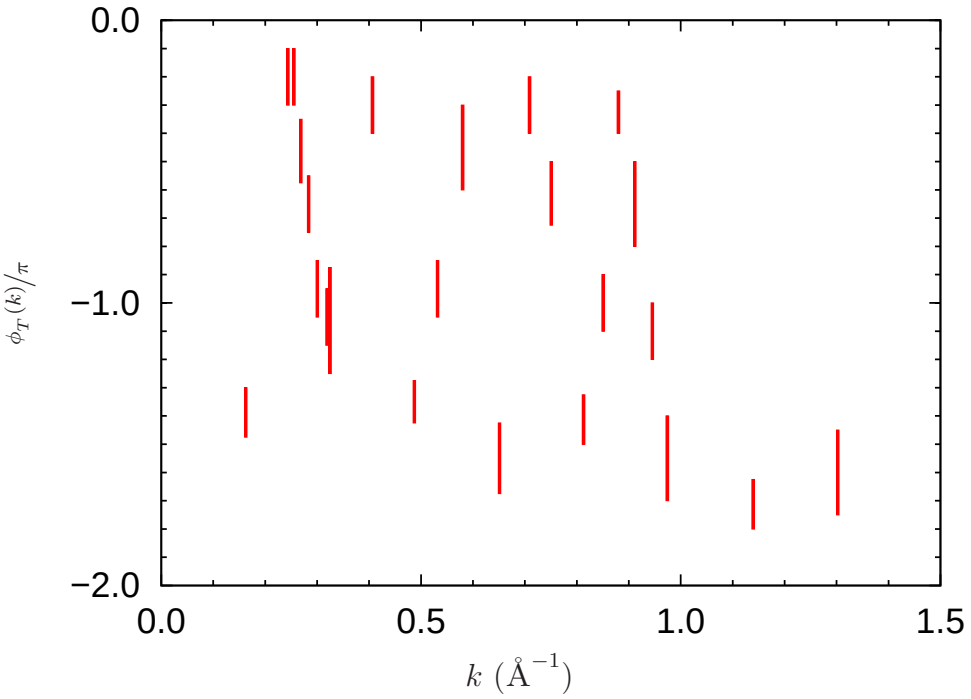

Figure 6.23: Phase of the transmission coefficient, shifted to fit between zero and -2π.

The phase of the transmission coefficient can be used to extract transmission times and to possibly infer the transmission mechanism from this information, as described in Section 6.4. Raw results are shown in Fig. 6.23. Phases for the scattering states are meaningful to within an addition of a factor of π and phase of the transmission coefficient is meaningful to within an addition of 2π (T is a measurable quantity; also recall Eq. (6.7)). Phase results in Fig. 6.23 are shifted so that they lie in $(0, -2\pi]$. A stripe pattern is observed. We shifted the phases by factors of 2π to allow for smooth continuation of these stripes. When this is done, data begins to collapse onto

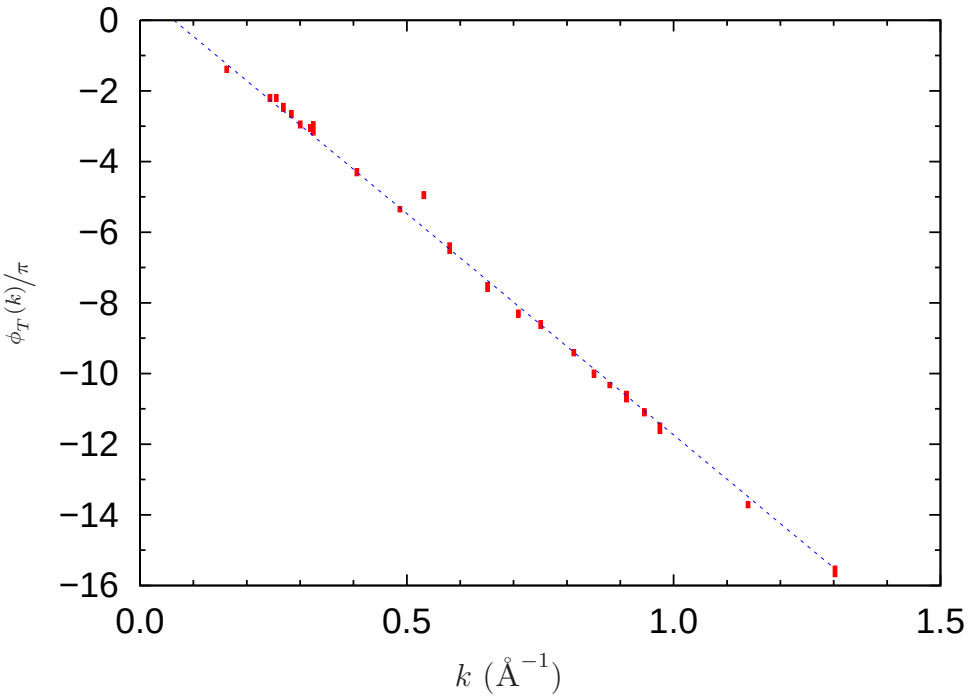

Figure 6.24: Phase of the transmission coefficient. Individual values are shifted by multiples of 2π to form a continuous phase dependence. Data points without neighbors were shifted similarly if they collapsed on the line with the rest of the data. The straight dashed line is phase in case of condensate mediated transmission according to Eq. (6.11). The only free parameter is the offset of this line which was gauged by eye.

a single straight line. Even those few points that are far separated from the rest can be shifted by a factor of 2π and collapse onto this line convincingly. (Results for $k = 0.53$ Å^{-1}, which did not collapse onto such a line are discussed below.) Figure 6.23 shows a line passing through the points. This line was produced with Eq. (6.11) for the phase in case of rapid transmission such as is the condensate mediated transmission. The slope of the line is determined by the width of the slab as set by the envelope function. The only

free parameter for this line is the phase offset which was eyeballed to allow for the line to pass through largest number of data markers. The excellent fit to our phase results suggests that the transmission indeed occurs in this model with condensate mediated transmission as the leading mechanism.

The only data point that falls out of the general trend is the calculation at $k = 0.532$ Å^{-1}. The transmission probability turned out much smaller at this wavevector, and the phase of the transmission amplitude did not collapse onto the trend for the rest of the data or the model corresponding to condensate mediated transmission. Scans of energy for different phases of the scattering states for this k-vector are shown in Figs. 6.18 and 6.19 on p. 123. Notice the double peak structure for the odd state's energy dependence (Fig. 6.19). The peak on the right is located higher and was chosen as the correct phase for this odd state. If the peak on the left were selected instead, the resulting transmission coefficient and its phase would fall within the general trend that we observed in this calculation. In particular, the transmission probability would be much higher and the phase of the transmission coefficient would fit well with the condensate mediated model shown in Fig. 6.24. However, there is no reason to discard the original result for the scattering phase. We found it interesting that it occurred at wavevectors very close to the possible onset of roton mediated transmission. Quite surprisingly, this point fitted on the roton branch of the transmission phase when this branch was aligned to match the condensate mediated model at its origin. This is illustrated in Fig. 6.25. There was no other fitting done with this branch (width of

the slab is taken from the slab profile function's parameters). While such a single datapoint match is at best inconclusive, we find that this occurrence warrants further investigation. We are performing additional calculation in this region of k-vectors at this time.

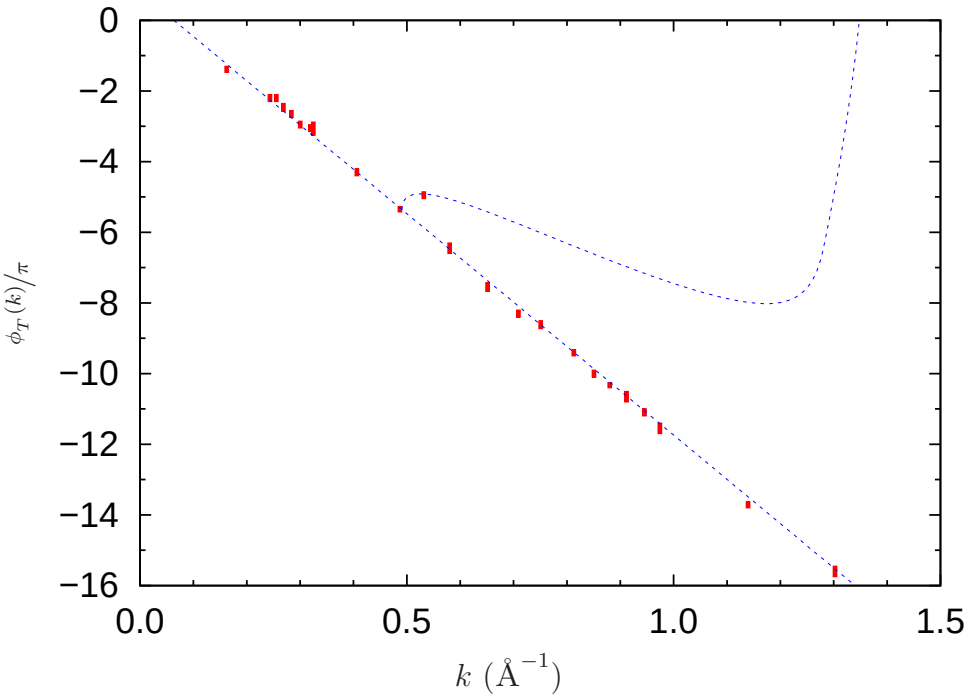

Figure 6.25: Phase of the transmission coefficient. Data is the same as in Fig. 6.24. Individual values are shifted by multiples of 2π to form a continuous phase dependence. Data points without many neighbor points were shifted similarly if they collapsed on the line with the rest of the data. The straight dashed line is phase in case of condensate mediated transmission according to Eq. (6.11). The only free parameter is the offset of this line which was gauged by eye. The curved line is the roton branch of quasiparticle mediated phase delay as shown on Fig. 6.5. The only free parameter was the vertical phase offset which was chosen to touch the straight line of the condensate mediation phase model.

Chapter 7

Summary

The elastic transmission of atoms through superfluid helium is an interesting experimental result which owes its existence to the properties of helium-II. As the experimental techniques develop, we expect to eventually see more controlled transmission conditions and better detection resolution. Our calculations suggests that the results of such experiments would provide an insight into the structure of superfluid, including the condensation phenomenon.

We have developed a modification of diffusion Monte Carlo method which is capable of characterizing some of the aspects of the transmission process. Unparalleled in its ability to tackle bosonic ground state problems, including correlated many-body systems, diffusion Monte Carlo is not directly suitable for simulating excited states phenomena. It is rarely applied to kinetic processes. Our variation of the method allows to characterize the kinetic process of atomic transmission. While the method is limited to elastic processes and

still somewhat lacks in terms of precision, we were able to extract results for transmission through a small unbound cluster of helium. Though it is small, such a system is significantly many-body in terms of theoretical complexity. The success of these calculations makes us optimistic regarding our ability to address the problem in more detail.

Results of our calculations show a significant likelihood of the condensate mediated transmission. This is an exciting result as the hypothesis is yet to be unambiguously tested in an experiment. We believe that these results may inspire and direct a greater experimental effort into characterizing or ruling out this hypothesis.

From the point of view of quality of present calculations, there is an improvement over past efforts. We improved on variational calculations of a past group member and obtained similar results regarding the possibility of the condensate-mediated transmission. We were able to study a much larger range of energies in the probe beam than the past study. While we also observe transmission behavior characteristic of the condensate mediated transmission, our transmission probability values are much higher. Results obtained with our DMC modification are also undoubtedly much less dependent on our model wavefunction and in this sense are more reliable.

There remains a large amount of work to be performed for improving the calculations technically but also in testing several important modifications of the transmission model. Such work could provide further insight into the nature of the transmission which we observe in our calculations and

provide additional clues for our predictions regarding various transmission mechanisms.

Bibliography

[1] J. Wilks and D. S. Betts. *An introduction to liquid helium* (Oxford University Press, New York, 1987).

[2] F. London. The λ-phenomenon of liquid helium and the Bose-Einstein degeneracy. Nature **141**, 643 (1938).

[3] F. London. On the Bose-Einstein condensation. Phys. Rev. **54**, 947 (1938).

[4] O. Penrose and L. Onsager. Bose-Einstein condensation and liquid helium. Phys. Rev. **104**, 576 (1956).

[5] C. N. Yang. Concept of off-diagonal long-range order and the quantum phases of liquid He and of superconductors. Rev. Mod. Phys. **34**, 694 (1962).

[6] P. C. Hohenberg and P. M. Platzman. High-energy neutron scattering from liquid ^{4}He. Phys. Rev. **152**, 198 (1966).

[7] W. C. Kerr, K. N. Pathak, and K. S. Singwi. Neutron scattering from liquid helium-II at large momentum transfer and the condensate fraction. Phys. Rev. A **2**, 2416 (1970).

[8] V. F. Sears and E. C. Svensson. Pair correlations and the condensate fraction in superfluid ^{4}He. Phys. Rev. Lett. **43**, 2009 (1979).

[9] V. F. Sears, E. C. Svensson, P. Martel, and A. D. B. Woods. Neutron-scattering determination of the momentum distribution and the condensate fraction in liquid ^{4}He. Phys. Rev. Lett. **49**, 279 (1982).

[10] W. L. McMillan. Ground state of liquid ^{4}He. Phys. Rev. **138**, A442 (1965).

[11] D. Schiff and L. Verlet. Ground state of liquid helium-4 and helium-3. Phys. Rev. **160**, 208 (1967).

[12] P. M. Lam and M. L. Ristig. Condensed phase of liquid ^{4}He. Phys. Rev. B **20**, 1960 (1979).

[13] M. H. Kalos, D. Levesque, and L. Verlet. Helium at zero temperature with hard-sphere and other forces. Phys. Rev. A **9**, 2178 (1974).

[14] P. A. Whitlock, D. M. Ceperley, G. V. Chester, and M. H. Kalos. Properties of liquid and solid ^{4}He. Phys. Rev. B **19**, 5598 (1979).

[15] S. O. Diallo, J. V. Pearce, R. T. Azuah, J. W. Taylor, and H. R. Glyde. Bose-Einstein coherence in two-dimensional superfluid ^{4}He. Phys. Rev. B **78**, 024512 (2008).

[16] P. Martel, E. C. Svensson, A. D. B. Woods, V. F. Sears, and R. A. Cowley. Neutron scattering from superfluid helium at large momentum transfers. J. Low Temp. Phys. **23**, 285 (1976).

[17] J. W. Halley. Structure of the condensate and some possible ways to observe it. J. Low Temp. Phys. **93**, 893 (1993).

[18] J. W. Halley, C. E. Campbell, C. F. Giese, and K. Goetz. New approach to the observation of the condensate fraction in superfluid helium-4. Phys. Rev. Lett. **71**, 2429 (1993).

[19] K. A. Lidke, A. Wynveen, N. Baisch, C. Koay, C. F. Giese, and J. W. Halley. Phonon mediated helium atom transmission through superfluid helium four. J. Low Temp. Phys. **140**, 429 (2005).

[20] C. D. H. Williams and A. F. G. Wyatt. Quantum transmission of atoms through a slab of superfluid helium. Phys. Rev. Lett. **91**, 085301 (2003).

[21] A. K. Setty. *Quantum coherence in many-body systems.* Ph.D. thesis, University of Minnesota (1998). Retrieved from Dissertations and Theses database. (UMI, AAT 9903651).

[22] A. S. Wynveen. *Scattering processes in Bose-Einstein condensed systems.* Ph.D. thesis, University of Minnesota (2002). Retrieved from Dissertations and Theses database. (UMI, AAT 3066393).

[23] M. Brown and A. F. G. Wyatt. Quantum condensation of liquid ^{4}He. Journal of Physics — Condensed Matter **15**, 4717 (2003).

[24] M. Brown and A. F. G. Wyatt. p. 1050. Proceedings of Phonons 89 (World Scientific, Singapore, 1990).

[25] P. W. Anderson. Interpretation of the Johnston-King experiment on evaporation of liquid He. Phys. Rev. A **29**, 563 (1969).

[26] M. J. Baird, F. R. Hope, and A. F. G. Wyatt. Quantized evaporation from liquid helium. Nature **304**, 325 (1983).

[27] F. R. Hope, M. J. Baird, and A. F. G. Wyatt. Quantum evaporation from liquid ^{4}He by rotons. Phys. Rev. Lett. **52**, 1528 (1984).

[28] M. A. H. Tucker and A. F. G. Wyatt. Double pulse phonon injection into liquid ^{4}He. Physica B **194**, 547 (1994).

[29] J. L. Yarnell, G. P. Arnold, P. J. Bendt, and E. C. Kerr. Excitations in liquid helium: Neutron scattering measurements. Phys. Rev. **113**, 1379 (1959).

[30] M. A. H. Tucker and A. F. G. Wyatt. A fast pulsed source of ballistic R^- rotons in superfluid ^{4}He. J. Low Temp. Phys. **110**, 455 (1998).

[31] M. A. H. Tucker and A. F. G. Wyatt. Evaporation probability of R^- rotons relative to R^+ rotons in superfluid ^{4}He. J. Low Temp. Phys. **113**, 615 (1998).

[32] C. E. Campbell, E. Krotscheck, and M. Saarela. Quantum sticking, scattering, and transmission of ^{4}He atoms from superfluid ^{4}He surfaces. Phys. Rev. Lett. **80**, 2169 (1998).

[33] D. G. Henshaw and A. D. B. Woods. Modes of atomic motions in liquid helium by inelastic scattering of neutrons. Phys. Rev. **121**, 1266 (1961).

[34] R. J. Donnelly and C. F. Barenghi. The observed properties of liquid helium at the saturated vapor pressure. Journal of Physical and Chemical Reference Data **27**, 1217 (1998).
URL `http://www.nist.gov/srd/PDFfiles/jpcrd551.pdf`

[35] J. W. Halley. A novel approach to the observation of the condensate fraction in superfluid helium four. Physica B **197**, 175 (1994).

[36] A. K. Setty, J. W. Halley, and C. E. Campbell. Variational Monte Carlo studies of the rate of transmission of an atomic helium beam through a slab of superfluid helium by a condensate mediated process. Phys. Rev. Lett. **79**, 3930 (1997).

[37] E. Cheng, M. W. Cole, J. Dupont-Roc, W. F. Saam, and J. Treiner. Novel wetting behavior in quantum films. Rev. Mod. Phys. **65**, 557 (1993).

[38] M. C. Williams, C. F. Giese, and J. W. Halley. Suspension of superfluid helium using cesium-coated surfaces. Phys. Rev. B **53**, 6627 (1996).

[39] K. A. Lidke, M. C. Williams, A. Wynveen, and J. W. Halley. Gas dynamics of pulsed low energy helium beams. J. Low Temp. Phys. **121**, 351 (2000).

[40] M. B. Sobnack, J. C. Inkson, and J. C. H. Fung. Quasiparticle scattering at helium surfaces: A microscopic theory. Phys. Rev. B **60**, 3465 (1999).

[41] M. A. H. Tucker and A. F. G. Wyatt. Lifetimes of fast R^+ rotons due to scattering by thermal phonons in superfluid ^{4}He. J. Low Temp. Phys. **110**, 425 (1998).

[42] M. A. H. Tucker and A. F. G. Wyatt. Four phonon scattering in superfluid ^{4}He. Journal of Physics — Condensed Matter **4**, 7745 (1992).

[43] A. F. G. Wyatt. Quantum evaporation of ^{4}He. J. Low Temp. Phys. **87**, 453 (1992).

[44] J. Harms and J. P. Toennies. Experimental evidence for the transmission of ^{3}He atoms through superfluid ^{4}He droplets. Phys. Rev. Lett. **83**, 344 (1999).

[45] D. M. Brink and S. Stringari. Density of states and evaporation rate of helium clusters. Zeitschrift Für Physik D — Atoms Molecules and Clusters **15**, 257 (1990).

[46] M. Lewerenz, B. Schilling, and J. P. Toennies. A new scattering deflection method for determining and selecting the sizes of large liquid clusters of ^{4}He. Chem. Phys. Lett. **206**, 381 (1993).

[47] J. Harms, J. P. Toennies, and F. Dalfovo. Density of superfluid helium droplets. Phys. Rev. B **58**, 3341 (1998).

[48] B. Fåk, K. Guckelsberger, M. Körfer, R. Scherm, and A. J. Dianoux. Elementary excitations in superfluid ^{3}He – ^{4}He mixtures: Pressure and temperature dependence. Phys. Rev. B **41**, 8732 (1990).

[49] B. Fåk and R. Scherm. Neutron scattering studies of liquid ^{3}He and ^{3}He – ^{4}He mixtures. Physica B **197**, 206 (1994).

[50] E. Krotscheck, J. Paaso, M. Saarela, K. Schorkhuber, and R. Zillich. Single-particle and Fermi-liquid properties of ^{3}He – ^{4}He mixtures: A microscopic analysis. Phys. Rev. B **58**, 12282 (1998).

[51] D. O. Edwards, P. Fatouros, G. G. Ihas, P. Mrozinski, S. Y. Shen, F. M. Gasparini, and C. P. Tam. Specular reflection of ^{4}He atoms from the surface of liquid ^{4}He. Phys. Rev. Lett. **34**, 1153 (1975).

[52] V. U. Nayak, D. O. Edwards, and N. Masuhara. Scattering of ^{4}He atoms grazing the liquid ^{4}He surface. Phys. Rev. Lett. **50**, 990 (1983).

[53] A. F. G. Wyatt, M. A. H. Tucker, and R. F. Cregan. Reflectivity of ^{4}He atoms from liquid ^{4}He: Direct observation of the effect of phonons and rotons. Phys. Rev. Lett. **74**, 5236 (1995).

[54] V. Apaja, E. Krotscheck, A. Rimnac, and R. E. Zillich. Quantum reflection, evaporation, and transport currents at ^{4}He surfaces. International Journal of Modern Physics B **20**, 5047 (2006).

[55] H. M. Bohm, V. Apaja, E. Krotscheck, and R. E. Zillich. Quantum reflection, evaporation, and transport currents in ^{4}He. J. Low Temp. Phys. **148**, 115 (2007).

[56] A. Wynveen, A. Setty, A. Howard, J. W. Halley, and C. E. Campbell. Identical particle scattering from a weakly coupled Bose-Einstein condensed gas. Phys. Rev. A **62**, 023602 (2000).

[57] U. V. Poulsen and K. Mølmer. Scattering of atoms on a Bose-Einstein condensate. Phys. Rev. A **67**, 013610 (2003).

[58] C. E. Campbell, E. Krotscheck, and M. Saarela. ^{4}He atoms incident on a superfluid ^{4}He slab: Quantum sticking, scattering and transmission. J. Low Temp. Phys. **113**, 519 (1998).

[59] E. Krotscheck and R. E. Zillich. Dynamics of atom scattering from ^{4}He nanoclusters. European Physical Journal D **43**, 113 (2007).

[60] J. Shumway and D. M. Ceperley. Quantum Monte Carlo treatment of elastic exciton-exciton scattering. Phys. Rev. B **63**, 165209 (2001).

[61] J. Carlson, V. R. Pandharipande, and R. B. Wiringa. Variational calculations of resonant states in ^{4}He. Nuclear Physics A **424**, 47 (1984).

[62] Y. Alhassid and S. E. Koonin. Monte Carlo method for the many-body scattering problem. Annals of Physics **155**, 108 (1984).

[63] D. M. Ceperley and B. Bernu. The calculation of excited-state properties with quantum Monte Carlo. J. Chem. Phys. **89**, 6316 (1988).

[64] J. K. L. MacDonald. Successive approximations by the Rayleigh-Ritz variation method. Phys. Rev. **43**, 830 (1933).

[65] N. Metropolis, A. W. Rosenbluth, M. N. Rosenbluth, A. H. Teller, and E. Teller. Equation of state calculations by fast computing machines. J. Chem. Phys. **21**, 1087 (1953).

[66] D. M. Ceperley and M. H. Kalos. *Quantum Many-Body Problems*, p. 145. Monte Carlo Methods in Statistical Physics (Springer-Verlag Berlin Heidelberg, Berlin, 1979).

[67] B. L. Hammond, W. Lester Jr., and P. J. Reynolds. *Monte Carlo methods in Ab Initio quantum chemistry* (World Scientific, Singapore, 1994).

[68] J. B. Anderson. A random-walk simulation of Schrödinger equation: H_3^+. J. Chem. Phys. **63**, 1499 (1975).

[69] J. B. Anderson. Quantum chemistry by random walk. H ^2P, H_3^+ D_{3h} $^1A_1$, H_2 $^3\Sigma_\mu^+$, H_4 $^1\Sigma_g^+$, Be ^1S. J. Chem. Phys. **65**, 4121 (1976).

[70] J. B. Anderson. Quantum-chemistry by random walk: Higher accuracy. J. Chem. Phys. **73**, 3897 (1980).

[71] F. Mentch and J. B. Anderson. Quantum chemistry by random walk: Importance sampling for H_3^+. J. Chem. Phys. **74**, 6307 (1981).

[72] D. M. Ceperley and B. J. Alder. Ground state of the electron gas by a stochastic method. Phys. Rev. Lett. **45**, 566 (1980).

[73] P. J. Reynolds, D. M. Ceperley, B. J. Alder, and W. A. Lester. Fixed-node quantum Monte-Carlo for molecules. J. Chem. Phys. **77**, 5593 (1982).

[74] J. W. Moskowitz, K. E. Schmidt, M. A. Lee, and M. H. Kalos. A new look at correlation energy in atomic and molecular systems II. The application of the Green's function Monte-Carlo method to LiH. J. Chem. Phys. **77**, 349 (1982).

[75] M. Newman and G. Barkema. *Monte Carlo methods in statistical physics* (Oxford: Clarendon Press, 1999).

[76] S. A. Chin and E. Krotscheck. Structure and collective excitations of ^{4}He clusters. Phys. Rev. B **45**, 852 (1992).

[77] J. Boronat and J. Casulleras. Monte Carlo analysis of an interatomic potential for He. Phys. Rev. B **49**, 8920 (1994).

[78] G. Ortiz, D. M. Ceperley, and R. M. Martin. New stochastic method for systems with broken time-reversal symmetry: 2D fermions in a magnetic field. Phys. Rev. Lett. **71**, 2777 (1993).

[79] K. S. Liu, M. H. Kalos, and G. V. Chester. Quantum hard spheres in a channel. Phys. Rev. A **10**, 303 (1974).

[80] P. J. Reynolds, R. N. Barnett, B. L. Hammond, and W. A. Lester. Molecular physics and chemistry applications of quantum Monte Carlo. J. Stat. Phys. **43**, 1017 (1986).

[81] R. N. Barnett, P. J. Reynolds, and W. A. Lester. Monte-Carlo algorithms for expectation values of coordinate operators. J. Comp. Phys. **96**, 258 (1991).

[82] K. J. Runge and R. J. Runge. Quantum Simulations of Condensed Matter Phenomena (World Scientific, Singapore, 1990).

[83] K. J. Runge. Quantum Monte Carlo calculation of the long-range order in the Heisenberg antiferromagnet. Phys. Rev. B **45**, 7229 (1992).

[84] J. Casulleras and J. Boronat. Unbiased estimators in quantum Monte-Carlo methods: Application to liquid ^{4}He. Phys. Rev. B **52**, 3654 (1995).

[85] A. Sarsa, J. Boronat, and J. Casulleras. Quadratic diffusion Monte Carlo and pure estimators for atoms. J. Chem. Phys. **116**, 5956 (2002).

[86] S. A. Chin. Quadratic diffusion Monte Carlo algorithms for solving atomic many-body problems. Phys. Rev. A **42**, 6991 (1990).

[87] R. Guardiola, O. Kornilov, J. Navarro, and J. P. Toennies. Magic numbers, excitation levels, and other properties of small neutral ^{4}He clusters ($N \leq 50$). The Journal of Chemical Physics **124**, 084307 (2006).

[88] H. A. Forbert and S. A. Chin. Fourth-order diffusion Monte Carlo algorithms for solving quantum many-body problems. Phys. Rev. B **63**, 144518 (2001).

[89] H. A. Forbert and S. A. Chin. A fourth order diffusion monte carlo algorithm for solving quantum many-body problems. International Journal of Modern Physics B **15**, 1752 (2001).

[90] D. Ceperley (2006). Personal communications.

[91] J. Boronat. *Helium in one, two and three dimensions.* In Krotscheck and Navarro [99] (2002).

[92] D. P. Landau and K. Binder. *A guide to Monte Carlo simulations in statistical physics* (Cambridge University Press, UK, 2005).

[93] J. R. Trail. Heavy-tailed random error in quantum Monte Carlo. Phys. Rev. E **77**, 016703 (2008).

[94] D. M. Ceperley. Path integrals in the theory of condensed helium. Rev. Mod. Phys. **67**, 279 (1995).

[95] B. M. Axilrod and E. Teller. J. Chem. Phys. **11**, 293 (1943).

[96] J. E. Lennard-Jones. Cohesion. Proceedings of the Physical Society **43**, 461 (1931).

[97] J. de Boer and A. Michels. Contribution to the quantum-mechanical theory of the equation of state and the law of corresponding states. Determination of the law of force of helium. Physica, **5**, 945 (1938).

[98] J. de Boer and A. Michels. The influence of the interaction of more than two molecules on the molecular distribution function in compressed gases. Physica **6**, 97 (1939).

[99] E. Krotscheck and J. Navarro, eds. *Microscopic approaches to quantum liquids in confined geometries* (World Scientific, River Edge, N.J., 2002).

[100] R. A. Aziz, V. P. S. Nain, J. S. Carley, W. L. Taylor, and G. T. McConville. Accurate inter-molecular potential for helium. J. Chem. Phys. **70**, 4330 (1979).

[101] M. H. Kalos, M. A. Lee, P. A. Whitlock, and G. V. Chester. Modern potentials and the properties of condensed ^{4}He. Phys. Rev. B **24**, 115 (1981).

[102] R. A. Aziz, F. R. W. McCourt, and C. C. K. Wong. A new determination of the ground state interatomic potential for He_2. Molecular Physics **61**, 1487 (1987).

[103] R. A. Aziz, A. R. Janzen, and M. R. Moldover. Ab initio calculations for helium: A standard for transport property measurements. Phys. Rev. Lett. **74**, 1586 (1995).

[104] E. L. Pollock and D. M. Ceperley. Path-integral computation of superfluid densities. Phys. Rev. B **36**, 8343 (1987).

[105] J. E. Cuervo, P. N. Roy, and M. Boninsegni. Path integral ground state with a fourth-order propagator: Application to condensed helium. J. Chem. Phys. **122**, 114504 (2005).

[106] B. K. Clark and D. M. Ceperley. Off-diagonal long-range order in solid ^{4}He. Phys. Rev. Lett. **96**, 105302 (2006).

[107] D. O. Edwards, S. Y. Shen, J. R. Eckardt, P. P. Fatouros, and F. M. Gasparini. Propagation of surface sound in superfluid ^{3}He – ^{4}He. Phys. Rev. B **12**, 892 (1975).

[108] J. M. Valles, R. H. Higley, R. B. Johnson, and R. B. Hallock. Nuclear magnetic susceptibility measurements of ^{3}He – ^{4}He mixture films. Phys. Rev. Lett. **60**, 428 (1988).

[109] K. D. Morhard, J. Bossy, and H. Godfrin. NMR measurements on ^{3}He adsorbed on Grafoil at submonolayer coverages and millikelvin temperatures. Phys. Rev. B **51**, 446 (1995).

[110] K. D. Morhard, C. Bauerle, J. Bossy, Y. Bunkov, S. N. Fisher, and H. Godfrin. Two-dimensional Fermi liquid in the highly correlated regime: The second layer of ^{3}He adsorbed on graphite. Phys. Rev. B **53**, 2658 (1996).

[111] P. A. Sheldon and R. B. Hallock. Properties of 2D ^{3}He on very thin ^{4}He films. Phys. Rev. Lett. **77**, 2973 (1996).

[112] A. Casey, H. Patel, J. Nyeki, B. P. Cowan, and J. Saunders. Strongly correlated two dimensional fluid ^{3}He. J. Low Temp. Phys. **113**, 293 (1998).

[113] C. Bauerle, Y. M. Bunkov, A. S. Chen, S. N. Fisher, and H. Godfrin. Ultra-low temperature magnetic properties of liquid ^{3}He films. J. Low Temp. Phys. **110**, 333 (1998).

[114] P. C. Ho and R. B. Hallock. Heat capacity studies of ^{3}He in ^{3}He–^{4}He mixture films and the coverage dependence of the two-dimensional

^{3}He Landau Fermi-liquid parameters. Phys. Rev. Lett. **8713**, 135301 (2001).

[115] A. D. Novaco and C. E. Campbell. Effects of crystalline substrate potentials on quasi-two-dimensional liquid helium. Phys. Rev. B **11**, 2525 (1975).

[116] M. D. Miller and L. H. Nosanow. Liquid-to-gas phase transitions in 2-dimensional quantum systems at zero temperature. J. Low Temp. Phys. **32**, 145 (1978).

[117] B. Brami, F. Joly, and C. Lhuillier. Is there a liquid phase in a (sub)monolayer of ^{3}He adsorbed on graphite. J. Low Temp. Phys. **94**, 63 (1994).

[118] E. Krotscheck. Liquid helium on a surface: Ground state, excitations, condensate fraction, and impurity potential. Phys. Rev. B **32**, 5713 (1985).

[119] B. E. Clements, E. Krotscheck, and M. Saarela. Impurity dynamics in boson quantum films. Phys. Rev. B **55**, 5959 (1997).

[120] F. Y. Wu and E. Feenberg. Theory of the Fermion liquid. Phys. Rev. **128**, 943 (1962).

[121] A. Bijl. The lowest wave function of the symmetrical many particles system. Physica, **7**, 869 (1940).

[122] R. Dingle. The zero-point energy of a system of particles. Phil. Mag. **40**, 573 (1949).

[123] R. Jastrow. Many-body problem with strong forces. Phys. Rev. **98**, 1479 (1955).

[124] E. W. Draeger. *Path Integral Monte Carlo simulations of helium: From superfluid droplets to quantum crystals.* Ph.D. thesis, University of Illinois at Urbana-Champain (2001). Retrieved from Dissertations and Theses database. (UMI, AAT 3023044).

[125] K. S. Liu, M. H. Kalos, and G. V. Chester. Variational calculations of liquid ^{4}He with free surfaces. Phys. Rev. B **12**, 1715 (1975).

[126] J. M. Marin, J. Boronat, and J. Casulleras. Free surface of superfluid ^{4}He at zero temperature. Phys. Rev. B **71**, 144518 (2005).

[127] J. L. Epstein and E. Krotscheck. Structure and excitations of liquid-helium films. Phys. Rev. B **37**, 1666 (1988).

[128] J. L. Valles and K. E. Schmidt. Ground state properties of the free surface of liquid ^{4}He. Phys. Rev. B **38**, 2879 (1988).

[129] K. Penanen, M. Fukuto, R. K. Heilmann, I. F. Silvera, and P. S. Pershan. ^{4}He liquid-vapor interface below 1 K studied using X-ray reflectivity. Phys. Rev. B **62**, 9621 (2000).

[130] L. B. Lurio, T. A. Rabedeau, P. S. Pershan, I. F. Silvera, M. Deutsch, S. D. Kosowsky, and B. M. Ocko. Liquid-vapor density profile of helium: An X-ray study. Phys. Rev. Lett. **68**, 2628 (1992).

[131] E. W. Draeger and D. M. Ceperley. Bose-einstein condensation at a helium surface. Phys. Rev. Lett. **89**, 015301 (2002).

[132] M. Casas, F. Dalfovo, A. Lastri, L. Serra, and S. Stringari. Density-functional calculations for ^{4}He droplets. Zeitschrift Für Physik D — Atoms Molecules and Clusters **35**, 67 (1995).

[133] R. M. Panoff and J. Carlson. Fermion Monte Carlo algorithms and liquid ^{3}He. Phys. Rev. Lett. **62**, 1130 (1989).

[134] S. Moroni, S. Fantoni, and G. Senatore. Euler monte-carlo calculations for liquid ^{4}He and ^{3}He. Phys. Rev. B **52**, 13547 (1995).

[135] P. J. Reynolds, R. N. Barnett, B. L. Hammond, R. M. Grimes, and W. A. Lester. Quantum chemistry by quantum Monte Carlo: Beyond ground-state energy calculations. International Journal of Quantum Chemistry **29**, 589 (1986).

[136] S. Giorgini, J. Boronat, and J. Casulleras. Diffusion Monte Carlo study of two-dimensional liquid ^{4}He. Phys. Rev. B **54**, 6099 (1996).

[137] S. Giorgini, J. Boronat, and J. Casulleras. Vortex excitation in superfluid ^{4}He: A diffusion Monte Carlo study. Phys. Rev. Lett. **77**, 2754 (1996).

[138] J. Boronat and J. Casulleras. Microscopic calculation of the phonon-roton branch in superfluid ^{4}He. Europhysics Letters **38**, 291 (1997).

[139] P. R. C. Kent. *Techniques and Applications of Quantum Monte Carlo*. Ph.D. thesis, Robinson College, Cambridge (1999).
URL `http://www.physics.uc.edu/~pkent/thesis/`

[140] W. H. Press, S. A. Teukolsky, W. T. Vetterling, and B. P. Flannery. *Numerical recipes: The art of scientific computing* (Cambridge University Press, New York, 2007).

Appendix A

Derivation of the evolution equation

The following is a derivation of the evolution equation (3.6) in its differential equation form.

$$f = \Psi_{\mathrm{T}} e^{-(\mathcal{H}-E_{\mathrm{ref}})\tau} \Psi_{\mathrm{I}}$$

$$\begin{aligned} \frac{\partial f}{\partial \tau} &= -\Psi_{\mathrm{T}} \left(\mathcal{H} - E_{\mathrm{ref}}\right) e^{-(\mathcal{H}-E_{\mathrm{ref}})\tau} \Psi_{\mathrm{I}} \\ &= -\Psi \left(\mathcal{H} - E_{\mathrm{ref}}\right) \left(\frac{f}{\Psi_{\mathrm{T}}}\right) \\ &= E_{\mathrm{ref}} f - \Psi \mathcal{H} \left(\frac{f}{\Psi_{\mathrm{T}}}\right) \end{aligned} \tag{A.1}$$

Notice how this expression depends only on the (analytically known) trial function Ψ_{T}. Let $\boldsymbol{R}$ be a coordinate in the configuration space: $\boldsymbol{R} = (\boldsymbol{x}_1, \cdots, \boldsymbol{x}_N)$,

$$\mathcal{H} = -\frac{\hbar^2}{2m}\nabla^2_{\boldsymbol{R}} + V(\boldsymbol{R})$$

$$-\Psi\mathcal{H}\frac{f}{\Psi} = \Psi\frac{\hbar^2}{2m}\left(\frac{\nabla^2 f}{\Psi} - 2\frac{\nabla f\cdot\nabla\Psi}{\Psi^2} - \frac{f\nabla^2\Psi}{\Psi^2} + 2\frac{f\left(\nabla\Psi\right)^2}{\Psi^3}\right) - \Psi V\frac{f}{\Psi}$$

Combining the above expression with (A.1) gives the evolution equation:

$$\begin{aligned}
\frac{\partial f}{\partial\tau} &= E_{\mathrm{ref}}f + \frac{\hbar^2}{2m}\left(\nabla^2 f - 2\frac{\nabla f\cdot\nabla\Psi}{\Psi} - \frac{f\nabla^2\Psi}{\Psi} + 2\frac{f\left(\nabla\Psi\right)^2}{\Psi^2}\right) - Vf \\
&= \frac{\hbar^2}{2m}\left(\nabla^2 f - 2\left(\frac{\nabla f\cdot\nabla\Psi}{\Psi} + \frac{f\nabla^2\Psi}{\Psi} - \frac{f\left(\nabla\Psi\right)^2}{\Psi^2}\right)\right) \\
&\quad + \frac{\hbar^2}{2m}f\frac{\nabla^2\Psi}{\Psi} - Vf + E_{\mathrm{ref}}f \\
&= \frac{\hbar^2}{2m}\left(\nabla^2 f - \nabla\cdot\left(f\nabla\ln|\Psi|^2\right)\right) - \left(\frac{\mathcal{H}\Psi}{\Psi} - E_{\mathrm{ref}}\right)f
\end{aligned}$$

Appendix B

Limit-safe forms of various derivatives of profile envelope

During the simulation, an envelope term was used in the guiding function to ensure the form of the helium film and to speed up the execution. This function and its derivatives had to be evaluated for each atom at every execution step. To speed up the execution, these functions were tabulated and splined, which in turn required up to fourth derivative of the envelope function. Because the expressions in the exponents tend to be rather large and may lead to be evaluation errors, we rewrote these function in a way that is safer for computer evaluation.

Below are the derivative expressions for envelope function. With the notation

$$\gamma \equiv \exp\left(-\frac{a}{b}\right) \tag{B.1}$$

Functions for the profile become

$$f = \frac{1 - cx^2}{\left(2\gamma + \frac{1+\gamma^2}{\cosh(x/b)}\right)\cosh\left(x/b\right)}$$

$$\begin{aligned} f'' =& \frac{-2c}{\left(2\gamma + \frac{1+\gamma^2}{\cosh(x/b)}\right)\cosh\left(x/b\right)} \\ &+ \frac{8cx\frac{\gamma}{b}\,\mathrm{sign}(x)\frac{1-\exp\left(-2\frac{|x|}{b}\right)}{1+\exp\left(-2\frac{|x|}{b}\right)} - 2(1-cx^2)\frac{\gamma}{b^2}}{\left(2\gamma + \frac{1+\gamma^2}{\cosh(x/b)}\right)^2\cosh\left(x/b\right)} \\ &+ \frac{16\left(1-cx^2\right)\left(\frac{\gamma}{b}\right)^2}{\left(2\gamma + \frac{1+\gamma^2}{\cosh(x/b)}\right)^3}\frac{\left(1-\exp\left(-2\frac{|x|}{b}\right)\right)^2}{\left(1+\exp\left(-2\frac{|x|}{b}\right)\right)^3}\frac{1}{\exp\left(\frac{|x|}{b}\right)} \end{aligned}$$

Functions for the logarithmic derivative:

$$\frac{f'}{f} = -\frac{2cx}{1-cx^2} - \frac{2\frac{\gamma}{b}}{2\gamma + \frac{1+\gamma^2}{\cosh(x/b)}}\,\mathrm{sign}(x)\frac{1-\exp\left(-2\frac{|x|}{b}\right)}{1+\exp\left(-2\frac{|x|}{b}\right)}$$

$$\left(\frac{f'}{f}\right)'' = -\frac{16c^3x^3}{(1-cx^2)^3} - \frac{12c^2x}{(1-cx^2)^2}$$
$$- 2\frac{\frac{\gamma}{b^3}}{\left(2\gamma + \frac{1+\gamma^2}{\cosh(x/b)}\right)}\,\mathrm{sign}(x)\frac{1-\exp\left(-2\frac{|x|}{b}\right)}{1+\exp\left(-2\frac{|x|}{b}\right)}$$
$$+ 12\frac{\frac{\gamma^2}{b^3}}{\left(2\gamma + \frac{1+\gamma^2}{\cosh(x/b)}\right)^2}\,\mathrm{sign}(x)\frac{1-\exp\left(-2\frac{|x|}{b}\right)}{1+\exp\left(-2\frac{|x|}{b}\right)}$$
$$- 16\frac{\frac{\gamma^3}{b^3}}{\left(2\gamma + \frac{1+\gamma^2}{\cosh(x/b)}\right)^3}\,\mathrm{sign}(x)\left(\frac{1-\exp\left(-2\frac{|x|}{b}\right)}{1+\exp\left(-2\frac{|x|}{b}\right)}\right)^3$$

Functions for the second "relative" derivative are below. Let us additionally label

$$\begin{aligned}\mathcal{D} &= 2\gamma + \frac{1+\gamma^2}{\cosh(x/b)} \\ \mathcal{S} &= \mathrm{sign}(x)\frac{1-\exp\left(-2\frac{|x|}{b}\right)}{1+\exp\left(-2\frac{|x|}{b}\right)}\end{aligned}$$

then

$$\frac{f''}{f} = -2\frac{c}{1-cx^2} + \frac{1}{\mathcal{D}}\left(8\frac{\gamma}{b}\frac{cx}{1-cx^2}\mathcal{S} - 2\frac{\gamma}{b^2}\right) + 8\left(\frac{\gamma}{b}\right)^2\frac{\mathcal{S}^2}{\mathcal{D}^2}$$

$$
\begin{aligned}
\left(\frac{f''}{f}\right)'' =& 192\left(\frac{\gamma}{b}\right)^4\frac{\mathcal{S}^4}{\mathcal{D}^4} \\
&+\frac{1}{\mathcal{D}^3}\left(-176\frac{\gamma^3}{b^4}\mathcal{S}^2+64\frac{\gamma^3}{b^3}\frac{cx}{1-cx^2}\mathcal{S}^3\right) \\
&+\frac{1}{\mathcal{D}^2}\left(12\frac{\gamma^2}{b^4}-48\frac{\gamma^2}{b^3}\frac{cx}{1-cx^2}\mathcal{S}+32\left(\frac{\gamma^2}{b^4}-2\frac{\gamma^2}{b^2}\frac{c^2x^2}{\left(1-cx^2\right)^2}-\frac{\gamma^2}{b^2}\frac{c}{1-cx^2}\right)\mathcal{S}^2\right) \\
&+\frac{1}{\mathcal{D}}\left(-2\frac{\gamma}{b^4}+32\frac{\gamma}{b^2}\frac{c^2x^2}{\left(1-cx^2\right)^2}+16\frac{\gamma}{b^2}\frac{c}{1-cx^2}\right. \\
&\left.+\left(64\frac{\gamma}{b}\frac{c^3x^3}{\left(1-cx^2\right)^3}+48\frac{\gamma}{b}\frac{c^2x}{\left(1-cx^2\right)^2}+8\frac{\gamma}{b^3}\frac{cx}{1-cx^2}\right)\mathcal{S}\right) \\
&-16\frac{c^3x^2}{\left(1-cx^2\right)^3}-4\frac{c^2}{\left(1-cx^2\right)^2}
\end{aligned}
$$

Appendix C

Guiding and branching terms for bulk trial functions

In order to compute both local energy and the guiding term, it is in fact sufficient to calculate first and second derivatives of the log of the trial function. Drift is given simply by the logarithmic derivative and the local energy can be expressed in terms of

$$T_i = -\frac{1}{4}\nabla_i^2 \log \Psi_{\mathrm{T}}$$

and

$$F_i = \frac{1}{\sqrt{2}}\nabla_i \log \Psi_{\mathrm{T}}$$

as

$$E_{\mathrm{L}} = \sum_i K_i = \sum_i 2T_i - F_i^2 \tag{C.1}$$

presuming $\hbar^2/m = 1$ (in our case the units were set so that $\hbar^2/2m = 1$). See Ref. [139] for details.

We had optimized summations involved in computing the local energy and drift term as this is the most computationally intensive part of the simulation. As much of summation as possible was done by hand and we used standard expression for local energy. Below I will list several important forms relevant for finding the local energy.

Notation

Coordinates in the configuration space, i.e. coordinates of particles represented by a walker are labeled in this section by symbol x with two subscripts. (The second subscript is sometimes dropped for brevity.) The first subscript corresponds to particle "number" within the system and the second one denotes the physical dimension in which the measurement is taken. For example, $x_{2,3}$ is the third physical coordinate of the second atom.

We also use zxy order of coordinates. Therefore the impact (lateral) direction as the first one. That is $x_{s,1}$ is equivalent to "z" coordinate of the s^{th} atom. This is a choice mainly for programming convenience and ease of changing the dimensionality of the problem.

When the impact ("z" elsewhere in the text) dimension is implied, such as in the envelope and parity functions, the coordinate index is sometimes dropped, so that x_s is the same as $x_{s,1}$.

Derivatives of the Jastrow part of the wavefunction

Consider derivatives for the Jastrow type trial function with power-law pseudopotential:

$$\Psi_J = \prod_{j<i}^{P} \exp\left[-\left(\frac{a}{r}\right)^5\right]$$

where $P \equiv N+1$ denotes number of particles in the system. Consider the first logarithmic derivative:

$$\begin{aligned}\nabla_{s,t} \log \Psi_T &= \nabla_{s,t} \log \prod_{i<j}^{P} \exp\left[-\left(\frac{a}{r_{ij}}\right)^5\right] \\ &= -\nabla_{s,t} \sum_{i<j}^{P} \left(\frac{a}{r_{ij}}\right)^5 = \sum_{i<j}^{P} 5\left(\frac{a}{r_{ij}}\right)^5 \frac{\nabla_{s,t} r_{ij}}{r_{ij}}\end{aligned}$$

With the distance between particles written in the form

$$r_{ij} = \left[\sum_{m=1}^{D} (x_{i,m} - x_{j,m})^2\right]^{\frac{1}{2}}$$

where D is the dimensionality of physical space, the derivatives can be written as

$$\begin{aligned}\nabla_{s,t} r_{ij} &= \frac{1}{2}\frac{1}{r_{ij}} \sum_{t=1}^{D} \nabla_{s,t} (x_{i,m} - x_{j,m})^2 \\ &= \frac{1}{r_{ij}} \sum_{t=1}^{D} \delta_{t,m} \left(\delta_{s,i} - \delta_{s,j}\right) \left(x_{i,m} - x_{j,m}\right) \\ &= \frac{\left(\delta_{s,i} - \delta_{s,j}\right) \left(x_{i,t} - x_{j,t}\right)}{r_{ij}}\end{aligned}$$

The second derivative is given by

$$\nabla_{s,t}^2 r_{ij} = -\frac{(\delta_{s,i}-\delta_{s,j})^2 (x_{i,t}-x_{j,t})^2}{r_{ij}^3} + \frac{(\delta_{s,i}-\delta_{s,j})^2}{r_{ij}}$$

and with the requirement that $i \neq j$,

$$\nabla_{s,t}^2 r_{ij} = -\frac{(\delta_{s,i}+\delta_{s,j})(x_{i,t}-x_{j,t})^2}{r_{ij}^3} + \frac{\delta_{s,i}+\delta_{s,j}}{r_{ij}}$$

With this we can write for the logarithmic derivative, a quantity that we also label $J'_{s,t}$:

$$\begin{aligned} J'_{s,t} &\stackrel{\text{def}}{=} \frac{\nabla_{s,t}\Psi_T}{\Psi_T} \equiv \nabla_{s,t} \log \Psi_T = 5a^5 \sum_{i<j}^{P} \frac{(\delta_{s,i}-\delta_{s,j})\,(x_{i,t}-x_{j,t})}{r_{ij}^7} \\ &= 5a^5 \left(\sum_{s<j}^{P} \frac{(x_{s,t}-x_{j,t})}{r_{sj}^7} - \sum_{i<s}^{P} \frac{(x_{i,t}-x_{s,t})}{r_{is}^7} \right) \\ &= 5a^5 \sum_{i\neq s}^{P} \frac{x_{s,t}-x_{i,t}}{r_{is}^7} \end{aligned} \tag{C.2}$$

Consider $J''_{s,t} \stackrel{\text{def}}{=} \nabla_{s,t} J'_{s,t}$:

$$\begin{aligned} J''_{s,t} &= \nabla_{s,t} 5a^5 \sum_{i\neq s}^{P} \frac{(x_{s,t}-x_{i,t})}{r_{is}^7} \\ &= 5a^5 \sum_{i\neq s}^{P} \frac{1}{r_{is}^7} + \frac{(x_{s,t}-x_{i,t})}{r_{is}^8}(-7)\frac{(\delta_{s,i}-1)\,(x_{i,t}-x_{s,t})}{r_{is}} \\ &= 5a^5 \sum_{i\neq s}^{P} \frac{1}{r_{is}^7} - 7\frac{(x_{s,t}-x_{i,t})^2}{r_{is}^9} \end{aligned}$$

Appendix D

Computational details

Splines

Transmission simulations involved calculating profile envelope f, first and second derivatives and various combinations of these.

In order to speed up the simulation, these functions (namely f, f'/f and f''/f) and their respective second derivatives were pre-tabulated before the main potion of the simulation. Cubic splines [140] produced with these tables were used to compute envelope functions during the simulation.

Cubic splines were computed in the following form. For a point x located between spline nodes x_i and x_{i+1}, splined value of $y(x)$ is computed based on values of function and its second derivatives on the nodes: $y_i = y(x_i)$ and $y''_i = y''(x_i)$ as

$$y = Ay_i + By_{i+1} + Cy''_i + Dy''_{i+1} \tag{D.1}$$

with coefficients

$$
\begin{aligned}
A &= \frac{x_{i+1} - x}{x_{i+1} - x_i} \\
B &= 1 - A = \frac{x - x_i}{x_{i+1} - x_i} \\
C &= \frac{1}{6}\left(A^3 - A\right)\left(x_{i+1} - x_i\right)^2 \\
D &= \frac{1}{6}\left(B^3 - B\right)\left(x_{i+1} - x_i\right)^2
\end{aligned}
$$

With evenly spaced spline nodes $x_{i+1} - x_i = h_i \equiv \text{const}$, this approach becomes a fast and convenient interpolation scheme. Indexes of embracing nodes are easy to calculate (i.e. for a given x finding i such that $x_i < x < x_{i+1}$ is straightforward and computationally cheap), and high order of convergence in step size h assures that number of nodes (and hence the amount of used high-level cash memory) is small. With 13 algebraic multiply-add operations and no divisions per cubic spline calculation (all denominators can be pre-computed), this calculation can be done very cheaply in terms of computational power on the multi-staged Power 4 processors. For reasons of utilizing the staged architecture of Power 4 processors more efficiently, spline values were computed on entire coordinate arrays at a time. Using splines as a replacement for analytically defined provided for a significant speed up in the execution time.

In appendix B we list derivatives of the envelope function in the forms

necessary for computing such spline coefficients.

We ensued that all splined functions are computed everywhere better than a rather small number, typically 10^{-6} or less. This usually required using few thousand spline nodes. Spline step h can be reliably selected for a desired accuracy ϵ with $h \ll \sqrt[4]{24\epsilon}$, with a factor of about 10 to ensure the "much lesser" relation. Accuracy was checked automatically at the beginning of an execution.